

# ANALYZING $\text{BaTiO}_3$ FOR FERROELECTRIC TUNING OF THE $\text{LaAlO}_3/\text{SrTiO}_3$ INTERFACE

Chiel Scholten

FACULTY OF SCIENCE AND TECHNOLOGY  
INTERFACES AND CORRELATED ELECTRON SYSTEMS  
QUANTUM TRANSPORT IN MATTER

**EXAMINATION COMMITTEE**

prof. dr. ir. Alexander Brinkman  
dr. ir. Gertjan Koster  
dr. Marc Dhallé  
ir. Sander Wenderich



**Analyzing BaTiO<sub>3</sub> for ferroelectric tuning of the  
LaAlO<sub>3</sub>/SrTiO<sub>3</sub> interface**

Chiel Scholten

26 July 2013



# Summary

This master thesis describes a study on barium titanate ( $\text{BaTiO}_3$ , BTO) for the ferroelectric tuning of the two-dimensional electron gas (2DEG) at the interface between lanthanum aluminate ( $\text{LaAlO}_3$ , LAO) and strontium titanate ( $\text{SrTiO}_3$ , STO). This research is initiated from an interest in ferroelectrically enhanced strong spin-orbit coupling in the LAO-STO 2DEG for the research on Majorana fermions. The main goal of this research project was realizing and characterizing ferroelectric tuning of the LAO-STO 2DEG.

The conducting interface between the insulators LAO and STO can have many remarkable properties, such as 2D superconductivity and strong spin-orbit coupling. This spin-orbit coupling can be enhanced by a ferroelectric top layer. Under the right conditions such a materials system is predicted to host Majorana fermions. The spontaneous polarization of the ferroelectric top layer establishes an electric field towards the LAO-STO interface which influences the electronic properties of the 2DEG. When this field is strong enough and has the right polarity it might deplete the LAO-STO 2DEG, resulting in an insulating interface. Since the spontaneous polarization direction of the ferroelectric can, in principle, be switched in a temporary externally applied electric field, the system could act as an electronic switch. The BTO-LAO-STO system, in which BTO is employed as the ferroelectric, can therefore be used to ferroelectrically tune the LAO-STO interface 2DEG.

In this research this materials system has been manufactured, characterized and analyzed using different techniques. The main tool used is piezoresponse force microscopy (PFM), that allows imaging and manipulation of the polarization in ferroelectric materials. The LAO-STO interface in BTO-LAO-STO was electronically characterized and turned out to exhibit qualitatively the same behaviour as LAO-STO samples without a BTO top layer. In all samples analyzed local ferroelectricity was repeatedly observed in the out-of-plane direction. The PFM measurements revealed that the materials system has a preferred (spontaneous) polarization direction, which can only be switched as long as an external electric field is present. This is due to internal electric field biases in the system and is highly disadvantageous for the pursued goal of this project.

To explain this preferred (spontaneous) polarization direction a band bending model was developed. The presence of internal biases in this model is ascribed to band bending at the different interfaces in the BTO-LAO-STO materials system, which are expected to pin the polarization. This model turned out to be only in partial agreement with the examined materials systems. Therefore, the model was extended by considering additional sources of internal bias. Among these are internal biases due to oxygen vacancies and strain in the materials system. The relative contribution of all possible sources of internal bias could not be determined from the current research.

Gating experiments on BTO-LAO-STO have been performed on a gate bar device to find any contribution from ferroelectric tuning of the 2DEG. However, the sought-after effect has not been clearly observed. This might be due to the inhomogeneity of the ferroelectricity in all samples. At crucial spots on the gate bar no ferroelectricity was found, which is detrimental for the functioning of the device. The main goal of this research has therefore only been partly reached. Recommendations are presented to reach this goal in the near future.



# Contents

<b>Summary</b>	<b>iii</b>
<b>1 Introduction</b>	<b>1</b>
1.1 Goal of the project . . . . .	1
1.2 LAO-STO system . . . . .	1
1.3 Ferroelectricity and piezoelectricity . . . . .	3
1.3.1 Barium titanate . . . . .	5
1.4 Ferroelectric control in recent literature . . . . .	6
1.5 Outline . . . . .	7
<b>2 Theoretical background of spin-orbit interactions and Majorana physics</b>	<b>9</b>
2.1 Origin of spin-orbit interactions . . . . .	9
2.2 Symmetry and symmetry breaking . . . . .	11
2.2.1 Time reversal symmetry . . . . .	11
2.2.2 Inversion symmetry . . . . .	12
2.3 Rashba spin-orbit coupling . . . . .	13
2.4 Effects of Rashba spin-orbit coupling and Zeeman interaction on 2DEG's . . . . .	14
2.5 The role of spin-orbit coupling in Majorana physics . . . . .	16
2.5.1 Majorana physics in the LAO-STO system . . . . .	18
<b>3 Principles of Piezoresponse Force Microscopy</b>	<b>19</b>
3.1 Thermodynamic energy of piezoelectricity . . . . .	19
3.2 Piezoresponse of ferroelectrics . . . . .	22
3.3 The PFM technique . . . . .	23
3.3.1 General working principle . . . . .	23
3.3.2 Microscopy . . . . .	25
3.3.3 Spectroscopy . . . . .	26
<b>4 Manufacturing and characterizing samples</b>	<b>29</b>
4.1 Substrate treatment and selection . . . . .	29
4.2 RHEED controlled pulsed laser deposition . . . . .	30
4.2.1 Conditions for a conducting LAO-STO interface . . . . .	31
4.2.2 Optimizing growth conditions of ferroelectric BTO on LAO-STO . . . . .	32
4.2.3 Conditions for SRO as back electrode . . . . .	33
4.3 Characterizing BTO-LAO-STO . . . . .	34
4.3.1 Electronic properties of the LAO-STO interface . . . . .	34
4.3.2 Verification of ferroelectricity . . . . .	35
4.3.3 X-ray diffraction . . . . .	37
4.4 PFM sample preparation . . . . .	38
4.4.1 Back gate and specimen plate . . . . .	38
4.4.2 Top gates . . . . .	38

4.5	Device fabrication . . . . .	39
4.5.1	Amorphous LAO structuring . . . . .	39
4.5.2	Back electrode etching and contact deposition . . . . .	41
4.5.3	Gates and top electrodes . . . . .	41
4.6	Effect of water on BTO . . . . .	42
<b>5</b>	<b>Analyzing ferroelectricity and its tuning effect in BTO-LAO-STO</b>	<b>47</b>
5.1	Ferroelectric hysteresis . . . . .	47
5.1.1	Piezoresponse . . . . .	47
5.1.2	Shifted loops . . . . .	48
5.1.3	Training and loop inversion . . . . .	49
5.2	Internal biases and polarization direction . . . . .	49
5.2.1	Band bending model . . . . .	49
5.2.2	Verifying the model . . . . .	52
5.2.3	Extending the band bending model . . . . .	54
5.2.4	Consequences of internal bias . . . . .	55
5.3	Inhomogeneous ferroelectricity . . . . .	55
5.4	Gating BTO-LAO-STO . . . . .	57
<b>6</b>	<b>Conclusions and recommendations</b>	<b>61</b>
6.1	Conclusions . . . . .	61
6.2	Recommendations . . . . .	64
6.2.1	Improving the materials system and measurements . . . . .	64
6.2.2	Further research . . . . .	65
	<b>Dankwoord</b>	<b>67</b>
	<b>References</b>	<b>73</b>
	<b>Appendix A Theory of spontaneous polarization</b>	<b>75</b>
A.1	Ginzburg-Landau theory of ferroelectric phase transition . . . . .	75
A.2	Ferroelectric hysteresis and domains . . . . .	78
	<b>Appendix B A short user guide to Piezoresponse Force Microscopy</b>	<b>81</b>
B.1	Preparations . . . . .	81
B.1.1	Sample . . . . .	81
B.1.2	Tip . . . . .	82
B.2	Measurements . . . . .	82
B.2.1	PFM mode . . . . .	82
B.2.2	Tuning the Tip . . . . .	82
B.2.3	Topographical measurements: reading . . . . .	84
B.2.4	Topographical measurements: writing . . . . .	84
B.2.5	Spectroscopy measurements . . . . .	87
B.3	Final remarks . . . . .	88

# Chapter 1

## Introduction

In this chapter the main concepts and materials systems important in this research project are introduced. Furthermore, the goal of this research project is defined and the idea of the project is explained. At the end of this chapter a recently published article on the same topic as this master thesis is discussed and the outline of this master thesis is given.

### 1.1 Goal of the project

In this project the effect of a ferroelectric top layer on the electronic properties of a conducting interface between two oxides is studied. The oxides considered are the perovskites lanthanum aluminate ( $\text{LaAlO}_3$ , LAO) and strontium titanate ( $\text{SrTiO}_3$ , STO). At the interface between these two insulators a two-dimensional electron gas (2DEG) is formed. An electric field can influence the electronic properties of this 2DEG. The ferroelectric perovskite barium titanate ( $\text{BaTiO}_3$ , BTO) is used to apply the desired electric field, which is sustained by the spontaneous polarization of this ferroelectric. The polarization of a ferroelectric is, in principle, switchable by an externally applied electric field. Switching of the polarization results in switching of the internal electric field, tuning the properties of the 2DEG accordingly. At high enough electric fields with the appropriate polarity, the 2DEG might even be depleted. The current all-oxide system might therefore act as an electronic switch, controlled by short voltage pulses, which change the polarization of the ferroelectric.

Another interesting feature of this system is the fact that the  $\text{LaAlO}_3/\text{SrTiO}_3$  interface can be made superconducting. This can be achieved by applying the right growth conditions for the crystal growth of LAO on STO. The electric field of the ferroelectric might now reveal new physics due to induced strong spin-orbit coupling, as will be discussed in chapter 2. It was suggested that this may induce p-wave superconductivity at the LAO-STO interface [1], which makes it a potentially interesting system for the search for Majorana fermions.

The initial goal of this project is to realize strong spin-orbit coupling induced by a ferroelectric top layer in the LAO-STO 2DEG for the research on Majorana fermions. The main goal, however, is realizing and characterizing ferroelectric tuning of the LAO-STO 2DEG. During the project some sub goals were defined: (1) grow a well-chosen ferroelectric layer by pulsed laser deposition (2) grow and verify that a ferroelectric top layer on LAO-STO does not destroy the 2DEG, (3) analyze the ferroelectric properties of the materials system, (4) make devices for electronic measurements on the materials system and (5) use these devices to examine whether there occurs some sort of ferroelectric tuning of the 2DEG.

### 1.2 LAO-STO system

The presence of a two-dimensional electron gas at the LAO-STO interface was first reported in Nature in 2004 [2]. At first sight this materials system bears an intriguing and paradox-

ical fact: the interface between these two insulating materials is conducting. However, the different theories on the formation of the interface 2DEG between LAO-STO remove this paradox. Still, there is no complete theory describing all fundamental aspects of the system. Moreover, the various theories are heavily debated within the field.

Both LAO and STO are perovskites with alternating layers along the (001) direction, as is schematically represented in figure 1.1. For LAO these layers are charged and consist of  $(\text{LaO})^+$  and  $(\text{AlO}_2)^-$  in the ionic limit, while for STO these layers are charge neutral and consist of  $(\text{SrO})^0$  and  $(\text{TiO}_2)^0$ . Due to the charge difference between the layers of LAO and STO a polar discontinuity is present at their interface. Depending on the layer stacking sequence, the interface is either n-type at a  $(\text{LaO})^+ / (\text{TiO}_2)^0$  interface (figure 1.1(a)) or p-type at an  $(\text{AlO}_2)^- / (\text{SrO})^0$  interface (figure 1.1(b)). Only the n-type interface is found to be conducting, while the p-type interface is insulating.

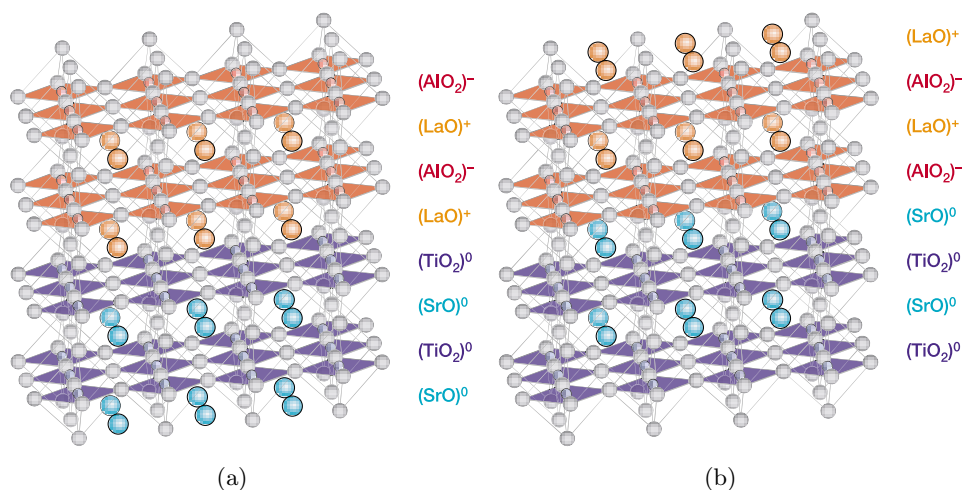


Figure 1.1: A schematic representation of the layers of LAO and STO and both types of LAO-STO interfaces. In (a) the n-type interface is depicted, whereas in (b) the p-type interface is depicted. Figure from reference [2].

The charged layers of LAO on uncharged STO give rise to the so-called polar catastrophe. Due to the alternating charged layers in LAO the electric field alternates between the layers, resulting in a potential that diverges with LAO thickness. This is schematically represented in figure 1.2(a). The diverging potential would build up a large electrostatic potential over the LAO layer, which would result in an unphysical situation. This potential has to be compensated. The suggested mechanism is called electronic reconstruction. This is a process in which half an electron per unit cell is redistributed from the LAO surface to the first few STO layers, doping the n-type interface and making it conducting. In this way the potential remains finite, as can be seen in figure 1.2(b). For p-type interfaces the redistribution of half a hole over the layers was suggested as the reconstruction mechanism, however this is suppressed by the formation of oxygen vacancies. Therefore the p-type interface is not hole doped and the interface remains insulating. [3]

The discussed model of electronic reconstruction is widely used, but it is not the only model to explain the behaviour of the LAO-STO interface. Several other models exist and are debated. One of these models explains the conductivity at the interface by oxygen vacancies in the top layers of STO created during LAO deposition [4]. Another model explains the conductivity by intermixing of La and Sr in STO, resulting in electron doping of the STO [5]. Instead of electronic reconstruction, there is also a model based on a structural reconstruction which leads to charge transfer to the impurity states of STO. These charge carriers are

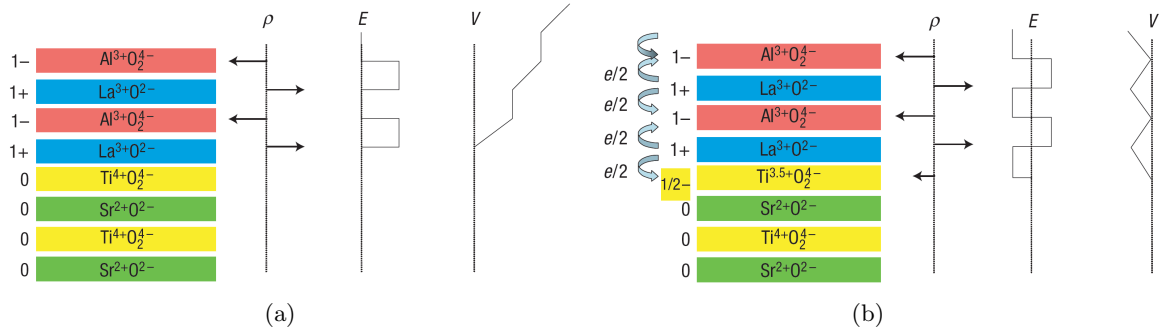


Figure 1.2: A schematic representation of the polar catastrophe (a) at the n-type LAO-STO interface due to the alternating charge of the LAO layers. This can be resolved by an electronic reconstruction (b): half an electron is redistributed to the  $\text{TiO}_2$  layer at the n-type interface. The profiles of the charge ( $\rho$ ), the electric field ( $E$ ) and the potential ( $V$ ) are indicated to clarify the origin and the removal of the polar catastrophe. Figure from reference [3].

activated to the conduction band by the polarization at the interface and thus explain the conductivity [6]. All these models, however, do not explain all features of the LAO-STO system and are not in accordance with all experiments.

The LAO-STO system exhibits some remarkable properties at its interface [7]. A fundamental property is the four unit cell critical thickness of LAO [8]. When only three or less unit cells of LAO are deposited on STO the n-type interface remains insulating. At four unit cells of LAO the LAO-STO interface suddenly becomes conducting. This is explained by the electronic reconstruction model, but this model fails to explain some other effects in the materials system. Another property is the 2D superconductivity of the interface: the interface 2DEG is found to be superconducting when specific growth conditions are used [9]. Also magnetic effects at the LAO-STO interface have been reported [10]. Furthermore, the interface 2DEG can have a very high carrier mobility of more than  $50.000 \text{ cm}^2\text{V}^{-1}\text{s}^{-1}$  [11].

### 1.3 Ferroelectricity and piezoelectricity

Ferroelectric and piezoelectric materials are both dielectrics. This large class of (electrically) insulating solids consists of materials with a number of different properties. All these materials can be polarized in an applied electric field. However, only some of these dielectrics develop also a polarization by applied mechanical stress. These materials are called piezoelectrics and are a subclass of dielectrics. Ferroelectrics, in their turn, are a subclass of piezoelectrics and have the defining property that their spontaneous polarization can be switched by an applied electric field. Furthermore, ferroelectrics are a subclass of pyroelectrics, since the spontaneous polarization of ferroelectrics can be influenced by temperature, which defines this subclass. A ferroelectric material is thus a piezoelectric material with a few additional properties within the shared class of dielectrics, as is schematically represented in figure 1.3. [12]

Ferroelectrics have a spontaneous polarization due to the displacement  $\mathbf{r}$  of ions with charge  $q$  in the unit cell of the ferroelectric. This results in a small dipole moment  $\mathbf{p} = q\mathbf{r}$ . The dipole moment  $\mathbf{p}$  is directed from the negative charge to the positive charge. The multiple dipole moments in a ferroelectric add up to form a total dipole moment. In macroscopic systems, it is therefore easier to work with the total dipole moment per unit volume  $V$ . This

quantity is called the polarization  $\mathbf{P}$  of a ferroelectric and is given by

$$\mathbf{P} = \frac{1}{V} \int \mathbf{p} dV. \quad (1.1)$$

An externally applied electric field can change the displacement of the ions in the unit cell and thus the direction of the dipole moment. This results in an opposite (macroscopic) polarization of the ferroelectric. The polarization in a ferroelectric aligns with the external electric field  $\mathbf{E}$  according to

$$\mathbf{P} = \epsilon_0 \chi \mathbf{E}, \quad (1.2)$$

in which  $\epsilon_0$  is the permittivity of free space and  $\chi$  is the electric susceptibility of the ferroelectric [12]. Due to the alignment of the dipoles, which constitute of a displaced positive and negative charge, the surface of a dielectric is charged. This charge is bound to the surface and its surface charge density is  $\sigma_b = \mathbf{P} \cdot \hat{\mathbf{n}}$ , with  $\hat{\mathbf{n}}$  the normal unitvector. Furthermore, if the ferroelectric is polarized inhomogeneously, there will also be a bound volume charge with density  $\rho_b = -\nabla \cdot \mathbf{P}$ . These bound charge densities give rise to a potential over the ferroelectric which results in an internal electric field [13].

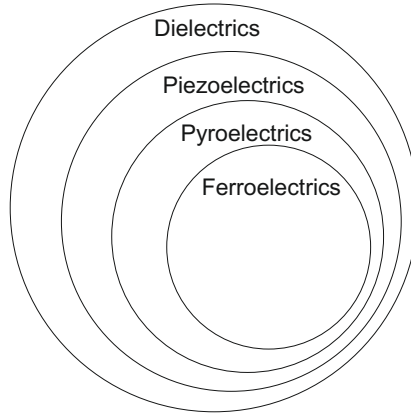


Figure 1.3: An Euler diagram showing the relations between the different classes of dielectrics. The ferroelectrics form the smallest class of dielectric materials.

Ferroelectric materials have two phases: a paraelectric phase and a ferroelectric phase. In both phases the stoichiometry is identical, only the dimensions of the unit cells are changed and/or atoms are displaced. This difference results in different properties of the material. Ferroelectric materials are ferroelectric in the ferroelectric phase, whereas they are only dielectric in the paraelectric phase. This phase change occurs at a certain temperature called the Curie temperature  $T_C$ . At temperatures lower than the Curie temperature the material favours a spontaneous polarization so that the material is ferroelectric. Barium titanate has a Curie temperature of  $T_C = 135^\circ\text{C}$  [14] and is thus ferroelectric at room temperature.

The ferroelectric phase transition can be described with a thermodynamic potential. In the ferroelectric phase this potential has stable minima which correspond to the spontaneous polarization directions of the ferroelectric. Ferroelectric materials can have multiple spontaneous polarization directions. A spatial part of such a material with a single and constant spontaneous polarization direction is called a domain.

As discussed, an externally applied electric field can change the polarization direction to another spontaneous polarization. In the ferroelectric phase the minima of the thermodynamic potential are, however, separated by a barrier. Therefore a small electric field will not change the spontaneous polarization immediately. A high enough electric field lowers this barrier and reduces the minima into a single minimum. This minimum is then the dominant

or even only spontaneous polarization direction. The direction of the electric field determines which of the minima or polarization directions will survive. Due to this barrier the changing of polarization is a hysteretic effect. This hysteresis effect is visible in a plot of polarization versus electric field, as can be seen in figure 1.4. Such a hysteresis loop is commonly called a polarization loop.

A more detailed and more complete discussion of the theory of spontaneous polarization can be found in appendix A.

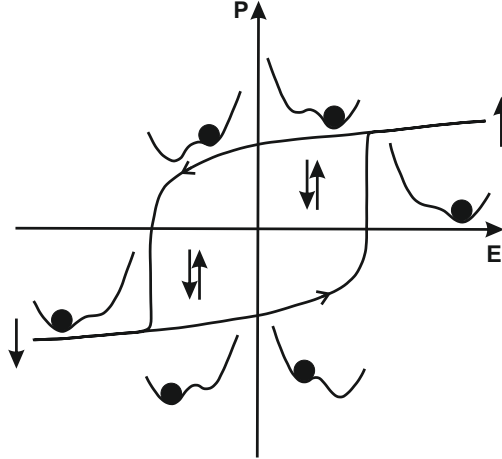


Figure 1.4: A ferroelectric hysteresis loop with schematically shown the form of the thermodynamic potential at specific electric fields. The dot indicates in which polarization state the ferroelectric is in and the arrows indicate the polarization direction(s). Figure after reference [15].

### 1.3.1 Barium titanate

The samples for this project needed a ferroelectric top layer on the LAO-STO system. A suitable ferroelectric was found in barium titanate (BTO), which is just like LAO and STO a perovskite. Furthermore, BTO can be grown ferroelectrically down to layers as thin as 1 nm [16]. The bulk lattice parameters of BTO are also close to the bulk lattice parameters of LAO and STO, see table 1.1. However, the small differences between these lattice parameters induce a compressed strain of approximately 2% in the  $(a,b)$ -plane of the BTO. This value is calculated with the assumption that the thin layer of LAO (10 unit cells) is fully strained on the STO substrate, thus mimicking the STO lattice parameters. A strain of a few percent has in fact been reported to improve the ferroelectricity in the strained BTO unit cells [17]. Only a small part at the bottom of the BTO layer is strained, but still the whole layer is expected to be ferroelectric. For thin films of BTO the lattice parameters strongly depend on the oxygen pressure during deposition and film thickness [18], therefore the strain may be up to 1% higher.

Ferroelectric BTO has a tetragonal crystal structure at room temperature, as can be seen in figure 1.5. Above the Curie temperature of BTO,  $T_C = 135$  °C [14], the crystal is cubic and no longer ferroelectric. In the ferroelectric phase the six  $O^{2-}$  atoms are displaced upward with respect to the eight  $Ba^{2+}$  atoms, the single  $Ti^{4+}$  atom is also slightly displaced upward. This results in a net dipole along the  $c$  axis of the tetragonal BTO unit cell, which in turn leads to a net spontaneous polarization of the crystal. In an anti-parallel electric field the atoms can be forced to be displaced in the opposite direction, reversing the polarization direction. In both polarization directions the  $c$  lattice parameter of the tetragonal unit cell is identical [20].

lattice parameters	STO	LAO	BTO
$a$ (Å)	3.91	3.79	3.99
$b$ (Å)	3.91	3.79	3.99
$c$ (Å)	3.91	3.79	4.04

Table 1.1: Bulk lattice parameters of the used perovskites at room temperature [2, 17]. The actual lattice parameters of the LAO layer in the BTO-LAO-STO system are probably close to the STO parameters due to strain, while the lattice parameters of the actual BTO layer strongly depend on the deposition conditions [19].

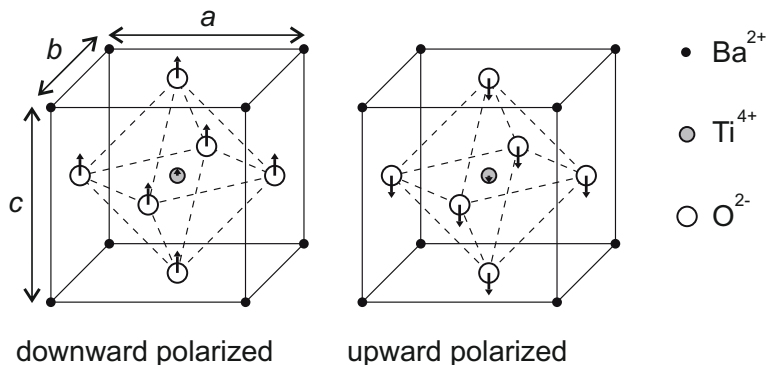


Figure 1.5: The tetragonal BTO unit cell showing the displacements of the atoms for both upward and downward polarization. The lattice parameters  $a$ ,  $b$  and  $c$  of BTO are indicated as the sides of the unit cell. Figure after reference [21].

## 1.4 Ferroelectric control in recent literature

A month before the end of this project an article [22] was issued in which an important part of the goal of this project was claimed. The authors of this communication claimed ferroelectric control of the LAO-STO interface conduction. Instead of BTO the authors have used  $\text{Pb}(\text{Zr}_{0.2}\text{Ti}_{0.8})\text{O}_3$  (PZT) to ferroelectrically influence the electronic properties at the LAO-STO interface 2DEG. The concept is however identical to the one in this project.

The authors have observed a convincing change (two orders of magnitude) of sheet resistance by changing the ferroelectric polarization direction of PZT. This is explained by band bending due to the electric field over the LAO layer induced by the polarization direction of the PZT top layer. When the PZT top layer is upward polarized the band bending results in electron depletion, while for a downward polarized PZT top layer the band bending results in electron accumulation. The sheet resistance also increases with the thickness of as-grown spontaneous upward polarized PZT. Furthermore, they have shown that 3 unit cells LAO on STO, which is just below the critical thickness, can be ferroelectrically pushed over the critical thickness. Switching the polarization can thus induce a 2DEG in insulating LAO-STO.

The experiments described in this article were performed on samples with fairly thin PZT layers. They used thicknesses ranging from 3.5 nm to 40 nm, which is rather thin for PZT, but in principle these can be ferroelectric for the used PZT stoichiometry if the growth conditions are optimized for ferroelectricity. Furthermore, for the characterization of the materials system with scanning tunneling spectroscopy a niobium doped STO substrate was used on which PZT-LAO-STO was grown. Previous experience within the ICE group has revealed that no interface 2DEG is established when LAO is grown on top of deposited STO; the 2DEG is only formed when single-terminated STO substrates are used. The electronic structure and derived quantities are therefore noteworthy, even more because they deviate

from the theoretical calculations in the article itself.

So, has ferroelectric control already been realized? The answer should be: 'partly'. Ferroelectric switching of the 2DEG's sheet resistance seems to be realized indeed, but some questions can still be posed. Furthermore, additional measurements would be appreciated. For example, no carrier density and carrier mobility data are presented in the article. This would be interesting for comparing their LAO-STO samples with other work and would completely characterize the ferroelectric control. Apart from this, but in connection with the research project of this thesis, it would be interesting to determine the strength of the spin-orbit coupling for both polarization directions at the LAO-STO 2DEG in these samples.

## 1.5 Outline

Now the central concepts and materials systems have been introduced and briefly discussed. The next chapter discusses the theoretical background of this research project in detail to elucidate spin-orbit coupling and Majorana physics. This chapter will help to understand the physical interest in the current materials system. The next chapter discusses theoretically the principles of piezoresponse force microscopy, a much used technique in this research project. Since the results of this measuring technique are found to be often complicated to interpret during this research, a whole chapter is devoted to explain some important basic principles of piezoresponse force microscopy. Furthermore, in the appendices a short user guide on piezoresponse force microscopy can be found as well as a more detailed description of the theory of spontaneous polarization. After these theoretical chapters two experimental chapters, the heart of this research project, are presented. The first discusses the fabrication and characterization of the different samples used, while the second presents and discusses the analysis of ferroelectricity and its effects in the current materials system. This master thesis is ended with conclusions and recommendations.



## Chapter 2

# Theoretical background of spin-orbit interactions and Majorana physics

This project is partly initiated by an interest in the LAO-STO system as a possible system for detecting Majorana fermions. In this chapter the relevant theory is discussed for understanding this interest. To that end the physics of spin-orbit interaction and the main theoretical aspects of Majorana physics are presented.

### 2.1 Origin of spin-orbit interactions

A spin-orbit interaction is a coupling between the spin of an electron and its orbital motion. Such an interaction shifts the energy levels of an electron in an atom. This correction to the energy levels is in fact a relativistic correction, due to the relativistic speed of the electron. There are different types of spin-orbit interactions. These will appear from a relativistic quantum mechanical approach. The following theoretical discussion is based upon references [23, 24, 25, 26].

Many quantum mechanical considerations are based upon the Schrödinger equation. However, the Schrödinger equation is a non-relativistic equation. As soon as fermions with relativistic speeds are involved, as is the case with spin-orbit interactions, one needs to use the Dirac equation instead. The Dirac equation is also a wave equation, but it is consistent with both quantum mechanics and special relativity. The Dirac equation for free particles is given by

$$(c\boldsymbol{\alpha} \cdot \mathbf{p} + \beta mc^2) \Psi = E\Psi. \quad (2.1)$$

In which  $\boldsymbol{\alpha}$  is the matrix

$$\boldsymbol{\alpha} = \begin{pmatrix} 0 & \boldsymbol{\sigma} \\ \boldsymbol{\sigma} & 0 \end{pmatrix}, \quad (2.2)$$

with  $\boldsymbol{\sigma}$  vectors consisting of the well-known Pauli spin matrices  $\sigma_x$ ,  $\sigma_y$  and  $\sigma_z$ . The  $\beta$  in the Dirac equation is defined as

$$\beta = \begin{pmatrix} \mathbb{1} & 0 \\ 0 & -\mathbb{1} \end{pmatrix}, \quad (2.3)$$

with  $\mathbb{1}$  the identity matrix. The wave vector  $\Psi$  is in fact a bispinor and consists of a particle (electron) spinor  $\phi$  and a antiparticle (hole) spinor  $\xi$ .

The Dirac equation must be slightly modified when electromagnetic fields are present, as is the case with bound particles. This is done by the replacement of  $\mathbf{p} \rightarrow (\mathbf{p} - \varepsilon\mathbf{A})$  and the addition of the (lattice) potential  $\varepsilon\Phi$ . The Dirac equation is thus given by

$$(c\boldsymbol{\alpha} \cdot (\mathbf{p} - \varepsilon\mathbf{A}) + \beta mc^2 + \varepsilon\Phi) \Psi = E\Psi, \quad (2.4)$$

with  $\mathbf{A}$  the vector potential and  $\varepsilon$  the charge of the particle, e.g. for electrons  $\varepsilon = -e$ . In the rest of this section  $\mathbf{p}$  will be used in stead of  $(\mathbf{p} - \varepsilon\mathbf{A})$  to make the notation less cumbersome. The reader should however keep in mind that  $\mathbf{p}$  should be expanded as discussed.

To find the explicit contribution from spin-orbit interaction to the Hamiltonian, one has to separate the time and space variables of the wave vector  $\Psi(\mathbf{r}, t)$  and thus of its two spinors  $\phi(\mathbf{r}, t)$  and  $\xi(\mathbf{r}, t)$ . To separate the time and space variables the wave vector can be explicitly written as

$$\Psi(\mathbf{r}, t) = e^{-\frac{i}{\hbar}Et} \begin{pmatrix} \phi(\mathbf{r}) \\ \xi(\mathbf{r}) \end{pmatrix}. \quad (2.5)$$

When putting this wave vector in equation (2.4) the time dependence will cancel out of the equation. Multiplying all matrices and vectors results in:

$$E \begin{pmatrix} \phi(\mathbf{r}) \\ \xi(\mathbf{r}) \end{pmatrix} = c \begin{pmatrix} \boldsymbol{\sigma} \cdot \mathbf{p} \xi(\mathbf{r}) \\ \boldsymbol{\sigma} \cdot \mathbf{p} \phi(\mathbf{r}) \end{pmatrix} + mc^2 \begin{pmatrix} \phi(\mathbf{r}) \\ -\xi(\mathbf{r}) \end{pmatrix} + \varepsilon\Phi \begin{pmatrix} \phi(\mathbf{r}) \\ \xi(\mathbf{r}) \end{pmatrix}. \quad (2.6)$$

This gives a set of two coupled equations, which can be solved by putting the one into the other. Solving the second (lower) equation first, gives an expression for  $\xi(\mathbf{r})$ :

$$\xi(\mathbf{r}) = \frac{c(\boldsymbol{\sigma} \cdot \mathbf{p})}{\tilde{E} - V + 2mc^2} \phi(\mathbf{r}). \quad (2.7)$$

In which  $\tilde{E} \equiv E - mc^2$  and  $V \equiv \varepsilon\Phi$ . Putting this result in the first (upper) equation gives an equation in  $\phi(\mathbf{r})$  only:

$$(\boldsymbol{\sigma} \cdot \mathbf{p}) \left[ \frac{c^2}{\tilde{E} - V + 2mc^2} \right] (\boldsymbol{\sigma} \cdot \mathbf{p}) \phi(\mathbf{r}) = (\tilde{E} - V) \phi(\mathbf{r}). \quad (2.8)$$

Up to now every result was exact. Now the term in square brackets will be approximated up to order  $\frac{\tilde{E}-V}{2mc^2} \approx \left(\frac{v}{c}\right)^2$ . This is done by a Taylor expansion around the point  $\tilde{E} = V$ . Up to first order in  $\left(\frac{v}{c}\right)^2$  this will give

$$\left[ \frac{c^2}{\tilde{E} - V + 2mc^2} \right] \approx \frac{1}{2m} \left[ 1 - \frac{\tilde{E} - V}{2mc^2} \right]. \quad (2.9)$$

This simplifies equation (2.8), but there is another problem with this equation. The full wave vector  $\Psi(\mathbf{r}, t)$  was correctly normalized, however the constituent spinor  $\phi(\mathbf{r})$  is not. The correctly normalized wave vector  $\psi(\mathbf{r})$  for equation (2.8) can be found by solving

$$\int \left( \phi^\dagger(\mathbf{r})\phi(\mathbf{r}) + \xi^\dagger(\mathbf{r})\xi(\mathbf{r}) \right) d^3\mathbf{r} = \int (a\phi(\mathbf{r}))^\dagger (a\phi(\mathbf{r})) d^3\mathbf{r} = \int \psi^\dagger(\mathbf{r})\psi(\mathbf{r}) d^3\mathbf{r} = 1. \quad (2.10)$$

One would then find:

$$\psi(\mathbf{r}) = \sqrt{1 + \left(\frac{\mathbf{p} \cdot \boldsymbol{\sigma}}{2mc}\right)^2} \phi(\mathbf{r}) \approx \left\{ 1 + \frac{(\mathbf{p} \cdot \boldsymbol{\sigma})^2}{8m^2c^2} \right\} \phi(\mathbf{r}), \quad (2.11)$$

which should be substituted for  $\phi(\mathbf{r})$  in equation (2.8). From here  $\mathbf{p}$  will be expanded according to the transformation  $\mathbf{p} \rightarrow (\mathbf{p} - \varepsilon\mathbf{A})$ , as was discussed previously.

Using the approximation of equation (2.9) and the normalized wave vector of equation (2.11) in equation (2.8), one will arrive at an equation known as the Pauli equation. To arrive there one needs to factor the different terms with the aid of some mathematical identities<sup>1</sup>. The Pauli equation is then given by

$$\left\{ \frac{p^2}{2m} + V + \frac{e\hbar}{2m} \boldsymbol{\sigma} \cdot \mathbf{B} - \frac{e\hbar}{4m^2c^2} \boldsymbol{\sigma} \cdot (\mathbf{p} \times \mathbf{E}) - \frac{e\hbar^2}{8m^2c^2} \nabla \cdot \mathbf{E} - \frac{p^4}{8m^3c^2} - \frac{e\hbar p^2}{4m^3c^2} \boldsymbol{\sigma} \cdot \mathbf{B} - \frac{e^2\hbar^2 B^2}{8m^3c^2} \right\} \psi = \tilde{E}\psi. \quad (2.12)$$

<sup>1</sup>To be more explicit:  $(\boldsymbol{\sigma} \cdot \mathbf{a})(\boldsymbol{\sigma} \cdot \mathbf{b}) = \mathbf{a} \cdot \mathbf{b} + i\boldsymbol{\sigma} \cdot (\mathbf{a} \times \mathbf{b})$  and  $\nabla \times \mathbf{A}\phi + \mathbf{A} \times \nabla\phi = (\nabla \times \mathbf{A})\phi = \mathbf{B}\phi$ .

The third term on the left-hand side of this equation is known as the Zeeman term. The fourth term on the left-hand side is also an important contribution to the Hamiltonian due to spin-orbit interaction and is called the Pauli term. This spin-orbit interaction is known as Pauli spin-orbit coupling. The fifth term is known as the Darwin term and is not a spin-orbit interaction. The next terms are higher-order (relativistic) corrections, for example to the kinetic energy (sixth term) and the Zeeman term (seventh term). This term is however of no particular importance to spin-orbit coupling, since it is an order of  $(\frac{v}{c})^2$  smaller than the Zeeman term.

## 2.2 Symmetry and symmetry breaking

Symmetry and symmetry breaking have an important effect on spin-orbit coupling. Therefore two types of symmetry are reviewed in this section: time reversal symmetry and inversion symmetry. The theory in this section is based upon references [23, 24, 26, 27, 28, 29, 30].

### 2.2.1 Time reversal symmetry

Time reversal is a discrete symmetry transformation in which the time  $t$  is transformed to time  $-t$  or mathematically:  $t \rightarrow -t$ . This transformation does not cause a system to go back in time, but to reverse its motion. The term time reversal can therefore be seen as a misnomer and could better be termed motion reversal [27].

In quantum mechanics the time reversal transformation is given by an antiunitary operator  $\hat{T}$ . This means that the operator  $\hat{T}$  has the two defining properties of antiunitarity:

1. it is antilinear:  $\hat{T}(c_1\tilde{\psi}_1 + c_2\tilde{\psi}_2) = c_1^*\hat{T}\tilde{\psi}_1 + c_2^*\hat{T}\tilde{\psi}_2$ ;
2. it obeys:  $(\hat{T}\tilde{\psi}, \hat{T}\tilde{\phi}) = (\tilde{\phi}, \tilde{\psi})$ .

For a spin- $\frac{1}{2}$  particle, such as an electron, this antiunitary time reversal operator is given by

$$\hat{T} = -i\sigma_y\hat{K}, \quad (2.13)$$

in which  $\sigma_y$  is the Pauli spin matrix for spins in the  $y$  direction and  $\hat{K}$  is the complex conjugation operator. The complex conjugation operator  $\hat{K}$  performs the antiunitary operation  $\hat{K}\tilde{\phi} = \tilde{\phi}^*$ . Applying this operator  $\hat{T}$  on the wave function  $\tilde{\Psi}(\mathbf{r}, t) = e^{-i(E/\hbar)t}\tilde{\psi}(\mathbf{r})$  will result in

$$\hat{T}\tilde{\Psi}(\mathbf{r}, t) = -i\sigma_y e^{-i(E/\hbar)(-t)}\tilde{\psi}^*(\mathbf{r}), \quad (2.14)$$

which shows that the time is 'reversed' indeed. The prefactor  $-i\sigma_y$  seems to be a bit arbitrary now, but it makes good sense when the spin is explicitly treated, since it causes the spin to flip.

The time reversal operator in equation (2.13) is defined to force the spin angular momentum  $\mathbf{S}$  to be non-invariant under time reversal, i.e.  $\hat{T}\mathbf{S}\hat{T}^{-1} = -\mathbf{S}$ . This makes sense, because reversing the time (reversing the motion) would also change the rotation of the electron and thus flipping its spin angular momentum<sup>2</sup>. The orbital angular momentum  $\mathbf{L}$  is already non-invariant under complex conjugation, so  $\mathbf{L}$  is also non-invariant under the time reversal operator defined in equation (2.13). Then from  $\mathbf{J} = \mathbf{L} + \mathbf{S}$ , the total angular momentum is also non-invariant under time reversal. Other important quantities that are non-invariant are velocity  $\mathbf{v}$  (hence motion reversal), momentum  $\mathbf{p}$  and magnetic field  $\mathbf{B}$ . The latter and the invariance of the electric field  $\mathbf{E}$  ensure that all Maxwell equations and the Lorentz force law are invariant under time reversal. The position  $\mathbf{r}$  is also invariant under time reversal, since the reversing motion of a particle does not change its position instantaneously.

---

<sup>2</sup>This argument is good to get a feeling of the situation, but the idea of a rotating electron resulting in a spin is more a semi-classical analogy than hard quantum mechanics.

Having defined the time reversal operator  $\hat{T}$  for one spin- $\frac{1}{2}$  particle, it is good to look at  $N$  spin- $\frac{1}{2}$  particles and the implications of time reversal. For  $N$  spin- $\frac{1}{2}$  particles the time reversal operator changes to

$$\hat{T} = \left(-i\sigma_y^{(1)}\right) \left(-i\sigma_y^{(2)}\right) \dots \left(-i\sigma_y^{(N)}\right) \hat{K}, \quad (2.15)$$

so that

$$\hat{T}^2 = (-1)^N. \quad (2.16)$$

This has a profound implication when the Hamiltonian of a system commutes with the time reversal operator,  $[\hat{T}, H] = 0$ , which means that the Hamiltonian of that system is invariant under time reversal. This implication is known as Kramers degeneracy. From the second property of antiunitarity and equation (2.16) it can be shown that the states  $\tilde{\psi}$  and  $\hat{T}\tilde{\psi}$  are orthogonal for that system if it has an odd number of spin- $\frac{1}{2}$  particles  $N$ . Since the Hamiltonian of such a system is invariant under time reversal, the states  $\tilde{\psi}$  and  $\hat{T}\tilde{\psi}$  have the same energy. All eigenstates of the system must therefore be at least two-fold degenerate, independent of the external electric field. Only an applied external magnetic field, which is non-invariant under time reversal, can break the invariance or symmetry of the Hamiltonian and lift the Kramers degeneracy.

The Pauli equation is an example of a time reversal invariant Hamiltonian. This can be proven formally, but a look at equation (2.12) will be convincing. As was mentioned, the quantities  $\mathbf{p}$ ,  $\mathbf{B}$  and  $\mathbf{S}$  are non-invariant under time reversal, whereas  $\mathbf{E}$  is invariant. Since  $\mathbf{S}$  is non-invariant, also  $\boldsymbol{\sigma}$  is non-invariant. Also, since  $\mathbf{E}$  is invariant,  $V$  is invariant too. Then none of the terms in equation (2.12) acquire a minus sign, so that the whole Hamiltonian is invariant under time reversal. Therefore the Pauli equation suffers from the Kramers degeneracy, which can be expressed as:

$$E(\mathbf{k}, \uparrow) = E(-\mathbf{k}, \downarrow). \quad (2.17)$$

This means that under time reversal symmetry (invariance) both the wave vector  $\mathbf{k}$  as the spin are degenerate.

### 2.2.2 Inversion symmetry

Inversion symmetry, also known as parity, is a discrete symmetry transformation which is more intuitive than time reversal symmetry. A transformation under parity changes the space or position vector from position  $\mathbf{r}$  to position  $-\mathbf{r}$  or mathematically:  $\mathbf{r} \rightarrow -\mathbf{r}$ . This is the same as stating that a right-handed coordinate system transforms under parity to a left-handed coordinate system. The whole coordinate system is then inverted around the origin, which is then called the inversion center. Centrosymmetric crystals have such an inversion center and are thus inversion symmetric and invariant under parity.

An inversion symmetry transformation can be formally expressed with the unitary parity operator  $\hat{P}$ . This simple operator is given by

$$\hat{P} = -\mathbb{1}, \quad (2.18)$$

in which  $\mathbb{1}$  is the three-dimensional identity matrix. So that in Dirac notation  $\hat{P}|\mathbf{r}\rangle = -|\mathbf{r}\rangle$ . Since operating  $\hat{P}$  twice on a state or quantity will bring that state or quantity back to its original coordinate system, it will be clear that  $\hat{P}^2 = 1$ . Therefore  $\hat{P}$  has eigenvalues  $\pm 1$  and states or quantities can be either even (invariant) or odd (non-invariant) under inversion symmetry (parity).

Some important quantities that are non-invariant under inversion symmetry are the electric field  $\mathbf{E}$ , the velocity  $\mathbf{v}$ , the momentum  $\mathbf{p}$  and the wave vector  $\mathbf{k}$ . However, the magnetic

field  $\mathbf{B}$ , the spin  $\mathbf{S}$  and the energy of a state  $E$  are invariant under inversion symmetry. This means that there can be two states with the same energy. For spin- $\frac{1}{2}$  particles under parity this can be stated as

$$E(\mathbf{k}, \uparrow) = E(-\mathbf{k}, \uparrow), \quad (2.19)$$

with the  $\uparrow$  indicating that the spin can be either both up or both down. Due to the space inversion symmetry there is a two-fold degeneracy.

Within centrosymmetric crystals the inversion symmetry is even or, as mentioned before, invariant. However, in these crystals the inversion symmetry can be broken. One obvious location at which the inversion symmetry is broken, is the surface of a crystal. Here the transformation  $\mathbf{r} \rightarrow -\mathbf{r}$  can no longer hold. This is also true for an interface between materials. Furthermore, the inversion symmetry can be broken by an electric field, since ions within the crystal will be displaced, leading to a structural change. Also the potential  $V$  will change, up to lowest order in  $\mathbf{r}$  the potential can be approximated as  $V(\mathbf{r}) = V_0 + e\mathbf{E} \cdot \mathbf{r}$ , with  $V_0$  the unperturbed lattice potential. There will be no center of inversion anymore and the degeneracy is lifted [24].

## 2.3 Rashba spin-orbit coupling

This specific type of spin-orbit coupling is strongly related to Pauli spin-orbit coupling. Pauli spin-orbit coupling is a result of the Pauli term in the relativistic approximation of the Dirac equation, as was discussed in section 2.1. This Pauli term  $H_P$  was given in equation (2.12) as

$$H_P = -\frac{e\hbar}{4m^2c^2} \boldsymbol{\sigma} \cdot (\mathbf{p} \times \mathbf{E}). \quad (2.20)$$

In the special case that time-reversal symmetry is preserved and the inversion symmetry is broken, one speaks of Rashba spin-orbit coupling instead. Under these conditions the spin degeneracy is lifted [28]:

$$E(\mathbf{k}, \uparrow) \neq E(\mathbf{k}, \downarrow). \quad (2.21)$$

This means that even without an externally applied magnetic field, Rashba spin-orbit coupling lifts the spin degeneracy. Another consequence of only having time reversal symmetry can be seen from equation (2.17). Electrons within the same energy state  $E$  have a spin up when they move to the  $+\mathbf{k}$  direction and a spin down when they move in the  $-\mathbf{k}$  direction.

The standard notation of the Rashba Hamiltonian differs somewhat from the Pauli term in equation (2.20). The electric field  $\mathbf{E}$  in this equation depends on the potential  $V(\mathbf{r})$  according to  $\mathbf{E} = -\nabla V(\mathbf{r})$ . If one applies the electric field in the  $z$  direction, as is often the case when 2DEG's are considered, the electric field is given by  $\mathbf{E} = -\frac{dV(z)}{dz} \hat{\mathbf{z}}$ . A gate voltage  $V(z)$  can then be used to control the spin-orbit coupling [30]. The Rashba spin-orbit coupling is then given by<sup>3</sup>:

$$H_R = \frac{\alpha_R}{\hbar} (\boldsymbol{\sigma} \times \mathbf{p}) \cdot \hat{\mathbf{z}}. \quad (2.22)$$

In this equation is  $\alpha_R$  the Rashba coefficient, a parameter that determines the strength of the Rashba spin-orbit coupling and is proportional to the gradient of the potential [29]:

$$\alpha_R = \frac{e\hbar^2}{4m^2c^2} \frac{dV(z)}{dz}. \quad (2.23)$$

---

<sup>3</sup>If one is wondering why the outer product is different than in the Pauli term: to arrive here from equation (2.20) one has to use the mathematical identities  $\mathbf{a} \cdot (\mathbf{b} \times \mathbf{c}) = (\mathbf{b} \times \mathbf{c}) \cdot \mathbf{a} = (\mathbf{a} \times \mathbf{b}) \cdot \mathbf{c}$ .

## 2.4 Effects of Rashba spin-orbit coupling and Zeeman interaction on 2DEG's

Different types of spin-orbit coupling can be present in the same system. This is obvious from the Pauli equation in equation (2.12), in which the Pauli term and the Zeeman term were connected to spin-orbit interactions. In the previous section, Rashba spin-orbit coupling was related to this Pauli term when time-reversal symmetry was preserved and inversion symmetry was broken. In this section the combined effect of Rashba spin-orbit coupling and Zeeman interaction on 2DEG's is considered, based upon references [24, 26, 31, 32].

The Zeeman term  $H_Z$  is given by

$$H_Z = \alpha_Z (\boldsymbol{\sigma} \cdot \mathbf{B}), \quad (2.24)$$

in analogy with the Rashba coefficient  $\alpha_Z$  is termed the Zeeman coefficient and is introduced for notational convenience. The Zeeman coefficient consist of physical constants only and is defined as

$$\alpha_Z \equiv \frac{e\hbar}{2m}. \quad (2.25)$$

The effects of Rashba spin-orbit coupling and Zeeman interaction in 2DEG's can be calculated analytically within the free electron model. The Hamiltonian of an electron within a 2DEG and with both types of interactions is given by:

$$H_{SO} = \frac{p^2}{2m} - \mu + \frac{\alpha_R}{\hbar} (\sigma_x p_y - \sigma_y p_x) + \alpha_Z \sigma_z B_z. \quad (2.26)$$

In this equation the Rashba term of equation (2.22) is written out explicitly in the Pauli matrices and the momentum in the  $x$  and  $y$  directions. For the Zeeman term the magnetic field is assumed to be in the  $z$  direction, as is common practice for 2DEG's, forcing the Pauli matrix to be in the  $z$  direction too. The chemical potential  $\mu$  is explicitly introduced. The expression in equation (2.26) is the spin-orbit Hamiltonian for 2DEG's.

The time-independent Schrödinger equation,  $H\psi = E\psi$ , can now be solved with this spin-orbit Hamiltonian. To do this, the spin-orbit Hamiltonian is written as a matrix:

$$H_{SO} = \begin{pmatrix} \frac{\hbar^2}{2m} (k_x^2 + k_y^2) - \mu + \alpha_Z B_z & \alpha_R (k_y + ik_x) \\ \alpha_R (k_y - ik_x) & \frac{\hbar^2}{2m} (k_x^2 + k_y^2) - \mu - \alpha_Z B_z \end{pmatrix}. \quad (2.27)$$

In which the relation  $\mathbf{p} = \hbar\mathbf{k}$  is used. The eigenvalues of this matrix Hamiltonian can be obtained by solving  $\det(H - E\mathbb{1}) = 0$ , resulting in:

$$E_{\pm} = \frac{\hbar^2 k_{\parallel}^2}{2m} - \mu \pm \sqrt{(\alpha_R k_{\parallel})^2 + (\alpha_Z B_z)^2}. \quad (2.28)$$

From this expression it is clear that the degeneracy is lifted. The wave vectors  $k_{\parallel}$  are the in plane wave vectors of the 2DEG,  $k_{\parallel} = \sqrt{k_x^2 + k_y^2}$ . The energy levels are displaced now by  $\Delta E = \sqrt{\Delta_R^2 + \Delta_Z^2}$ , with  $\Delta_R = 2\alpha_R k_{\parallel}$  the momentum dependent lift of the bands due to Rashba spin-orbit coupling and  $\Delta_Z = 2\alpha_Z B_z$  the gap at  $k_{\parallel} = 0$  due to Zeeman interaction. Furthermore, Rashba spin-orbit coupling has shifted the bands along the  $k_{\parallel}$  axis by  $\Delta k_R = \frac{2m}{\hbar^2} \alpha_R$ . These features can be seen in figure 2.1.

Now the wave functions  $\psi$  can be determined. To do this, the wave function is separated into a spatial part and a spin part, in Dirac notation:

$$|\psi\rangle = |\mathbf{k}\rangle \otimes |\chi\rangle. \quad (2.29)$$

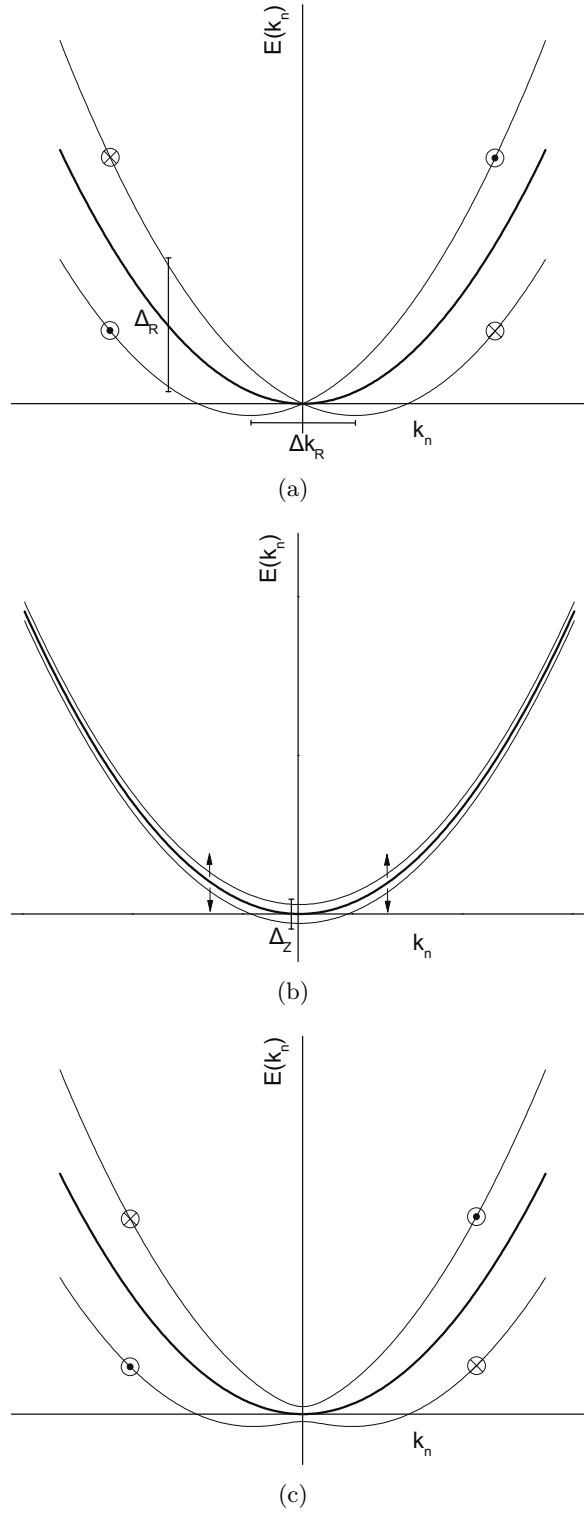


Figure 2.1: The dispersion relations of electrons in a 2DEG for  $\mu = 0$  with wave vector  $k_n$ , where  $n \in \{x, y\}$ . In (a) the effect of Rashba spin-orbit coupling is depicted, in (b) the effect of the Zeeman interaction is depicted and in (c) the combined effect of Rashba spin-orbit coupling and Zeeman interaction is depicted. The bold curve is the spin degenerate dispersion relation when none of the interactions is present. When at least one of both interactions is present, the spin degeneracy is lifted, resulting in the two thinner curves for each spin state. The arrows indicate the spin direction as well as the dot (out-of-paper) and cross (into-paper).

In which  $|\chi\rangle$  is the spin ket and  $|\mathbf{k}\rangle$  a wave vector state. Furthermore, the wave vector  $\mathbf{k}$  can be conveniently expressed in circular coordinates as  $\mathbf{k} = k \langle \cos \varphi, \sin \varphi, 0 \rangle$ . In this description the wave vector rotates with angle  $\varphi$  in plane of the 2DEG. Writing this description in complex notation the spin-orbit Hamiltonian becomes:

$$H_{SO} = \begin{pmatrix} \frac{\hbar^2 k^2}{2m} - \mu + \alpha_Z B_z & i\alpha_R k e^{-i\varphi} \\ -i\alpha_R k e^{i\varphi} & \frac{\hbar^2 k^2}{2m} - \mu - \alpha_Z B_z \end{pmatrix}. \quad (2.30)$$

Solving  $\det(H_{SO} - E_{\pm}\mathbb{1}) = 0$  will give the spin kets for the spin-orbit Hamiltonian. Correctly normalized, these are:

$$|\chi_{\pm}\rangle = \frac{1}{\sqrt{1 + \Gamma_{\pm}^2}} \begin{pmatrix} -ie^{-i\varphi} \\ \Gamma_{\pm} \end{pmatrix}, \quad (2.31)$$

in which  $\Gamma_{\pm} \equiv \left( \frac{\Delta_Z \pm \Delta E}{\Delta_R} \right)$ .

With these spin kets the directions of the spin  $\mathbf{n}$  can be calculated by projecting the Pauli spin matrices on the spin ket basis:

$$\mathbf{n}_{\pm} = \langle \chi_{\pm} | \boldsymbol{\sigma} | \chi_{\pm} \rangle. \quad (2.32)$$

In this equation the vector  $\mathbf{n}_-$  denotes the spin-down direction and the vector  $\mathbf{n}_+$  denotes the spin-up direction. With the spinors in equation (2.31) the spin directions are given by the vector  $\mathbf{n}_{\pm} = \frac{2\Gamma_{\pm}}{1 + \Gamma_{\pm}^2} \langle -\sin \varphi, \cos \varphi, 0 \rangle$ . When one compares the spin directions with the wave vector, it becomes clear that both are orthogonal, i.e.  $\mathbf{k} \cdot \mathbf{n}_{\pm} = 0$ . The directions of the spin are thus related by the wave vector as

$$\mathbf{n}_{\pm} = - \left( \frac{2\Gamma_{\pm}}{1 + \Gamma_{\pm}^2} \right) \hat{\mathbf{k}} \times \hat{\mathbf{z}}, \quad (2.33)$$

in which  $\hat{\mathbf{k}}$  is the unit wave vector.

Since the spin kets are known, the full wave functions can now be given:

$$|\psi_{\pm}\rangle = \frac{e^{i\mathbf{k} \cdot \mathbf{r}}}{\sqrt{(1 + \Gamma_{\pm}^2) S}} (|\uparrow\rangle + i\Gamma_{\pm} e^{i\varphi} |\downarrow\rangle). \quad (2.34)$$

Here the spin kets are written differently by multiplying  $|\chi_{\pm}\rangle$  in equation (2.31) by  $ie^{i\varphi}$  for clarity. The states  $|\uparrow\rangle$  and  $|\downarrow\rangle$  denote the spin-up state (1, 0) and the spin-down state (0, 1), respectively. Furthermore, use was made of the representation  $\langle \mathbf{r} | \mathbf{k} \rangle = \frac{1}{\sqrt{S}} e^{i\mathbf{k} \cdot \mathbf{r}}$ , in which  $S$  is the area of the 2DEG.

## 2.5 The role of spin-orbit coupling in Majorana physics

Majorana physics describes the physics behind the Majorana particle, which can be thought of as half a normal fermion. In fact, a fermion is a superposition of two spatially separated Majorana fermions [1]. One remarkable property of this particle is that it is also its own antiparticle. In solid state physics one usually defines a Majorana particle as an equal superposition of an electron and a hole. Such a superposition is described in the field of superconductivity by Bogoliubov quasiparticles. Excitations of superconducting states are therefore a natural candidate to look for Majorana fermions. In second quantization notation these properties can be cast in the Majorana fermion creation operator  $\hat{\gamma}^{\dagger}$  as

$$\hat{\gamma}^{\dagger} = \bar{u}\hat{c}_{\sigma} + u\hat{c}_{\sigma}^{\dagger}, \quad (2.35)$$

in which  $\hat{c}_\sigma$  is a hole creation operator,  $\hat{c}_\sigma^\dagger$  is an electron creation operator and  $u$  is a Bogoliubov coefficient. This operator is Hermitian, so that  $\hat{\gamma}^\dagger = \hat{\gamma}$ , proving that the Majorana fermion is its own antiparticle [1].

Theoretically it was predicted that Majorana fermions indeed can be found in some types of superconductors [1, 33]. They should occur in spinless superconductors with  $p$ -wave pairing symmetry. However,  $p$ -wave superconductors are rare in nature. Luckily,  $p$ -wave-like pairing can be engineered from common  $s$ -wave superconductors through the proximity effect. This effect is common for superconductors in contact with non-superconductors and is due to the leakage of Cooper pairs<sup>4</sup> into the non-superconducting material [34]. Apart from the proximity effect, strong spin-orbit coupling is essential to induce a superconducting interface with  $p$ -wave-like pairing.

The spin-orbit Hamiltonian for a 2D system is given by

$$\mathcal{H}_{SO} = \sum_{\sigma=\uparrow,\downarrow} \int d^2\mathbf{r} \psi_\sigma^\dagger(\mathbf{r}) \mathcal{H}_{SO}(\mathbf{r}) \psi_\sigma(\mathbf{r}), \quad (2.36)$$

in which the spin-orbit Hamiltonian of equation (2.26) is used. The wave vectors  $\psi_\uparrow(\mathbf{r})$  and  $\psi_\downarrow(\mathbf{r})$  are linear combinations of equation (2.34) so that one spin state is selected.

The superconducting pairing potential  $\Delta$  can be proximity induced in the 2DEG and adds a superconducting multiple particle Hamiltonian to the system. This Hamiltonian is approximated (mean-field) by

$$\mathcal{H}_S = \int d^2\mathbf{r} d^2\mathbf{r}' \psi_\downarrow(\mathbf{r}) \Delta(\mathbf{r}, \mathbf{r}') \psi_\uparrow(\mathbf{r}') + H.c., \quad (2.37)$$

wherein  $H.c.$  denotes the Hermitian conjugates of the preceding terms.

Combining both Hamiltonians, the total Hamiltonian of the system is obtained:  $\mathcal{H}_{BdG} = \mathcal{H}_{SO} + \mathcal{H}_S$ . This Hamiltonian is central to the theory of Majorana physics. It is usually described in the Nambu particle-hole space, in which the wave functions transform to include both electrons and holes explicitly:

$$\bar{\Psi}(\mathbf{r}) = \begin{pmatrix} \psi_\uparrow(\mathbf{r}) \\ \psi_\downarrow(\mathbf{r}) \\ \psi_\downarrow^\dagger(\mathbf{r}) \\ -\psi_\uparrow^\dagger(\mathbf{r}) \end{pmatrix}. \quad (2.38)$$

Within this Nambu space the Hamiltonian can then be given as

$$\mathcal{H}_{BdG} = \frac{1}{2} \int d^2\mathbf{r} d^2\mathbf{r}' \bar{\Psi}^\dagger(\mathbf{r}) \begin{pmatrix} \mathcal{H}_{SO}(\mathbf{r}) \delta(\mathbf{r} - \mathbf{r}') & \Delta^*(\mathbf{r}, \mathbf{r}') \\ \Delta(\mathbf{r}, \mathbf{r}') & -\sigma_y \mathcal{H}_{SO}^*(\mathbf{r}) \sigma_y \delta(\mathbf{r} - \mathbf{r}') \end{pmatrix} \bar{\Psi}(\mathbf{r}), \quad (2.39)$$

where  $-\sigma_y \mathcal{H}_{SO}^*(\mathbf{r}) \sigma_y$  is  $\mathcal{H}_{SO}$  time-reversed, so that it operates on holes – which are time-reversed electrons. If the superconducting pairing potential introduces spinless  $p$ -wave-like pairing to this Hamiltonian, then its zero-energy solution describes a Majorana fermion [1]. Bringing an  $s$ -wave superconductor in contact with the 2DEG will be sufficient, since intra-band  $p_x \pm ip_y$  pairing will be induced by the proximity effect [35].

The spin-orbit Hamiltonian describes a gapped Dirac point at sufficiently small momenta [35]. Inside this gap there is only one effective spin direction. Induced spinless superconductivity can be achieved when the chemical potential is placed inside the gap, therefore  $|B_z| > \mu$ . Furthermore, if  $\Delta$  is small and  $|B_z| > \sqrt{\Delta^2 + \mu^2}$  the superconducting state is topological and Majorana edge states appear [1].

<sup>4</sup>The leakage of Cooper pairs is in fact a boundary effect: a superconducting wave function cannot abruptly end at the interface.

### 2.5.1 Majorana physics in the LAO-STO system

The LAO-STO system is an interesting system to study in this respect, since the 2DEG itself can be made superconducting at temperatures below  $T_C \cong 200$  mK [9] when the right growth conditions are used. Furthermore, due to the broken inversion symmetry and polar interface in the LAO-STO system a strong and tunable Rashba spin-orbit coupling was reported in this materials system [36]. Moreover, this Rashba spin-orbit coupling can be enhanced by the polarization of a ferroelectric material grown on LAO-STO. This polarization creates an electric field and a potential difference over the LAO-STO interface, which is proportional to the Rashba coefficient according to equation (2.23). Applying a magnetic field or using a ferromagnetic insulator layer [35] can control the Zeeman interaction, which determines the size of the gap and the condition for topological superconductivity and Majorana edge states. However, too high magnetic fields  $B > \mu_0 H_{c2} \cong 65$  mT [9] can destroy the superconducting state of the LAO-STO interface.

A recent theoretical study [37] has shown that topological superconductivity and Majorana edge states can perhaps be realized at the interface of LAO-STO. Apart from the previously mentioned conditions, an additional condition needs to be fulfilled in a bilayer LAO-STO system: the interlayer attraction needs to be both repulsive and stronger than the attractive intralayer interaction.

## Chapter 3

# Principles of Piezoresponse Force Microscopy

A powerful tool for the characterization of ferroelectric thin films is Piezoresponse Force Microscopy (PFM). This tool allows non-destructive imaging of ferroelectric domains at high-resolution. Furthermore, it also enables the manipulation of ferroelectric domains. PFM measurements can be performed with an adapted AFM setup. In this chapter the theoretical concepts behind piezoelectricity as well as the PFM measurement technique will be discussed.

### 3.1 Thermodynamic energy of piezoelectricity

The fundamental connection between piezoelectricity and ferroelectricity can be derived from thermodynamics. In order to understand why the PFM measurement technique can be used for the detection of ferroelectric polarization, some thermodynamics of piezoelectricity has to be discussed. Therefore this section will introduce the basics of the thermodynamics of piezoelectricity. A more elaborate discussion on this topic can be found in references [38, 39], on which the following theoretical discussion is based.

The thermodynamic response of an elastic piezoelectric can be described with the second law of thermodynamics. This fundamental law can be written in such a way that the change in internal energy  $dU$  of an elastic piezoelectric is a function of a change in mechanical strain  $dx$ , a change in dielectric displacement  $dD$  and a change in entropy  $dS$

$$dU = TdS + X_{ij}dx_{ij} + E_idD_i. \quad (3.1)$$

In this equation  $T$  denotes the temperature,  $X$  denotes the mechanical stress and  $E$  denotes the electric field vector. Some of these quantities are in fact tensors of different rank, these tensors are labeled with subscripts  $i, j \in \{1, 2, 3\}$ .

During PFM measurements the temperature can be regarded as constant ( $dT = 0$ ), furthermore, the electric field and mechanical stress are used as independent variables. To get an expression with these independent variables, the Gibbs free energy is used, which can be expressed in differential form using equation (3.1). This results in

$$dG = -x_{ij}dX_{ij} - D_idE_i. \quad (3.2)$$

Two important equations can be expressed in these thermodynamic quantities. These are the equations describing the direct and the converse piezoelectric effect. The direct piezoelectric effect is the effect that a mechanical stress results in a surface charge giving rise to a polarization. The converse piezoelectric effect is just the opposite: a surface charge

giving rise to a polarization results in a mechanical stress. These equations are

$$dD_i = \left( \frac{\partial D_i}{\partial X_{jk}} \right)_E dX_{jk} + \left( \frac{\partial D_i}{\partial E_j} \right)_X dE_j \quad (3.3a)$$

$$dx_{ij} = \left( \frac{\partial x_{ij}}{\partial X_{kl}} \right)_E dX_{kl} + \left( \frac{\partial x_{ij}}{\partial E_k} \right)_X dE_k, \quad (3.3b)$$

respectively, with subscripts  $k, l \in \{1, 2, 3\}$ . The first term in the first of these equations defines the direct piezoelectric effect and the second term in the second of these equations defines the converse piezoelectric effect. Both equations can be written more conveniently in integral form, in which the partial differentials are relabeled to tensors:

$$D_i = d_{ijk}^E X_{jk} + \epsilon_{ij}^X E_j \quad (3.4a)$$

$$x_{ij} = s_{ijkl}^E X_{kl} + d_{kij}^X E_k. \quad (3.4b)$$

In these equations  $s$  is the compliance, the inverse of stiffness,  $\epsilon$  is the permittivity or dielectric constant and  $d$  is the piezoelectric coefficient. The difference between the piezoelectric coefficient for the direct and converse effect is in the order of the subscripts. This means that the piezoelectric coefficient tensor of the converse effect is the transposed tensor of the direct effect.

It is common to simplify the tensor notation in these equations to matrix notation using the Voigt convention [39]. The Voigt convention is in fact a symmetric subscript transformation. The transformation is best explained by an example. Take, for instance, the transformation of the mechanical strain tensor

$$x_{ij} = \begin{pmatrix} x_{11} & x_{12} & x_{13} \\ x_{21} & x_{22} & x_{23} \\ x_{31} & x_{32} & x_{33} \end{pmatrix} \longrightarrow \begin{pmatrix} x_{11} \\ x_{22} \\ x_{33} \\ x_{23} = x_{32} \\ x_{13} = x_{31} \\ x_{12} = x_{21} \end{pmatrix} \equiv \begin{pmatrix} x_1 \\ x_2 \\ x_3 \\ x_4 \\ x_5 \\ x_6 \end{pmatrix} = x_m. \quad (3.5)$$

The rank 2 mechanical strain tensor is thus reduced to a 6-dimensional vector. Analogous transformations reduce the rank 4 compliance tensor  $s_{ijkl}$  to a  $(6 \times 6)$ -matrix  $s_{mn}$  and the rank 3 piezoelectric coefficient tensor  $d_{ijk}$  to a  $(3 \times 6)$ -matrix  $d_{im}$ . Please note the difference between the earlier defined subscripts  $i, j, k$  and  $l$  and the subscripts  $m, n \in \{1, 2, 3, 4, 5, 6\}$ , which have a larger set of numbers. The tensors of rank 1 and 2 do not transform, since these are already 3-dimensional vectors and  $3 \times 3$ -matrices, respectively. In this simplified matrix notation the two equations describing the piezoelectric effect transform to

$$D_i = d_{im}^E X_m + \epsilon_{ij}^X E_j \quad (3.6a)$$

$$x_m = s_{mn}^E X_n + d_{mi}^X E_i. \quad (3.6b)$$

It is now possible to show how the piezoelectric effect is related to the ferroelectric polarization. This can be done by deducing a relation for the piezoelectric coefficient matrix. Comparing equation (3.3a) with equation (3.6a) will make clear that, in the simplified matrix notation, the piezoelectric coefficient matrix can be rewritten to

$$\begin{aligned} d_{im} &= \left( \frac{\partial D_i}{\partial X_m} \right)_E \\ &= \left( \frac{\partial D_i}{\partial E_j} \right) \left( \frac{\partial E_j}{\partial X_m} \right) \\ d_{im} &= \epsilon_{ij} \left( \frac{\partial E_j}{\partial X_m} \right). \end{aligned} \quad (3.7)$$

The second line of manipulation is allowed, because the first differential is defined with constant electric field, so that  $\partial E_i = \partial E_j$  for any  $i$  and  $j$ .

By introducing the elastic Gibbs free energy  $G_e$  the remaining differential in this equation can be eliminated. The elastic Gibbs free energy is in fact the Gibbs free energy with an extra term depending on the electric field and dielectric displacement. The elastic Gibbs free energy is given by

$$G_e = G + E_i D_i, \quad (3.8)$$

in which  $G$  is the integral form of equation (3.2). Differentiating the elastic Gibbs free energy with respect to the dielectric displacement gives an differential expression for the electric field:

$$E_i = \frac{\partial G_e}{\partial D_i}. \quad (3.9)$$

Now equation (3.7) can be expressed as

$$d_{im} = \epsilon_{ij} \left( \frac{\partial}{\partial X_m} \frac{\partial G_e}{\partial D_i} \right) = \epsilon_{ij} \left( \frac{\partial^2 G_e}{\partial X_m \partial D_i} \right). \quad (3.10)$$

The resulting second order differential can be well approximated by using the Taylor expansion of  $G_e(T, X, D)$  around  $G_e^0(T)$ . This can be written compactly as,

$$G_e(T, X, D) = G_e^0(T) + \frac{1}{2}\alpha_1 D^2 + \frac{1}{4}\alpha_2 D^4 + \frac{1}{6}\alpha_3 D^6 + \frac{1}{2}sX^2 + QXD^2 + h.o., \quad (3.11)$$

in which all subscripts are omitted for convenience. The introduced constants are in fact differentials, which are not very interesting for the current problem. Only the constant  $Q$ , which is actually a tensor, is worth mentioning. This constant is the electrostriction coefficient tensor and describes the electrostrictive effect, which is the effect that a dielectric acquires a mechanical strain due to an applied electric field. In this Taylor expansion all terms with odd powers are zero due to the centrosymmetric crystal symmetry in the non-polar or paraelectric phase. Therefore, this thermodynamic relation is formally describing the paraelectric phase only, but it turns out to be a good approximation to the ferroelectric phase too. The approximation given here applies to ferroelectrics with polarization directions along only one of their crystal axis, as is common for many ferroelectrics, including Barium titanate.

Performing the differentiation in equation (3.10) on the Taylor expansion of  $G_e$ , the piezoelectric coefficient matrix becomes a matrix equation:

$$d_{im} = 2\epsilon_{ij} Q_{mjk} D_k. \quad (3.12)$$

Now the polarization can be introduced by using the definition of the dielectric displacement,  $D_k = \epsilon_0 E_k + P_k$ , so that

$$d_{im} = 2\epsilon_0 \epsilon_{ij} Q_{mjk} E_k + 2\epsilon_{ij} Q_{mjk} P_k. \quad (3.13)$$

When there is no electric field applied to the ferroelectric, the expression reduces to

$$d_{im} = 2\epsilon_{ij} Q_{mjk} P_{S,k}, \quad (3.14)$$

in which  $P_S$  is the spontaneous polarization of the ferroelectric. These last equations give the sought after relations between the piezoelectric effect of a material and its polarization. It turns out that the piezoelectric coefficient is proportional to the polarization of the ferroelectric.

### 3.2 Piezoresponse of ferroelectrics

With the PFM technique the piezoresponse of a material is measured. The piezoresponse is in fact the contraction, expansion or shearing of a piezoelectric in an external electric field. It is the result of the converse piezoelectric effect, which changes the size of the unit cell somewhat. Since ferroelectric materials are a subgroup of piezoelectric materials, meaning that all ferroelectrics are piezoelectric, this technique can be used on ferroelectrics too. In the previous section it was shown that the polarization of such a ferroelectric is directly related to the piezoelectric coefficient, which describes the (converse) piezoelectric effect. In this section the piezoresponse of ferroelectric is theoretically discussed based on references [38, 39, 40, 41].

During a PFM measurement no stress is applied to the material and the electric field is applied in the  $z$  direction. In that case  $X = 0$  and  $E = E_z = E_3$ . Under these conditions equation (3.6b) for the converse piezoelectric effect reduces to

$$x_m = d_{m3}E_3. \quad (3.15)$$

For a tetragonal ferroelectric crystal, such as barium titanate, PZT and many other ferroelectrics, the piezoelectric coefficient matrix  $d$  is given by

$$d = \begin{pmatrix} 0 & 0 & 0 & 0 & d_{15} & 0 \\ 0 & 0 & 0 & d_{15} & 0 & 0 \\ d_{31} & d_{31} & d_{33} & 0 & 0 & 0 \end{pmatrix} \quad (3.16)$$

and the permittivity matrix  $\epsilon$  by

$$\epsilon = \begin{pmatrix} \epsilon_{11} & 0 & 0 \\ 0 & \epsilon_{22} & 0 \\ 0 & 0 & \epsilon_{33} \end{pmatrix}. \quad (3.17)$$

From these matrices the only elements that survive in the  $z$  direction are  $d_{33}$  and  $\epsilon_{33}$ . This fixes the subscript  $m$  to  $m = 3$  in equation (3.15) and  $j$  to  $j = 3$  in equation (3.13). Combining both equations results in an expression for the mechanical strain of a ferroelectric during a PFM measurement

$$x_3 = 2\epsilon_0\epsilon_{33}Q_{333}E_3^2 + 2\epsilon_{33}Q_{333}P_3E_3. \quad (3.18)$$

In a PFM measurement the strain is not directly measured as a function of the electric field, but instead the piezoresponse as a function of applied voltage is measured. The compression or expansion of a piezoelectric in the  $z$  direction  $\Delta z$  (out-of-plane) is proportional to the mechanical strain by  $x_3 = \frac{\Delta z}{t_z}$ , with  $t_z$  the thickness of the piezoelectric (ferroelectric) layer. Furthermore, the electric field in the  $z$  direction is given by  $E_z = \frac{V_z}{t_z}$ , with  $V_z$  the applied voltage. During a PFM measurement an AC voltage with a small DC offset is applied, so that  $V_z(t) = V_{DC} + V_0 \cos(\omega t)$ . Using all this, equation (3.18) can be rewritten to

$$\Delta z = 2\epsilon_0 \frac{\epsilon_{33}Q_{333}}{t_z} (V_{DC}^2 + 2V_{DC}V_0 \cos(\omega t) + V_0^2 \cos^2(\omega t)) + 2\epsilon_{33}Q_{333}P_3 (V_{DC} + V_0 \cos(\omega t)). \quad (3.19)$$

This relation can be well approximated by making use of the fact that  $V_{DC} \ll V_0$ ,  $\epsilon_{33} \gg \epsilon_0$  and by comparing the relative size of the other prefactors<sup>1</sup>. This results in

$$\Delta z \approx \pm 2\epsilon_{33}Q_{333} |P_3| V_0 \cos(\omega t). \quad (3.20)$$

From this equation it can be seen that the higher the applied voltage, the higher the piezoresponse and thus the higher the resolution in the PFM scans. This holds up to a critical

<sup>1</sup> $P_3 \sim 10^{-1}$ ,  $t_z \sim 10^{-9}$ - $10^{-6}$  and  $V_0 \sim 10^{-3}$ -1

voltage  $V_c$  at which the sample is destructed, so that for a good PFM measurement  $V_0$  should be as high as possible but  $V_0 < V_c$ .

One step of further manipulation will give the central equation for the PFM measurement technique. This important equation relates the piezoresponse  $\Delta z$  to amplitude  $\Delta z_0$  and phase  $\phi$  as

$$\Delta z \approx \Delta z_0 \cos(\omega t + \phi). \quad (3.21)$$

The phase  $\phi$  is introduced here to account for the sign of the piezoresponse and the amplitude is defined as  $\Delta z_0 = 2\epsilon_{33}Q_{333}|P_3|V_0$ . For a polarization in the  $-z$  direction  $\phi = 0$  and for a polarization in the  $+z$  direction  $\phi = \pi$  (or  $\phi = 180^\circ$ ). The amplitude is however for both polarization directions equal, only at the domain boundary the value decreases rapidly. Combining both amplitude and phase signals will give clear information on the sizes and positions of ferroelectric domains and their polarization direction.

In the above analysis the out-of-plane polarization of a tetragonal ferroelectric crystal is considered. Generally the PFM technique can be used for any piezoelectric crystal with arbitrary polarization direction. The expression in equation (3.21), however, describes only the piezoresponse of out-of-plane polarization, as is shown figures 3.1(a)-(b). For in-plane polarization, polarization in the  $(x, y)$  plane, a similar relation can be derived. In the PFM setup the electric field is always in the  $z$  direction, therefore the unit cells are sheared when they have an in-plane polarization, see figures 3.1(c)-(d). This shearing is described by other matrix elements than just considered. The piezoresponse of sheared unit cells is measured with the PFM as a torsion of the cantilever. Polarizations with both in-plane and out-of-plane components will cause two piezoresponse signals, one due to shearing and one due to expansion or compression of the unit cells, as can be seen in figure 3.1(e).

### 3.3 The PFM technique

The PFM technique can be used for both microscopy and spectroscopy measurements. Microscopy measurements are in fact the measurements usually meant when one speaks about PFM measurements. Strictly speaking, that is what piezoresponse force microscopy is. However, in this thesis PFM is usually used as a spectroscopic tool. The general working principle is the same, although the measurement type is different. To stress the difference, PFM spectroscopy is in literature sometimes also referred to as S-PFM (Spectroscopic PFM) or PFS (Piezoresponse Force Spectroscopy). These measurements are sometimes called ramp measurements.

#### 3.3.1 General working principle

The working principle of PFM is much the same as of AFM. The big difference, however, is that with PFM a voltage is applied to the tip of the probe while a bottom electrode of the sample is grounded (or vice versa). With this configuration an electric field is created through the ferroelectric sample. The applied voltage is AC biased with a frequency commonly within the kHz range. Due to the converse piezoelectric effect, the ferroelectric starts to contract and expand with the applied bias frequency. Ferroelectric domains with a different polarization oscillate with a different phase.

The special PFM tip, which has a conducting coating, follows the movement of the ferroelectric surface. In that respect it is just like AFM, but since the surface height oscillates depending on the polarization, not only the topography of the sample is mapped, but also the ferroelectric domains. To this mapping of ferroelectric domains the polarization of several nanometers below the surface contributes. Therefore a PFM measurement will generally not give information on the extension of domains throughout the thickness of the ferroelectric layer(s).

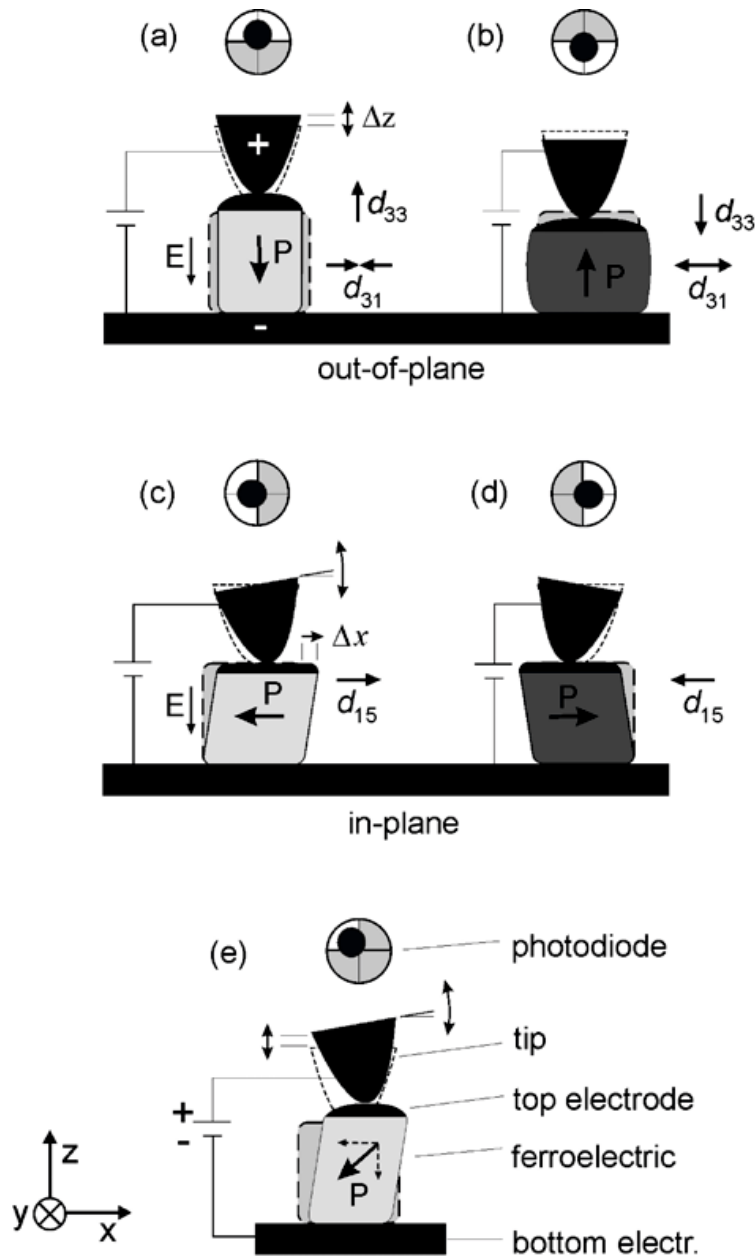


Figure 3.1: Response of different ferroelectric domains on an applied bias voltage when performing a PFM measurement. In (a) and (b) the polarization is out-of-plane which is measured as an up-down movement of the tip due to expansion (polarization parallel to electric field) and contraction (polarization antiparallel to electric field) of the ferroelectric domain. In (c) and (d) the polarization is in-plane which results in a shear movement, measured as a torsional movement of the cantilever. The out-of-plane and in-plane polarizations are measured via two separate lock-ins so that the amplitude and phase in both planes are measured separately, giving four measurement channels. A polarization with components both out-of-plane and in-plane (e) can also be measured, but the phase and amplitude data are each distributed over two measurement channels. Figure from reference [42].

### 3.3.2 Microscopy

The PFM microscopy technique is used to map the polarization and domains of a ferroelectric sample. This mode is denoted as reading. The reading technique must be performed at voltages below the coercive bias. Furthermore, the microscopy technique can be used to polarize a sample into a specific direction. This can be done by applying a bias voltage to the sample which is higher than the sample's coercive bias. This mode is denoted as writing. During a PFM measurement not only the piezoresponse, but also the topography can be recorded.

A general PFM microscopy setup is shown in figure 3.2. The conducting back electrode of the ferroelectric sample and the conducting tip are used to supply an AC voltage with a small DC bias over the ferroelectric. This voltage is applied by a function generator. The signal of the function generator is also used as a reference for the lock-ins of the system. The deflection and torsion of the tip is monitored by a laser beam which is reflected from the tip onto a photo detector. The detector has four quadrants:  $a$ ,  $b$ ,  $c$  and  $d$ . Before starting the measurement the laser spot is aligned in the center of the detector. The laser intensity on the quadrants of the detector  $(a + c) - (b + d)$ , which corresponds to a torsional movement of the tip, is monitored with the first lock-in. The signal on the quadrants  $(a + b) - (c + d)$ , which corresponds to the deflection of the tip, is monitored with the second lock-in. The latter signal is also sent to a low-pass filter, which removes the oscillating piezoresponse, so that a topography image of the sample can be constructed. This signal is then sent to a feedback loop to control the average force on the cantilever. The signal from the first lock-in is used to construct the in-plane amplitude and phase, while the signal from the second lock-in is used to construct the out-of-plane amplitude and phase. The whole set-up, including the data capturing and analysis, is generally computer controlled and combined in a commercial system. [42]

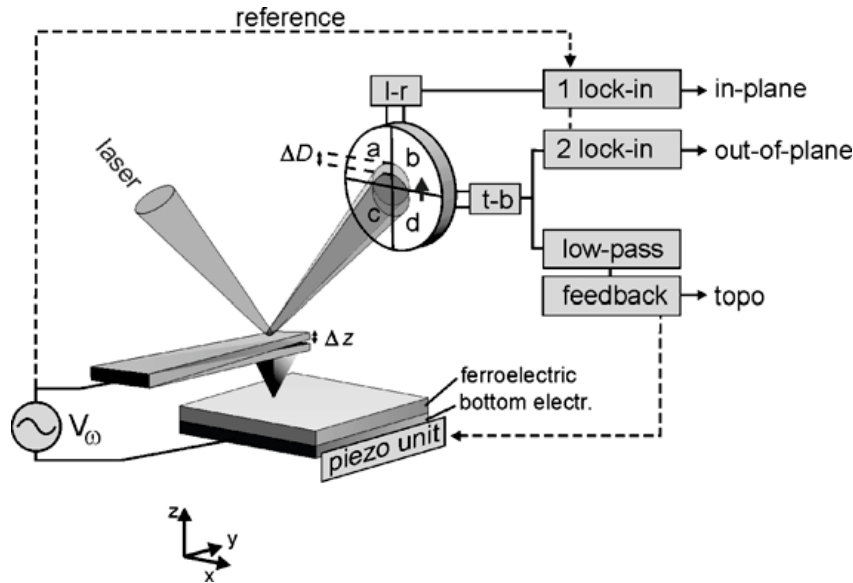


Figure 3.2: The PFM microscopy setup. Figure from reference [42].

The data captured with this technique are scans of the sample's topography and scans of the amplitude and phase of the sample's piezoresponse. The phase and amplitude scans are recorded both in-plane and out-of-plane and can be used to determine the polarization directions in the sample. An example of PFM microscopy data is given in figure 3.3. A

downward polarized domain has a much lower intensity in the phase scan than an upward polarized domain, since downward polarization corresponds ideally to zero phase and upward polarization to  $\pi$  phase. At the edge of a domain the amplitude signal steadily decreases, since the piezoresponse is low at the edge of two different domains, leading to a clear contrast. The amplitude signal thus clearly indicates the edges of the domains, while the phase signal indicates the polarization direction of the domain. Both scans should therefore match. The topography scan should not be fully related to the amplitude and phase scans, although certain surface features (e.g. islands) might act as natural domains.

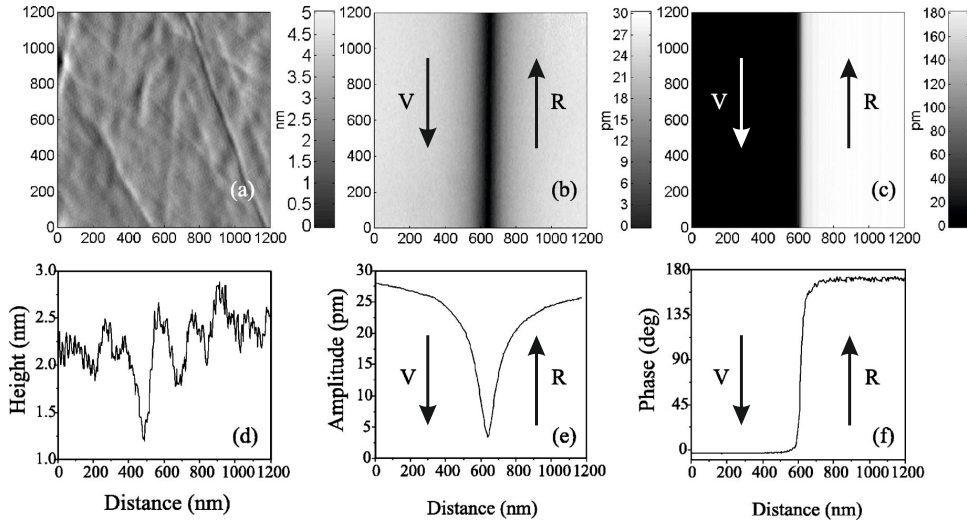


Figure 3.3: An instructive example of experimental PFM data, which are fairly ideal. Figure from reference [43].

### 3.3.3 Spectroscopy

During a spectroscopy measurement the tip is in contact with the surface at a fixed position. At this position the piezoresponse is measured as a function of the DC tip bias, resulting in a local piezoresponse amplitude and phase. The DC tip bias is changed linearly, so that the electric field in the sample changes accordingly. This influences the polarization direction. As soon as the coercive field is reached, the polarization direction switches to another stable polarization direction. At this switching bias a peak appears in the amplitude signal and a  $\pi$  phase change occurs in the phase signal.

For a ferroelectric material, the amplitude signal should consist of a so-called 'butterfly loop'. Two peaks appear at the switching biases. At tip biases lower than the left peak, the ferroelectric is locally switched to an upward polarization. At tip biases higher than the right peak, the ferroelectric is locally switched to a downward polarization. In between the two peaks the polarization direction is switching between the polarization directions, or if not switching, strongly dependent on the sweep direction of the bias voltage. The amplitude signal is useful for determining the local switching biases of the ferroelectric and to reason the polarization direction.

The phase signal will show a hysteresis loop for ferroelectric materials. The hysteresis loop switches from one stable polarization direction to the other, indicated by a hysteretic  $\pi$  phase change. The absolute phase value is, however, not a direct measure for the polarization direction, as might be suggested from equation (3.21). This equation is only valid for PFM microscopy measurements and does not describe these spectroscopic measurements. Although

the absolute phase is arbitrary, the phase change is still  $\pi$ . A clear hysteresis loop is a strong indication of ferroelectricity.

The PFM spectroscopy hysteresis loop is ideally due to the nucleation and switching of a single domain under the influence of a PFM tip at a fixed position. The local domain switching behaviour is thus determining the shape of the hysteresis loop. This has been modeled with the aid of domain wall thermodynamics and kinetics [44, 42]. Considering only thermodynamics and assuming strong indentation<sup>2</sup>, the shape of the hysteresis loop is given by the piezoresponse  $PR$ :

$$PR = d_{eff} \left( 1 - \frac{5\beta\pi^2\sigma_{wall}}{8P_S V_{DC}} \right). \quad (3.22)$$

In this equation  $d_{eff}$  is the effective value of  $d_{33}$ ,  $\sigma_{wall}$  is the domain wall energy in any direction and the proportionality coefficient  $\beta$  is of the order of unity. The piezoresponse  $PR$  defined here is different from  $\Delta z$  and  $\phi$ , since  $\Delta z$  describes the amplitude and  $\phi$  the absolute value of the phase, whereas  $PR$  describes the shape of the hysteresis loop in the phase. The coercive bias, analogous to the coercive field, can be deduced from this model as  $V^+ = V^- = 5\beta\pi^2\sigma_{wall}/8P_S$ . The expression in equation (3.22) does, however, not really give a loop, since it does not give any hysteresis. As soon as domain wall pinning is introduced to the model, the hysteresis loop will appear. Then the domain wall boundary will lag behind its position predicted by the thermodynamic model. When pinning kinetics are considered, the coercive bias is given by  $V^+ = V^- = 2\beta a/k_s$ , where  $a$  is the contact radius and  $k_s$  is the kinetic constant, which is related to the material's pinning strength. The area of the hysteresis loop is a measure for this pinning strength.

The thermodynamic piezoresponse from equation (3.22) is shown in figure 3.4(a). The equation only describes the bold part of the hysteresis curve. The corresponding tip-sample interactions at different parts of the hysteresis loop are given in figure 3.4(c). A domain of opposite polarization is induced by the tip and increases in size, both width and depth, as the bias increases. As soon as the bias decreases again, the domain shrinks in a fully reversible process. This reversibility is due to the absence of pinning, which prevents the system from being hysteretic. Obviously, this is not what happens in ferroelectrics, where the hysteresis is a characteristic property. In practice there is pinning, resulting in a hysteresis loop. When pinning kinetics are considered the hysteresis loop will look like in figure 3.4(b). With pinning the domain wall boundary will lag behind when the bias is decreased, which results in hysteresis. The corresponding tip-surface interactions are shown in figure 3.4(d), where the domain size first increases and then decreases in such a way that the decrease is faster close to the tip than far from the tip.

The PFM spectroscopy set-up is given in figure 3.5. It is largely the same as the PFM microscopy set-up, the main difference is the applied tip signal. In the spectroscopy set-up two function generators are used, whereas in the microscopy set-up only one function generator is used. The first function generator generates the same AC bias with a DC offset as the one in the microscopy set-up. However, the second function generator creates a slow varying triangular signal, which acts as the ramp bias for the spectroscopy measurement. Both signals are superimposed by a summing amplifier and provided to the PFM tip, so that a ramp can be performed with a superimposed signal to generate the oscillating piezoresponse. The resulting output is detected and processed in the same manner as in the microscopy measurement. The final piezoresponse amplitude and phase are now plotted as a function of the delivered ramp bias. No scans are produced since this is a local measurement. [42]

The PFM spectroscopy measurement output will be discussed and analyzed in detail in chapter 5. Examples of PFM spectroscopy data can be found there too.

---

<sup>2</sup>Basically meaning that the tip is in good contact with the surface.

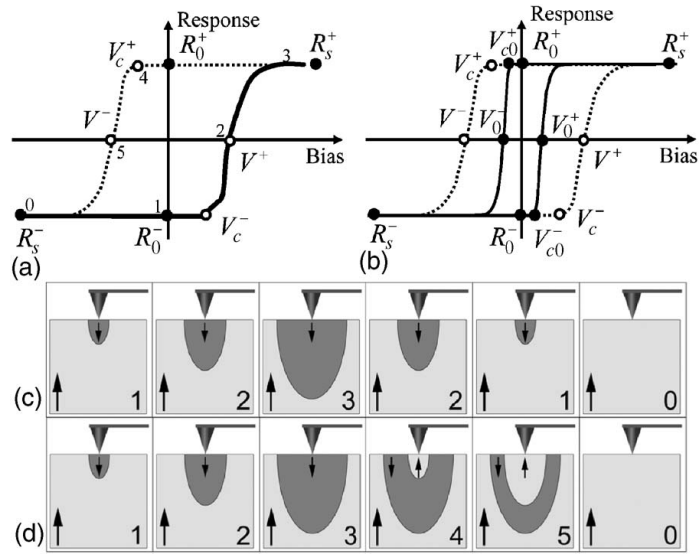


Figure 3.4: Piezoresponse in PFM spectroscopy without (a) and with (b) hysteresis when pinning is not or is accounted for, respectively. The tip surface interaction shows the nucleation of domains when either pinning is not considered (c) or when pinning is in action (d). Figure from reference [44].

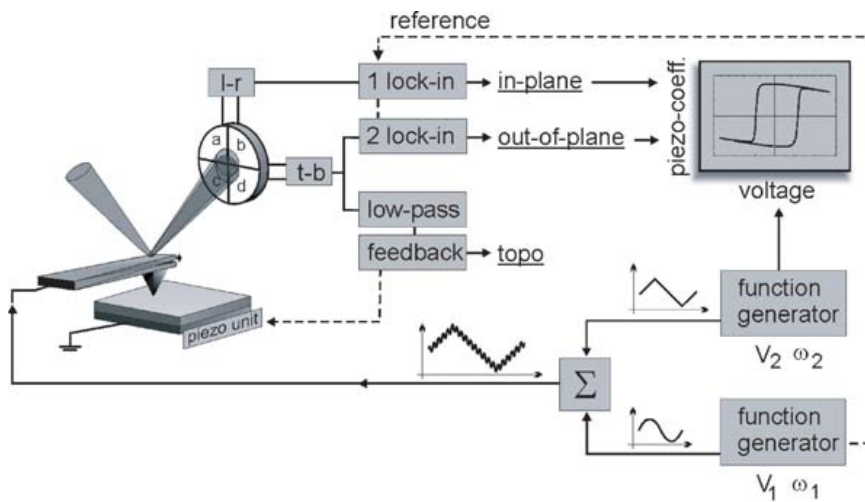


Figure 3.5: The PFM spectroscopy setup. Figure from reference [42].

## Chapter 4

# Manufacturing and characterizing samples

Multiple samples have been manufactured and characterized using various techniques. The conducting interface between LAO and STO is known to be sometimes destroyed by materials deposited on top of LAO-STO<sup>1</sup>. The first tests were therefore designed at verifying the existence of this interface 2DEG when BTO is grown on top of the LAO layer. All oxides were deposited using pulsed laser deposition at specific growth conditions. The growth conditions for ferroelectric thin films of BTO have been established and optimized. The BTO-LAO-STO system was verified to be ferroelectric at certain growth conditions and layer thicknesses. X-ray diffraction has confirmed the materials to be grown epitaxially along the  $c$  axis and to be crystalline. XRD was also used to analyze the effect of water on BTO. Furthermore, samples have been prepared for PFM measurements, for which at least electronic contact to the 2DEG is needed via a special specimen plate. Moreover, devices have been made in the BTO-LAO-STO system using amorphous LAO structuring. All these aspects are discussed in the current chapter.

### 4.1 Substrate treatment and selection

Whether the interface between LAO and STO is conducting or not crucially depends on the termination of the STO substrate [2]. Both LAO and STO can be considered as consisting of alternating planes in the (001) direction, as was discussed in section 1.2. For LAO these planes are  $(\text{LaO})^+$  and  $(\text{AlO}_2)^-$ , while for STO these planes are  $(\text{SrO})^0$  and  $(\text{TiO}_2)^0$ . Only when the interface is bounded by the planes  $(\text{LaO})^+$  and  $(\text{TiO}_2)^0$  a 2DEG is formed. Such an interface is established by using an STO substrate which is single terminated at the  $\text{TiO}_2$  plane. Standard STO substrates are not single terminated, therefore the STO substrate must be chemically treated.

The chemical treatment of STO substrates consists of four steps [45]. The first step is ultrasonic cleaning of the substrates with acetone and ethanol. The second step is to hydrolyze the strontium oxide at the surface of the substrate. This is done in an ultrasonic bath with deionized water for 30 minutes. The  $\text{SrO}$  at the surface will then react with  $\text{H}_2\text{O}$  to form  $\text{Sr}(\text{OH})_2$ . The third step is etching with buffered hydrofluoric acid (BHF) for 30 seconds. In BHF the strontium hydroxide complexes will dissolve, so that the surface will be free of  $\text{SrO}$ . The surface is now single terminated with unit cell terrace steps. The fourth and last step is annealing the substrates at  $950^\circ\text{C}$  for 150 minutes. This will facilitate recrystallization, so that the terraces will be broadened and the edges straightened. Chemically treated substrates with terrace widths ranging from approximately 100 nm tot 500 nm, with on average a width

---

<sup>1</sup>A problem that is not reported, but was experienced in previous research within the ICE and IMS groups.

of approximately 300 nm, have been obtained in this project. A detailed manual on the chemical treatment process of STO substrates can be found in reference [46].

After the chemical treatment the substrates are quality checked and selected based upon AFM scans. A good substrate should have no kinks in the step edges, should have unit cell step height, should have no islands on the terraces, should have no etch pits and should have no dislocations or defects. An example of a good substrate is given in the AFM scan of figure 4.1. Kinks in the step edges and deviations from unit cell step height indicate the presence of SrO, which can be detrimental for uniform 2DEG formation. All other effects mentioned hamper the crystalline growth of LAO thin films. During this project many STO substrates were of poor quality, generally only about 20% of the treated substrates were suitable for LAO deposition.

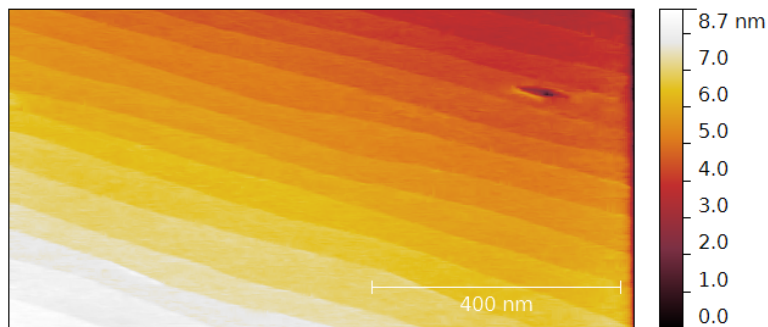


Figure 4.1: A well single terminated STO substrate with straight step edges after chemical treatment. This substrate is nearly perfect, except for a small defect at the upper right corner.

## 4.2 RHEED controlled pulsed laser deposition

All samples have been grown using Pulsed Laser Deposition (PLD). This deposition technique uses a high-power 248 nm pulsed excimer laser to evaporate a target material within a vacuum chamber. The focused laser beam creates a highly directional plasma plume of evaporants that is directed towards a substrate or sample. At the substrate or sample the evaporants, consisting of molecules, ions, electrons and atoms, condense to form a stoichiometric layer of the target material. During the deposition a background gas (oxygen in this research) is introduced in the deposition chamber to maintain the stoichiometry of the deposited material. In this way monolayer by monolayer growth of the target material can be stoichiometrically realized on the substrate or sample. [47]

The used PLD system is equipped with a RHEED gun, so that the layer growth can be monitored utilizing Reflection High-Energy Electron Diffraction (RHEED). In this technique electrons with a high energy, 5-100 keV, are focused on the sample at grazing incidence. The diffracted beam is recorded with a sensor and phosphor screen and consists of a streaked diffraction pattern. The intensity of the diffraction signal is directly related to the film roughness, which is rough when half a monolayer is deposited and smooth when a full monolayer is deposited. This results in intensity oscillations in the diffraction signal during the deposition of a monolayer: before and after the deposition of a full monolayer the RHEED signal is at a maximum, while at half a monolayer the RHEED signal is at a minimum. These RHEED oscillations can therefore be used to monitor the number of monolayers deposited. This technique does, however, only works properly for layer-by-layer growth. [47]

### 4.2.1 Conditions for a conducting LAO-STO interface

In all samples made, 10 unit cells of LAO were directly deposited on the single terminated STO substrate with the growth conditions of table 4.1. This should result in a conducting interface, since the LAO layer thickness is larger than the critical thickness of 4 unit cells. In all samples electronic contact was made to the 2DEG to verify its existence with a simple two-point resistance measurement. This was done on the final samples, with (an) additional top layer(s). In these samples the four-point resistances were found to be within the  $k\Omega$  range. This proves that the LAO-STO 2DEG is conducting after deposition of a BTO top layer with or without gold top contacts.

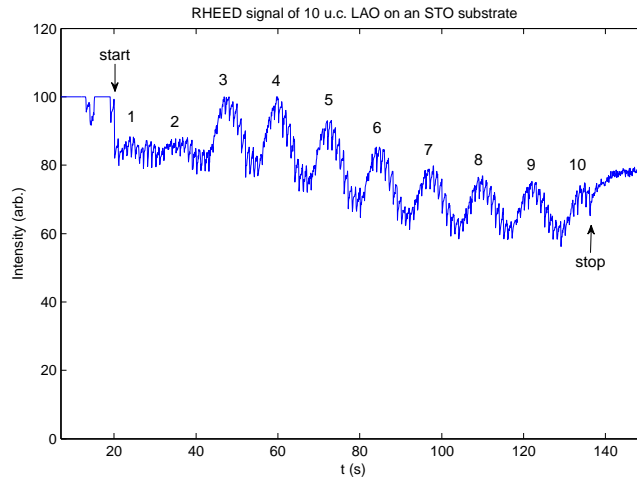


Figure 4.2: RHEED intensity oscillations of the growth of 10 unit cells LAO on an STO substrate, using the growth conditions of table 4.1.

During the PLD process a clear RHEED signal of the LAO growth was observed, as can be seen in figure 4.2. After 10 RHEED oscillations the deposition was stopped manually. The used growth conditions are given in table 4.1. The annealing procedure in this table is initiated after the BTO growth and consists of annealing the sample at the BTO deposition temperature in high oxygen pressure for one hour. After the anneal step the oxygen supply is closed, leaving the system at a residual oxygen pressure, while the sample is cooled down to room temperature at a ramp rate of  $10\text{ }^\circ\text{C}/\text{min}$ .

PLD growth conditions LAO	
laser fluency	$1.4\text{ J}/\text{cm}^2$
spot size	$2.3\text{ mm}^2$
repetition rate	1 Hz
deposition pressure ( $\text{O}_2$ )	$2.1 \cdot 10^{-3}\text{ mbar}$
deposition temperature	$850\text{ }^\circ\text{C}$
annealing time	60 min.
annealing pressure ( $\text{O}_2$ )	500 mbar
annealing temperature	$750\text{ }^\circ\text{C}$

Table 4.1: Used growth conditions for LAO with the same anneal step as is used for BTO.

### 4.2.2 Optimizing growth conditions of ferroelectric BTO on LAO-STO

Unlike LAO, there was no experience with the growth of ferroelectric BTO within the research group. Therefore initially the growth conditions were based upon several growth settings found in literature [16, 48, 49], which were used as a starting point. In the first sample 10 unit cells of BTO were directly grown on an STO substrate to test the initial growth conditions. These growth conditions were partly based upon the literature and partly on the custom growth conditions of LAO. Lower deposition and annealing temperatures (700 °C and 650 °C) and lower energies (25.3 mJ) were used than the optimized growth conditions found later (see table 4.2). The STO substrate used had no outstanding quality and was not fully single terminated after chemical treatment, as was indicated by the kinks in the step edges.

The thin BTO film was found under AFM to have steps with flat plateaus, but had islands at the edges of these steps. This AFM image is given in figure 4.3. The islands at the edge might be due to the fact that the substrate was not fully single terminated ('SrO islands') or due to the growth mechanism of BTO. The latter argument is supported by the fact that during any growth of BTO performed, the RHEED signal was always flattened within a few oscillations.

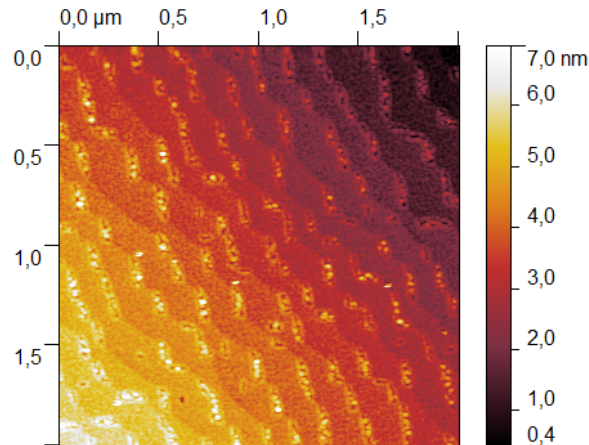


Figure 4.3: AFM image of the first BTO sample, grown with sub-optimal growth conditions.

The same growth conditions and thickness were used for the first sample with 25 nm BTO as a top layer on LAO-STO. In the PFM the BTO layer of this sample turned out to have a too low density, since the tip changed the surface while scanning with a small applied voltage (see also subsection 4.3.2). The growth conditions of BTO were therefore altered based upon the literature and earlier experiences within the research group with barium strontium titanate ( $\text{Ba}_{0.5}\text{Sr}_{0.5}\text{TiO}_3$ ) [50]. These optimized growth conditions are given in table 4.2 and are close to the growth conditions used in reference [16] to grow 1 nm of ferroelectric BTO. In all further experiments discussed in this thesis, these growth conditions have been used. These conditions solved the PFM problem: the density of the BTO layer was sufficient for good measurements.

Still the RHEED signal of the improved BTO growth is poor and indicates layer-by-layer growth only for the first few monolayers deposited. The number of oscillations visible in the RHEED signal is different for every deposition. Sometimes only three oscillations are observed, whereas in other depositions eleven oscillations can be distinguished, as is shown in figure 4.4. In other research similar behaviour is found [51], in which optimization of the growth conditions has led to less than ten oscillations.

According to a publication on the growth stages of BTO on  $\text{TiO}_2$  terminated STO (001) substrates [52], the growth mode of BTO is Stranski-Krastanov, which means layer-then-

PLD growth conditions BTO	
laser fluency	1.8 J/cm <sup>2</sup>
spot size	2.3 mm <sup>2</sup>
repetition rate	1 Hz
deposition pressure (O <sub>2</sub> )	0.13 mbar
deposition temperature	750 °C
annealing time	60 min.
annealing pressure (O <sub>2</sub> )	500 mbar
annealing temperature	750 °C

Table 4.2: Optimized growth conditions for BTO on LAO-STO.

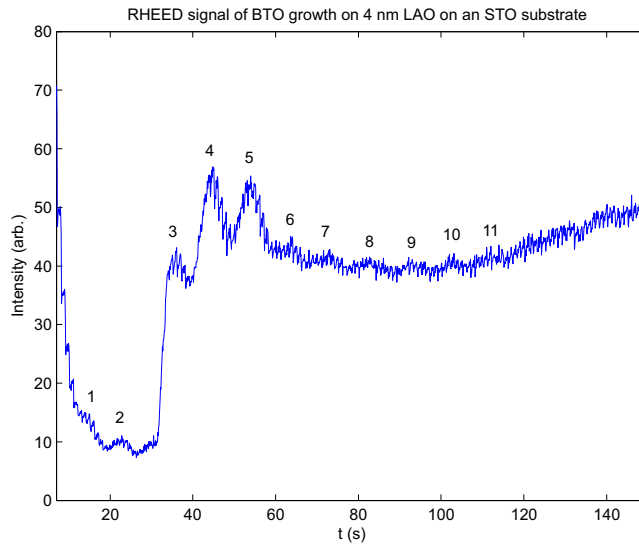


Figure 4.4: RHEED intensity oscillations of the growth of BTO on 4 nm LAO on an STO substrate, grown with the growth conditions of table 4.2. Only the first 150 seconds of the deposition (PLD) are shown, no oscillations were observed in later parts of this deposition. The oscillations are numbered and correspond to the number of monolayers deposited. Between the second and the third oscillation the intensity was increased manually to improve the signal.

island growth. They used PLD and optimized growth conditions for BTO. They furthermore showed that above 5 nm BTO, which approximately corresponds to 12 monolayers, island growth starts and grains are formed. This is consistent with our RHEED observations presented in figure 4.4. At larger thicknesses these grains acquire a lateral size of 100 nm and will continue to grow as columns. These columns also exist in the samples with 100 nm thick BTO films used in this research. This causes the observed surface roughness of approximately 10% and islands, which were observed in the AFM scan given in figure 4.5. These islands have a varying lateral size in the order of 100 nm.

### 4.2.3 Conditions for SRO as back electrode

One sample was made with SrRuO<sub>3</sub> (SRO) as a back electrode in stead of the LAO-STO 2DEG. SRO was chosen as the back electrode material, since it is a conducting perovskite with in-plane lattice constants which are expected to be close to those of STO under the used growth conditions [53]. In this sample 30 nm SRO was grown with a top layer of 50 nm BTO.

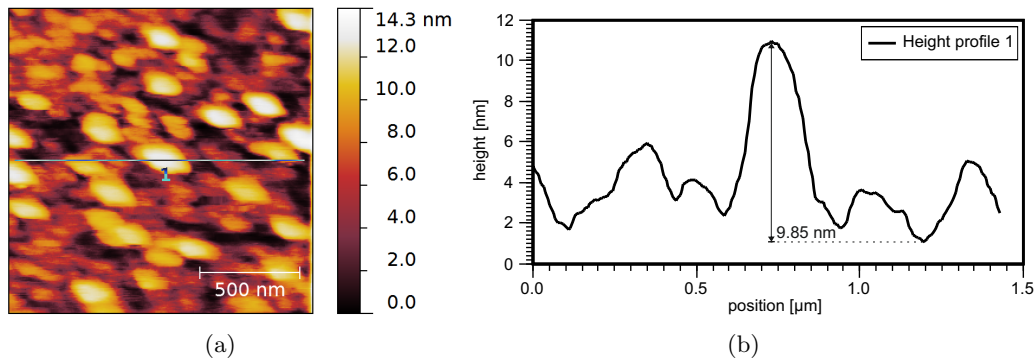


Figure 4.5: AFM scan (a) and height profile (b) of a sample with a top layer of 100 nm BTO and 10 unit cells LAO on an STO substrate. The sample was grown using the optimized growth conditions. From the line scan a surface roughness of approximately 10% can be observed.

The used growth conditions are given in table 4.3 and were based upon literature [53] and the experience within the IMS group with the PLD growth of SRO. Once again, the annealing procedure of BTO is used after the growth of the BTO top layer. During the SRO growth the RHEED intensity decreased after approximately 15 oscillations, so that the observed growth rate of 30 pulses per unit cell was extrapolated to determine when 30 nm SRO was deposited.

PLD growth conditions SRO	
laser fluency	2.0 J/cm <sup>2</sup>
spot size	2.3 mm <sup>2</sup>
repetition rate	1 Hz
deposition pressure (O <sub>2</sub> )	0.13 mbar
deposition temperature	700 °C
annealing time	60 min.
annealing pressure (O <sub>2</sub> )	500 mbar
annealing temperature	750 °C

Table 4.3: Growth conditions for SRO with the same anneal step as for BTO is used.

### 4.3 Characterizing BTO-LAO-STO

The grown BTO-LAO-STO samples were characterized with different techniques. Directly after the growth of the samples the existence of a 2DEG was verified. Later, the electronic properties of the 2DEG were characterized with a low-temperature four-point magnetotransport measurement in the PPMS system to compare these samples to LAO-STO samples without a BTO top layer. The ferroelectricity of BTO was verified with PFM. X-ray diffraction was performed on the samples to check the crystal orientation (growth direction), stoichiometry and crystallinity of the sample.

#### 4.3.1 Electronic properties of the LAO-STO interface

Both with the initial as with the optimized growth conditions of BTO (see table 4.2) the electronic properties of the 2DEG behave qualitatively the same as conventional LAO-STO samples. The many resemblances with these conventional LAO-STO samples convincingly

proof the existence of a similar 2DEG in the BTO-LAO-STO samples. The considered electronic properties of the samples are the sheet resistance, the Hall resistance, the carrier density and the carrier mobility. These properties are measured with the Physical Properties Measurement System (PPMS) during magnetic field sweeps and cool-down.

The magnetoresistance as a function of temperature for a sample with 10 unit cells LAO and 10 nm BTO, which was prepared with optimized BTO growth conditions, is given in figure 4.6(a). The sheet resistance was calculated with the Van der Pauw algorithm [54]. The sheet resistance (symmetrically) increases with magnetic field and decreases with increasing temperature. The anti-symmetrized Hall resistance in figure 4.6(b) is fairly linear as a function of magnetic field, with only slight curvature at low temperatures. Therefore one conduction band can be assumed as an approximation. A one-band model is therefore used to calculate the carrier density. According to this model [55] the sheet carrier density  $n_s$  is calculated by  $n_s = \frac{1}{R_0 e}$ , in which  $R_0$  is the Hall coefficient and  $e$  the electron charge. The Hall coefficient is equal to the slope of the Hall resistance as a function of magnetic field:  $R_0 = \frac{dR_H}{dB}$ . The carrier mobility  $\mu$  is then calculated by  $\mu = \frac{1}{R_s |n_s| e}$ , in which  $R_s$  is the sheet resistance.

The sheet carrier density and the carrier mobility of the BTO top layer samples are compared with data on high-mobility LAO-STO samples<sup>2</sup>. The behaviour of both electronic properties is qualitatively the same, however there are quantitative differences. A striking difference can be seen in the sheet carrier density in figure 4.6(c). At high temperatures the sheet carrier density of the high-mobility LAO-STO sample is an order of magnitude higher than the sheet carrier density of the BTO-LAO sample. In both samples there is a similar thermal activation of the sheet carrier density, both with an onset near 20-25 K. The thermal activation of the BTO-LAO-STO sample is clearly visible in the inset of figure 4.6(c). The number of available charge carriers in the 2DEG of the BTO-LAO-STO is significantly lower at high temperature, but slightly higher at low temperature as compared to a high-mobility LAO-STO sample. This might be due to the used annealing procedure and the BTO top layer. After the BTO growth the system was annealed in high oxygen pressure which influences the oxidation level of the sample, resulting in less oxygen vacancies so that the amount of thermally activated charge carriers was reduced. [11]

The carrier mobility of both samples is indeed qualitatively the same, as can be clearly seen from figure 4.6(d). At low temperature the BTO-LAO-STO sample has carriers with less mobility than the high-mobility LAO-STO sample. The carrier mobility is, however, not unusually low, since LAO-STO samples with nearly the same mobility have been reported [56]. At high temperature the carrier mobility of both samples start to overlap: there is no quantitative difference at these temperatures. The thermal activation is also fairly identical with an onset near 20-25 K. The growth conditions of the BTO top layer might have decreased the carrier mobility at low temperatures.

### 4.3.2 Verification of ferroelectricity

Using PFM the BTO-LAO-STO samples have been tested for ferroelectricity. A sample with a top layer of approximately 25 nm BTO and 10 unit cells LAO on an STO substrate did not reveal any ferroelectricity. This sample was grown with the initial non-optimized growth conditions. Furthermore, upon increasing the bias voltage to pick up a piezoresponse the surface of the sample was modified, as was discussed in section 4.2.2.

A sample with a top layer of 10 nm BTO and 10 unit cells LAO on an STO substrate was grown with the optimized growth conditions (see table 4.2). PFM microscopy scans did not reveal any ferroelectricity in this sample. PFM spectroscopy, however, did reveal a very weak piezoresponse on a few spots. The film was too thin to give a strong piezoresponse,

<sup>2</sup>Data taken from the research of S. Wenderich which is yet unpublished.

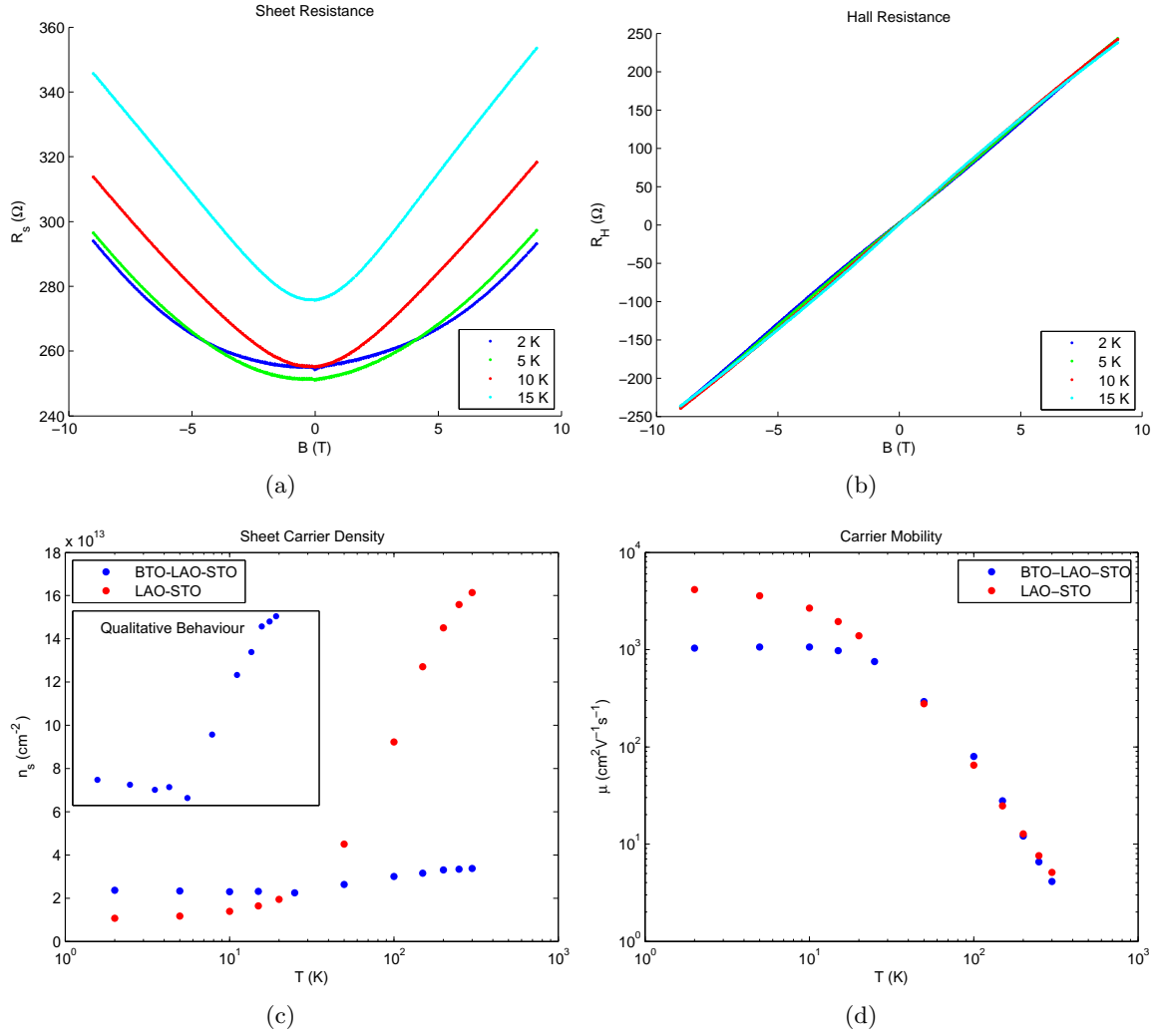


Figure 4.6: Characterization of various electronic properties of the LAO-STO 2DEG in a typical BTO-LAO-STO system. In (a) the sheet resistance and in (b) the Hall resistance are presented at different temperatures. In (c) and (d) the sheet carrier density and the carrier mobility of BTO-LAO-STO are compared with high-mobility LAO-STO samples (see footnote on page 35). The inset in (c) is to elucidate the qualitative behaviour of the BTO-LAO-STO carrier density. The system considered has a top layer of 10 nm BTO and 10 unit cells LAO on an STO substrate.

therefore in all other samples the thickness of the BTO top layer was increased.

Samples with approximately 50 nm BTO on SRO-STO and 100 nm BTO on LAO-STO revealed a clear piezoresponse, indicating ferroelectricity. This was measured locally with PFM spectroscopy, PFM microscopy scans were unable to verify ferroelectricity in these samples. In all further experiments on BTO-LAO-STO 100 nm of BTO was used and PFM spectroscopy was adopted as the main technique to verify ferroelectricity. The analysis of ferroelectricity in BTO-LAO-STO and BTO-SRO-STO samples is discussed in detail in chapter 5.

### 4.3.3 X-ray diffraction

A BTO-LAO-STO sample, grown with optimized growth conditions, was characterized with X-ray diffraction (XRD). The sample examined consisted of a top layer of 100 nm BTO and 10 unit cells LAO on an STO substrate. With XRD the crystallinity of the sample, its stoichiometry and its crystal orientation or growth direction can be verified. An XRD  $2\theta$  scan was made and is presented in figure 4.7.

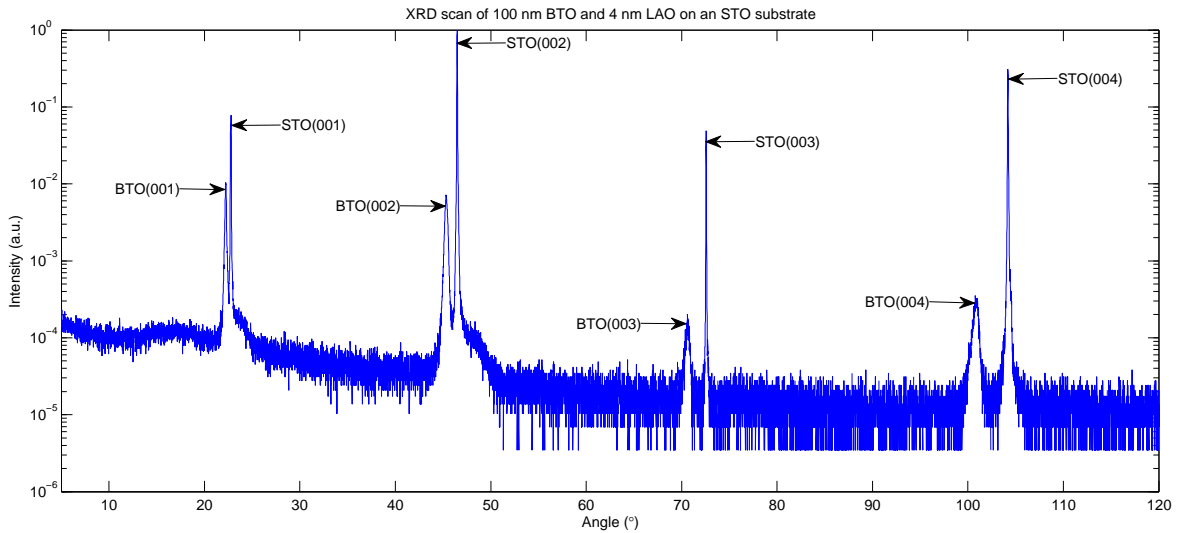


Figure 4.7: XRD  $2\theta$  scan of a sample with 100 nm BTO and 4 nm LAO (10 unit cells) on an STO substrate, for which the optimized growth conditions were used. There are no separate LAO peaks visible, because the LAO layer was too thin to be measured above noise level and was probably fully strained on the STO substrate.

In the XRD scan multiple peaks are visible, these are identified by XRD reference data as BTO(001) and STO(001) peaks. No separate LAO peaks were detected, which was expected, since 10 unit cells is too thin to measure above noise. Furthermore the LAO layers are expected to be fully strained on STO, so that the peaks of LAO and STO would overlap in the XRD spectrum. The STO peaks are larger, because the STO substrate is much thicker than the STO layer, which results in a higher intensity of the refracted beam.

The peaks of all materials are found to be oriented in the (001) direction<sup>3</sup>. The layers are thus epitaxially grown along the  $c$  axis. Furthermore clear peaks appear at the reference positions, indicating a crystalline sample and correct stoichiometry. The optimized growth conditions are therefore, in a crystallographic point of view, good growth conditions.

<sup>3</sup>The identification of the BTO(001) peak is not straightforward. A more detailed discussion on the identification of the BTO(001) peak is given in section 4.6.

## 4.4 PFM sample preparation

To analyze the sample with PFM, the sample must be prepared so that contact can be made to a back gate. The sample needs to have a back electrode below the ferroelectric layer, so that an electric field can be established over this layer. Top electrodes are not necessary, since the conducting PFM tip functions as a local electrode. However, top gates might be used to probe less locally the piezoresonance of the material. To contact the back gate a special PFM specimen plate is needed on which the sample should be mounted. These aspects are discussed in this section.

### 4.4.1 Back gate and specimen plate

For PFM a back gate close to the ferroelectric layer is needed. In the BTO-LAO-STO system no metallic layer can be inserted without blocking the polarization induced electric field over the 2DEG or even destroying the 2DEG itself (see footnote on page 29). Therefore, the 2DEG was used as a back gate. In the PFM experiments discussed in chapter 5, the 2DEG was successfully used as a back gate.

The 2DEG was contacted by sputter deposited gold electrodes at 500 W after 45° argon etching through the BTO-LAO layers. However, it was estimated that the etching was also a few nanometers into the STO substrate. This ensured contact to the 2DEG which is formed in STO at the first few unit cells from the interface [6]. A titanium adhesion layer was sputter deposited first at 150 W to make sure that the gold contacts adhere well to the STO substrate.

For the etching and sputtering a shadow mask was used for most samples. This mask consists of a metallic plate in the shape of a cross, so that at the corners of the sample square gold contacts were deposited. The sample was attached to a microscope slide with silver paste. The shadow mask was carefully placed on top of the sample and with kapton tape fixed to the microscope slide. This allowed the sample to be transferred easily to the etch holder and the sputter holder, without the need to fix the shadow mask twice. Furthermore, the use of a shadow mask had the advantage that no photolithography was needed, so that no chemical reaction between the BTO surface and surface adsorbates could have occurred during the production of these samples.

Contact to a PFM specimen plate was made by wire bonding to the electrodes and gluing the wire to the specimen plate with silver paint. In the PFM setup the specimen plate was grounded so that the 2DEG was effectively grounded too.

### 4.4.2 Top gates

A few samples have been made with top gates to study the effect of gold electrodes on BTO and to apply a more homogeneous electric field to the sample. Furthermore, top electrodes enable to study the piezoresponse of a material less locally [42]. Top electrodes were also used in samples with devices, these are however discussed in more detail in section 4.5.

One BTO-LAO-STO sample was created with top electrodes of different size. This sample contained 100 nm BTO as a top layer and 10 unit cells LAO on an STO substrate. This sample already had electrodes to the 2DEG back gate. The structure for the top electrodes was created with photolithography by using the mask in figure 4.8. Approximately 12 micron thick positive photoresist was spun on the sample at 6000 rpm, followed by annealing the sample at 100 °C for 1 minute. Subsequently, the photoresist was exposed through the mask by UV light for 6 seconds, after which the photoresist was developed in OPD 4262 for 1 minute and rinsed in deionized water for two times 30 seconds.

The contacts were then deposited by low-power RF sputtering. To improve the adhesion of gold to BTO a few nanometers were etched first into the BTO and photoresist. This was

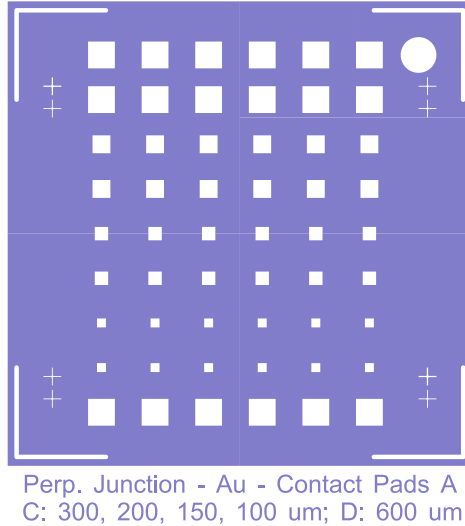


Figure 4.8: Photolithography mask for sputter depositing gold top contacts on BTO-LAO-STO.

followed by a deposition of approximately 100 nm gold at low power (50 W). Low power was needed to limit the implantation and diffusion of gold into the BTO layer, which would probably reduce the ferroelectricity of the BTO layer below the gold contacts. After the gold deposition, a gentle lift-off procedure was performed by dipping the acetone filled beaker, which contained the sample, in an ultrasonic bath. After a few dips the photoresist was completely removed. A gentle lift-off was used to prevent the possible undesired removing of (parts of) the top contacts.

## 4.5 Device fabrication

Devices are needed to measure the expected tuning of the LAO-STO 2DEG by the BTO top layer. Such devices are bridge devices with tunneling contacts, Van der Pauw devices and Hall bar devices. The fabrication of a sample with these devices is more complicated and more time consuming than the previously discussed samples. Two PLD deposition steps, three lithography steps, one etch step and two sputtering steps are needed to complete the sample. The masks are designed with low spatial tolerances and are difficult to align. Combine these facts with the many process steps and it will be clear that the production of the device samples is challenging. In this section the production of these device samples is discussed.

### 4.5.1 Amorphous LAO structuring

A chemically treated,  $\text{TiO}_2$  terminated STO substrate is used for the production of the sample. The substrate is spin coated with 17 micron thick positive photoresist at 6000 rpm and afterwards annealed at 100 °C for 1 minute. Subsequently, the mask in figure 4.9(a) is used to expose the sample to UV light for 6 seconds. Next, the photoresist is developed in OPD 4262 for 1 minute followed by rinsing the sample with deionized water twice for 30 seconds and drying the sample in an argon flow. The sample is now covered with device structures of photoresist.

The uncovered parts of the sample are deposited with amorphous LAO (a-LAO) using PLD. The sample was fixed on the heater with double sided tape, since the normally used silver paint must be heated, which would harden the photoresist. At room temperature approximately 50-100 nm a-LAO was deposited. The exact thickness of the a-LAO layer is

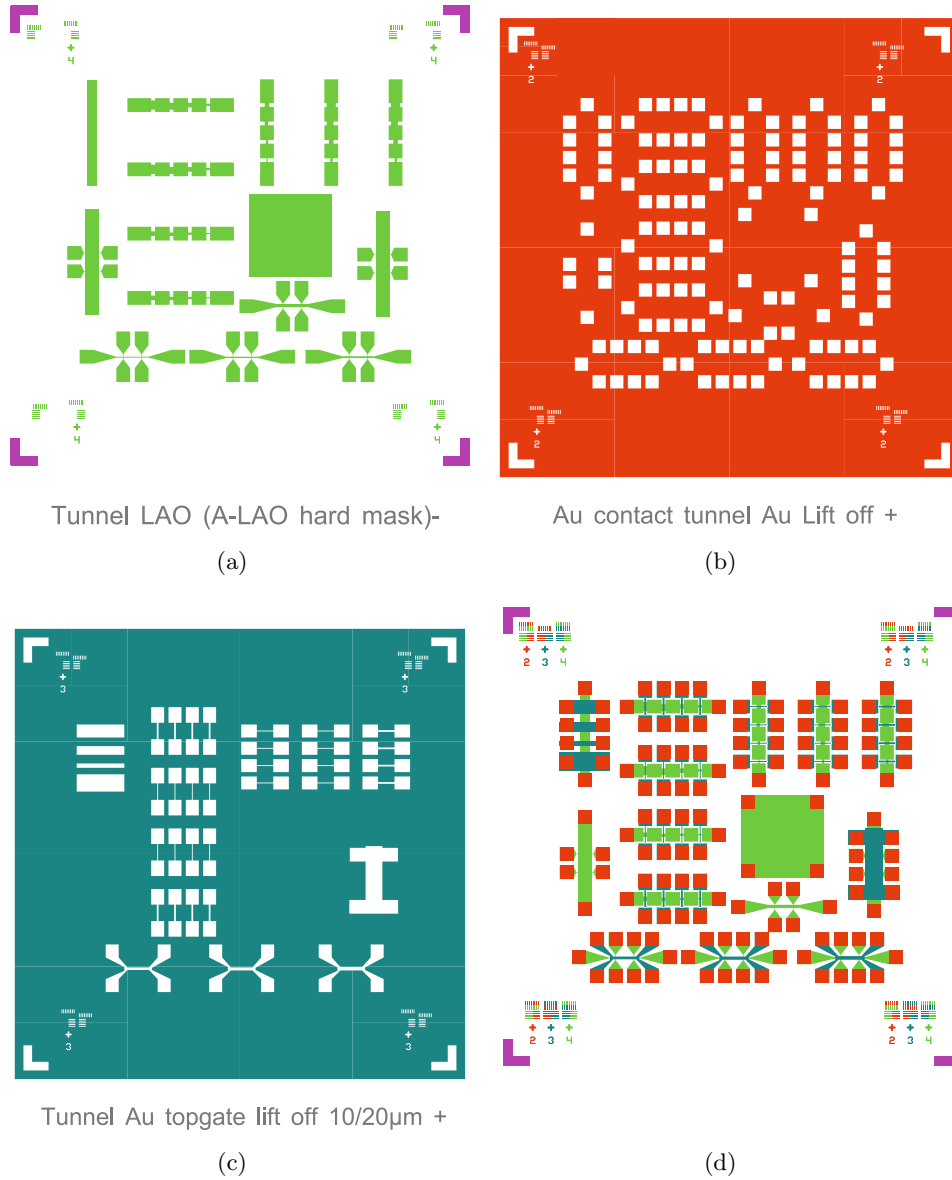


Figure 4.9: The photolithography masks for the fabrication of BTO-LAO-STO devices: (a) is used for the amorphous LAO structuring, (b) is used for the electrode etching and deposition, (c) is used for the depositing of gates and gold electrodes and (d) shows all masks combined to give an impression of the final look of the device sample.

not verified and cannot be deduced from RHEED, since amorphous materials do not grow in a layer-by-layer fashion. The thickness is estimated from the growth rate of crystalline LAO, which will lead to an underestimation due to the lower density of the amorphous layer. The used growth conditions of a-LAO are given in table 4.4.

PLD growth conditions a-LAO	
laser fluency	1.4 J/cm <sup>2</sup>
spot size	2.3 mm <sup>2</sup>
repetition rate	2 Hz
deposition pressure (O <sub>2</sub> )	2.1 · 10 <sup>-3</sup> mbar
deposition temperature	20 – 25 °C

Table 4.4: Growth conditions for amorphous LAO.

After the a-LAO deposition, the photoresist is lift-off ultrasonically in acetone, then dipped in ethanol and dried in an argon flow. The amorphous LAO structure on the sample is used for structuring. The LAO-STO interface only establishes a 2DEG in the device structures that are not covered with a-LAO. The interface between a-LAO and STO is not conducting when the growth conditions of table 4.4 are used [57]. This was also verified in the final sample.

After the lift-off, LAO and BTO were deposited by PLD. The LAO growth was controlled by RHEED and stopped after ten oscillations, which resulted in approximately 4 nm LAO (10 unit cells). After the LAO layer, 100 nm BTO was deposited, which was not monitored with RHEED intensity oscillations. The deposition was ended with an anneal step, as described previously (see tables 4.1 and 4.2).

#### 4.5.2 Back electrode etching and contact deposition

The sample now consists of device structures of BTO-LAO-STO with a 2DEG at the LAO-STO interface, surrounded by amorphous layers of LAO and BTO on an STO substrate. Contacts to the 2DEG can now be made on the devices. A second photolithography step is needed before the gold electrodes can be deposited by RF sputtering. The photolithography procedure is identical to the procedure in the first lithography step, only now the electrode mask in figure 4.9(b) is used.

Once the photoresist is established on the sample, 45° argon etching is used to etch through the BTO-LAO layers into the STO substrate. Subsequently, a thin adhesion layer of titanium was deposited at 500 W by RF sputtering, followed by a gold layer of 100 nm which was sputter deposited at 150 W.

After sputtering the gold contacts, the photoresist was lift-off ultrasonically in acetone. The sample was then dipped in ethanol and dried in an argon flow. Now the sample consists of BTO-LAO-STO devices with back electrodes to the 2DEG.

#### 4.5.3 Gates and top electrodes

The gates and top electrodes were structured in the last photolithography step. The procedure is identical to the previous lithography steps, only now the mask in figure 4.9(c) was used. The top electrodes must be deposited 'softly' to prevent deep implantation of gold atoms in the BTO, which is expected to reduce the ferroelectricity in the sample. Therefore two deposition techniques were used on different samples: electron-beam evaporation and low-power RF sputtering.

One sample was made with electron-beam evaporation in the BAK 600. This deposition technique was directly applied after the photoresist development in the cleanroom. In the

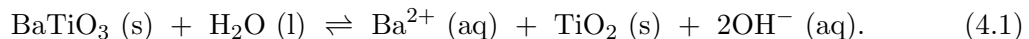
BAK 600 gold is evaporated from a gold target by an electron beam. The evaporated gold softly lands on the sample where it solidifies again. This results in less implantation than with normal RF sputtering. In this way approximately 100 nm gold was deposited.

Top electrodes were successfully made on previous samples with low-power RF sputtering. Therefore, all gates and top electrodes on the other device samples were created by low-power RF sputtering. Before the gold deposition a few nanometers was etched to improve the gold adhesion. Approximately 100 nm gold was deposited at 50 W.

To finish the sample a final and gentle lift-off was performed. The sample was immersed in acetone and the containing beaker was shortly dipped in an ultrasonic bath for a few times. When all the gold is removed, the sample is finished and the sample will be as in figure 4.9(d).

## 4.6 Effect of water on BTO

After the photolithography of the electrodes on the BTO-LAO-STO device samples a color difference was observed which might indicate a chemical reaction between the BTO layer and water. In this production step the sample consisted of polycrystalline and crystalline BTO top layers on amorphous LAO and crystalline LAO, respectively. The color difference after lift-off was observed between the places that were and were not previously covered by photoresist. This color difference was especially pronounced on the polycrystalline parts of the sample: the electrodes seemed to be etched in the polycrystalline BTO layer. This was probably due to a reaction between BTO and water during the development of the photoresist, since according to chemical literature [58], water reacts with BTO via the equilibrium reaction



This would mean that the BaO layers within the BTO unit cell are dissolved in the water while the  $\text{TiO}_2$  layers would remain solid. This severely affects the BTO unit cell and structure of the BTO layer and might therefore be observed as an etching effect. Although this is an equilibrium reaction, the reaction will first react only to the right, since at the first contact with water the equilibrium is not yet reached. During photoresist development the sample is rinsed in deionized water twice in two different beakers for in total one minute. During this process it is highly unlikely that the equilibrium is reached, considering the ration between water and BTO. Therefore, once BTO is affected by the reaction during photolithography, the BaO will dissolve and no  $\text{BaTiO}_3$  will be reformed.

The reaction will only affect the BTO surface layers and the BTO layers near the surface. Since the polycrystalline layers have a rougher surface than the crystalline layers and might be porous, the reaction may affect the polycrystalline BTO layers more. Therefore, the etching effect and color difference is more pronounced on the polycrystalline parts of the sample. The impact of this etching effect on the polycrystalline BTO is studied with AFM. The AFM scan, shown in figure 4.10(a), clearly reveals that the part of the sample that was in contact with water (right) lies deeper than the part that was covered with photoresist (left). The line scan in figure 4.10(b) reveals that the reaction had the effect of etching approximately 10 nm into the polycrystalline BTO layer.

The equilibrium reaction in equation 4.1 is expected to have a strong effect on the PFM measurements on BTO, since this technique is very surface sensitive. If the surface of the film consists of a BaO deficient BTO layer, no clear or even not a single effect of ferroelectricity will be measured, due to a detrimental change in stoichiometry and structure. Furthermore, since only one minute of rinsing in water has led to 10 nm deep etching in polycrystalline BTO, which is approximately 10% of the whole BTO layer, the polycrystalline BTO surface might be considered quite reactive. Therefore it might be well possible that the BTO surface slowly reacts with vapour or water in its environment. For crystalline samples this effect is expected to be less pronounced, since their surface is less rough and denser. However, since

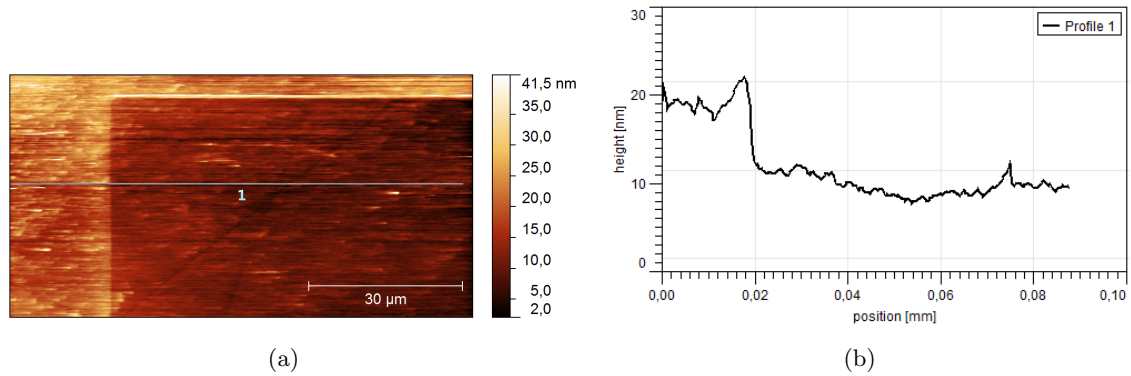


Figure 4.10: An AFM scan (a) and line scan (b) on the edge of a polycrystalline part of the BTO-LAO-STO device sample that was in contact with water (right) and a part that was not in contact with water (left) during photolithography.

their surface still has a roughness of approximately 10% due to the columnar growth of BTO, the reaction will probably still occur, albeit at a lower rate. PFM measurements on samples a few months after their production might thus not be as reliable as PFM measurements performed directly after production. This might partly explain the differences between several PFM measurements on the same samples.

To investigate the effect of water on crystalline BTO a crystalline BTO-STO sample has been made by PLD (growth conditions of table 4.2) and investigated by X-ray diffraction (XRD). A chemically treated STO substrate has been used, so that the substrate was single terminated. This ensured a stacking sequence of the BTO layers so that the BTO surface is  $\text{TiO}_2$ -terminated, which is the same surface termination as when LAO is grown in between BTO and STO. Within 24 hours after deposition the sample was analyzed by XRD. An XRD  $2\theta$  scan was made as a reference for an identical measurement after photolithography. During the lithography process the previously used procedure was performed. The sample was covered with photoresist of which only one half was exposed to UV light. On both sides an XRD  $2\theta$  scan was made to check for differences in structure or composition after contact with water.

The three XRD  $2\theta$  scans made are zoomed in at the second set of film and substrate peaks. Figure 4.11 shows these zooms, which are scaled on the STO substrate peak and combined in one graph for comparison. The peaks are identified using XRD reference data. However, the direction of the BTO film peak is hard to determine, since it strongly depends on the oxygen pressure during deposition. At low oxygen pressure the found BTO peak is corresponding to the (001) direction, while at high pressure this peak is corresponding to the (100) direction. Furthermore, the  $c$  lattice parameter decreases with increasing pressure until a cubic unit cell is obtained, which is no longer ferroelectric [18]. Therefore, XRD reference data sometimes specify the position of the BTO film peak in figure 4.11 to be in the (001) direction, while others specify it to be in the (100) direction. The latter would however mean that cubic BTO has grown along the  $a$  axis on a  $c$  axis oriented substrate. This would result in non-ferroelectric BTO, which was not observed in previous PFM measurements. According to literature [19] it is known that at a pressure of 0.10 mbar, which is used during the BTO deposition, the sample is tetragonal and ferroelectric with a  $c$  lattice parameter of about 0.4 nm. This corresponds approximately to the peak position of BTO in figure 4.11 and the previous XRD scan in figure 4.7, which was calculated to be 0.39947 nm, and is sometimes identified as an (001) peak [59]. Considering these arguments and especially the fact that the polarization was measured out-of-plane with PFM, the BTO film peak is identified as

an (001) peak. The BTO film has thus been grown epitaxially along the  $c$  axis on the STO substrate.

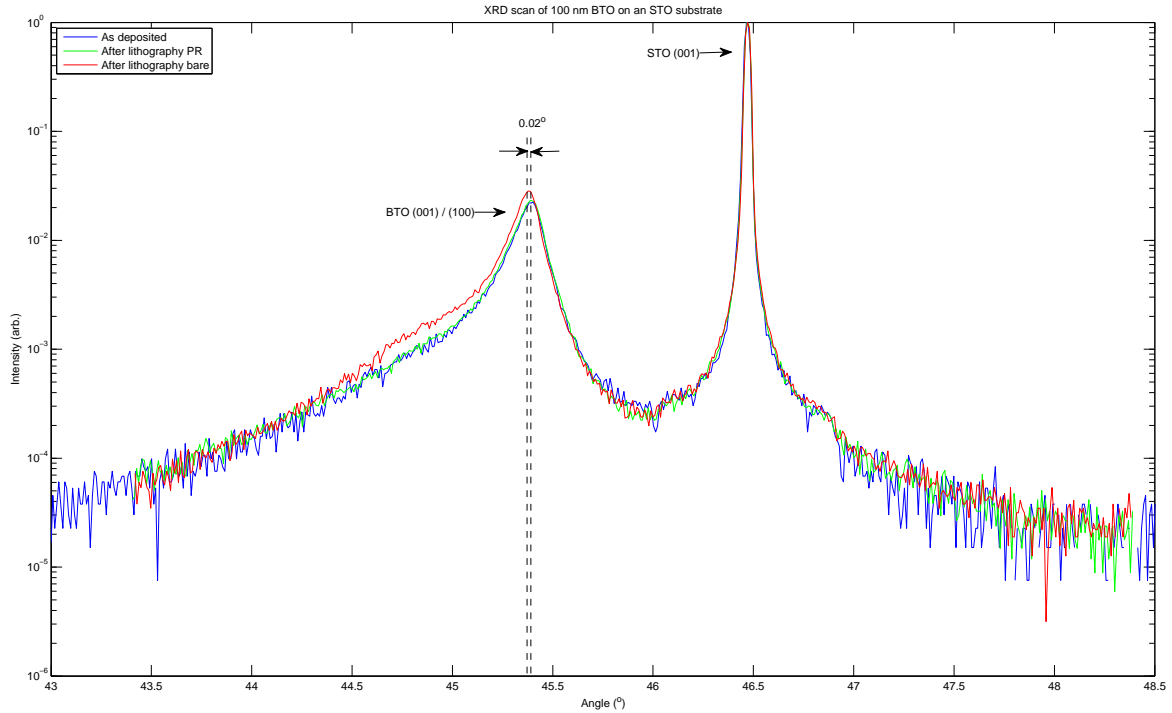


Figure 4.11: Combined XRD  $2\theta$  scans of 100 nm BTO on an STO substrate measured directly after deposition (blue), measured after photolithography on a side that was in contact with water (red) and measured after photolithography on a side that was shielded from water by photoresist (green).

The XRD scan made directly after the deposition (blue) almost perfectly overlaps with the scan made after lift-off on the half covered with photoresist during photolithography (green). This indicates that the part of the sample that was shielded against water has not changed structurally or stoichiometrically. The XRD scan of the half of the sample that has been in contact with water during photolithography (red) is slightly different near the BTO peak. The scan neatly overlaps with the other curves on the STO substrate peak, however in front of the BTO peak a slightly higher shoulder is clearly found. Furthermore, the BTO peak maximum is shifted  $0.02^\circ$  to the left compared to the other curves. This might be due to a change of a few layers near the surface, but the differences in the scans are too small to be significant. This might be due to the fact that only a small amount of BTO layers are affected by the reaction, so that the influence on the XRD signal is minimal. Moreover, the reaction may have made the surface layers somewhat amorphous, in which case the effect will not be visible in an XRD scan.

An AFM scan of this sample would reveal more information on the etching effect of water on the crystalline BTO. However, it turned out that an AFM scan over the border between the water contacted and water shielded side of the sample was impossible. Scanning this border in both contact mode as well as tapping mode, resulted in tip artifacts in the scan. Multiple new tips got contaminated during the scanning and led all to imaging of the tip itself. This was probably caused by a thin line of residual (hardened) photoresist at the border between the two areas. This line was visible with an optical microscope and was first believed to be due to etching. Now, it is more probable that this thin line is (hardened) photoresist in which the tip was dragged and consequently contaminated. This explains the

impossibility to make a sensible artifact-free AFM scan.

In conclusion, polycrystalline BTO layers have clearly suffered from some etching reaction. Crystalline BTO layers might also be affected by a reaction with water, but this could not be confirmed nor excluded by XRD and AFM. The crystalline BTO parts are important for all PFM measurements and the working of devices. An effect of water on the analyzed BTO-LAO-STO samples and devices could therefore not be fully excluded. To do this further research is needed.



## Chapter 5

# Analyzing ferroelectricity and its tuning effect in BTO-LAO-STO

With a ferroelectric layer of barium titanate (BTO) a switchable electric field has been tried to establish, directed towards the 2DEG at the LAO-STO interface. A switchable ferroelectric polarization in BTO is key to establishing this. The resulting electric field can, in principle, be used to tune the electronic properties of the LAO-STO interface and to realize strong Rashba spin-orbit coupling within the 2DEG. Ideally, the ferroelectric polarization can be uniformly switched by applying a short voltage pulse to a top electrode on the system. This voltage pulse must be higher than the switching voltage of the ferroelectric. The ferroelectric properties of the BTO layer are therefore crucial for realizing such a switchable electronic system.

In this chapter the ferroelectricity in the BTO-LAO-STO system is analyzed thoroughly. First, local ferroelectricity is verified by means of PFM spectroscopy. Second, the switching voltages are discussed. Third, a model has been developed to account for the piezoresponse of the system. This model is subsequently tested. Fourth, the homogeneity of the switching is discussed.

Apart from direct measurements of ferroelectricity also gating measurements to find effects of ferroelectric tuning of the 2DEG are discussed.

### 5.1 Ferroelectric hysteresis

The first thing to verify is the occurrence of ferroelectric hysteresis in the grown thin layer of BTO on LAO-STO. As was discussed in chapter 1 and 3, one expects a hysteretic change of polarization upon sweeping the electric field over the BTO top layer. This is successfully verified with the aid of PFM spectroscopy. In these measurements the PFM tip was used to supply an AC signal with a ramped DC offset to create a changing electric field over the BTO layer. The DC offset was ramped linearly from a specified negative voltage to a specified positive voltage and vice versa. The former is called the trace and the latter the retrace.

#### 5.1.1 Piezoresponse

From the piezoresponse of the system three signals were recorded: the out-of-plane amplitude, the out-of-plane phase and the in-plane phase. Together they give crucial information on the plane of polarization, the polarization direction, the switching voltages and the internal biases. All information is however strongly position dependent and can be influenced by surface effects. Still, if the features of ferroelectricity are detected, i.e. a so-called 'butterfly loop' in the amplitude and a hysteresis loop in the phase, these give clear evidence of local ferroelectricity.

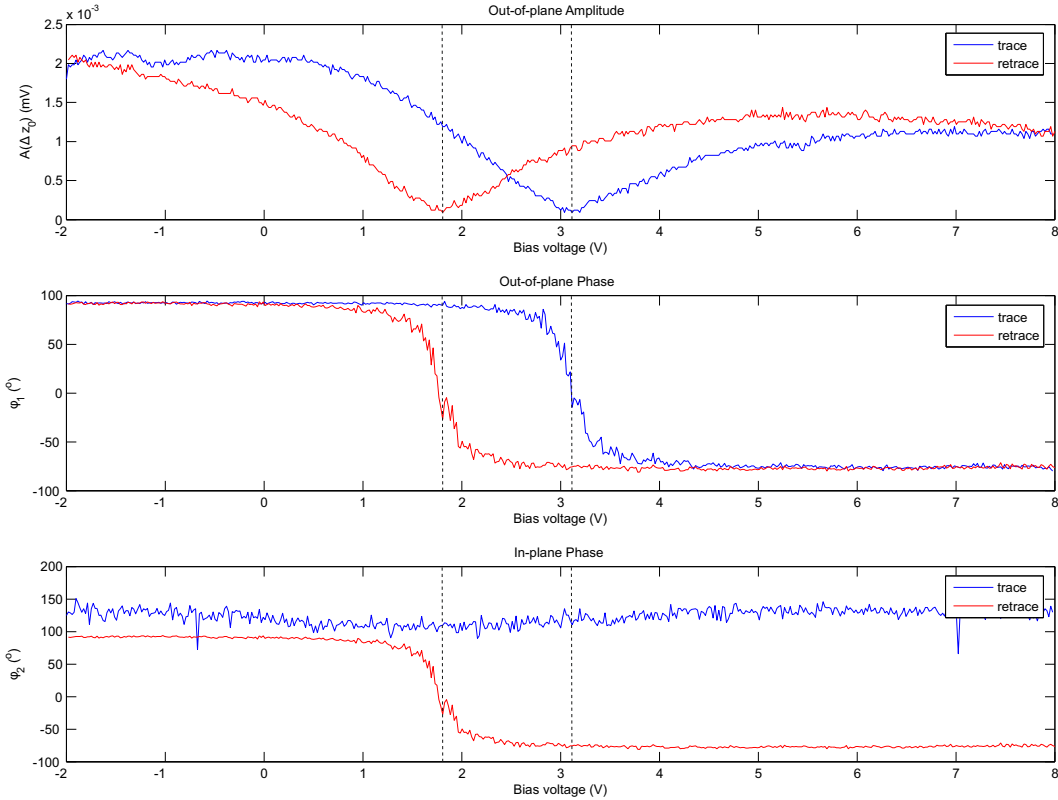


Figure 5.1: PFM spectroscopy data of a sample with 100 nm BTO and 4 nm LAO on an STO substrate showing the characteristic features of local ferroelectricity. The top graph displays the out-of-plane amplitude with a characteristic 'butterfly' loop. The graph in the middle displays the out-of-plane phase with a characteristic hysteresis loop, while the bottom graph displays the in-plane phase without a ferroelectric signal. The bias voltage on the horizontal axis is the ramped DC offset supplied to the PFM tip.

In all examined BTO-LAO-STO samples with approximately 100 nm thick BTO local ferroelectricity was repeatedly observed from PFM spectroscopy measurements. Hysteresis loops were recorded solely in the out-of-plane phase channels and were accompanied by a butterfly loop in the out-of-plane amplitude channels. This indicates an out-of-plane (along the  $c$  crystal axis) polarization of the crystal. The exact appearance of the piezoresponse deviates from sample to sample and from position to position. A typical example of the obtained evidence of local ferroelectricity in BTO-LAO-STO is presented in figure 5.1.

There is no evidence of in-plane polarization (along the  $a$  or  $b$  crystal axes) in the BTO. This is consistent with the expectation for epitaxially grown thin films in the ferroelectric phase, because from the BTO crystal symmetry only out-of-plane polarization is expected, as is discussed in section 1.3.1 of the introduction. Although, the in-plane phase channel generally reveals a jump in the retrace signal that seems to be an exact copy of the out-of-plane retrace signal, it does not indicate any in-plane ferroelectricity, since the trace is generally flat. Considering the complete resemblance between the retrace signals in both phases, the jump in the in-plane retrace signal is believed to be a measurement artifact.

### 5.1.2 Shifted loops

The butterfly loop in the amplitude channel has two minima which correspond to the switching voltages of the ferroelectric. At these voltages the polarization is switched to the opposite direction: upward or downward polarization. In a ferroelectric film one expects these minima

in the butterfly loop to occur simultaneously with the jumps in the hysteresis loop. The jumps in the hysteresis loop of the phase channel thus also correspond with the switching of polarization. The switching voltages are strongly position dependent: in this research no uniform switching voltages were observed across the surface of single samples.

The butterfly and hysteresis loops found on BTO-LAO-STO are generally not centered around zero bias, but are shifted, either to negative or positive voltages. In literature this shift is sometimes referred to as imprint. All these features can be clearly observed in figure 5.1. In this figure the loops are shifted to positive voltages (approximately 2.5 V) and the hysteresis loop has jumps at the peaks of the butterfly loop.

### 5.1.3 Training and loop inversion

In the piezoresponse of the BTO-LAO-STO system training effects have been irregularly observed. At some spots on some samples a training effect of the loop shifting occurred while performing multiple PFM spectroscopy measurements at the same spot. When the ramp was repeated a second time, the shifting of the loops decreased to a lower voltage offset. Ramping more than twice did not decrease the loop shifting any further. An example of such an observed training effect is given in figure 5.2.

The training effect might be ascribed to the changing of the (local) internal biases in the materials system itself. For instance, mobile charges in the system might be displaced to a more stable position in which they compensate the internal bias responsible for the loop's initial shift. The possible sources of these charges are discussed in section 5.2.3. The training effect could, however, also be a result of changing tip-surface interactions, for which the PFM technique is very sensitive. In this view, surface or tip contaminants (e.g. moisture) or surface charge might be displaced after one full ramp and thus influence the piezoresponse.

Another irregularly observed effect is inversion of the hysteresis loop. Both the butterfly and the hysteresis loop are then inverted, which means that the trace signal switches at a lower voltage than the retrace signal, whereas this is expected to be vice versa for a standard hysteresis loop. This behaviour implies that the hysteresis loop reaches at a lower bias the reverse polarization direction than it switches back to its original direction. Inversion of the hysteresis loop is observed in approximately 55% of all measurements and its occurrence seems to be more measurement dependent than sample dependent. For some measurement series the inversion of the hysteresis loop is never observed, while another measurement series on the same sample might in majority reveal inversion of the hysteresis loop. Multiple measurements on the same spot do not change the inversion of the hysteresis loop, the inversion is stable, this would suggest that it is really a local effect too. The inversion of the hysteresis loop is yet unexplained.

## 5.2 Internal biases and polarization direction

The fact that the butterfly and hysteresis loop are shifted from zero bias suggests the presence of local internal electric field biases. A normal ferroelectric, without internal biases, is expected to have switching voltages symmetrically centered around zero bias. A voltage higher than the coercive bias would switch the polarization direction. In the current PFM configuration a positive bias voltage above the coercive bias will induce a downward polarization and vice versa. The BTO-LAO-STO system however has an additional internal bias that needs to be overcome to change the polarization state, therefore the loops are shifted.

### 5.2.1 Band bending model

The measured internal biases can be explained by band bending at the interfaces between the different materials in the samples. The band bending model is displayed in figure 5.3.

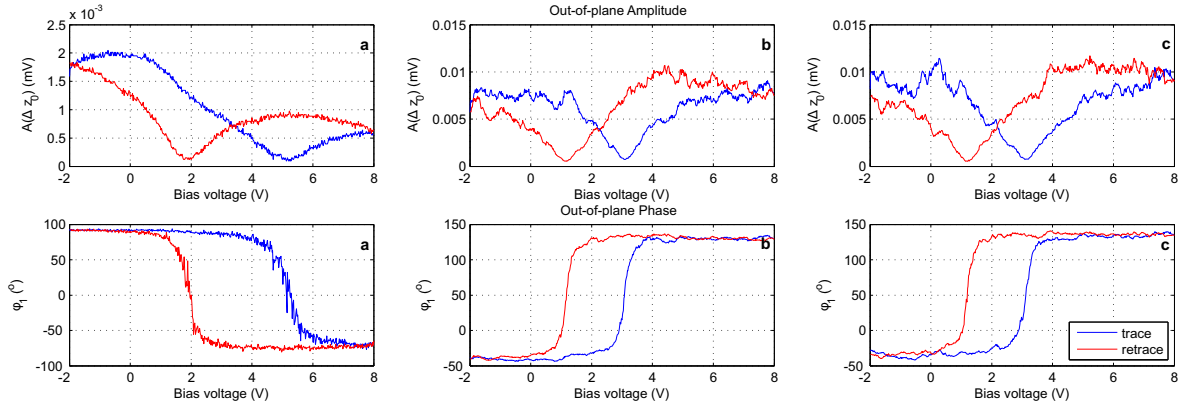


Figure 5.2: An example of observed training of the loop shifting with PFM spectroscopy. During the first measurement (a) switching occurs at approximately 2 V and 5 V bias, whereas during the second measurement (b) switching occurs at approximately 1 V and 3 V bias, which is stable during a third measurement (c). During the second measurement the hysteresis loop in the out-of-plane phase is flipped horizontally, this is different from the discussed inversion of the hysteresis loop, since the retrace still switches at a lower voltage than the trace. This flipping of the hysteresis loop does not change the physics, since the absolute value of the phase does not determine the polarization direction, the phase change is still the same.

Two materials systems are presented, the BTO-LAO-STO system with gold top electrodes in figure 5.3(a) and the BTO-SRO-STO system in figure 5.3(b).

The different materials in the BTO-LAO-STO system with gold top electrodes have different band structures. Gold is a metal and has no band gap but has a filled conduction band. In contrast, the oxide materials in the system are all insulators and do have a wide band gap, but have an empty conduction band. Of all three insulators in this system LAO has the largest band gap, 5.6 eV [7], while BTO and STO have a lower but quite similar band gap, both approximately 3.2 eV [60]. The Fermi levels of LAO and STO are ideally more or less in the center of their band gap, however the Fermi level of BTO is displaced towards its empty conduction band. BTO is thus slightly n-type.

Just as most ferroelectric perovskites, BTO may be regarded as an n-type semiconductor with a low electron mobility. This is mainly a result of oxygen vacancies near the ferroelectric interface. Deposited ferroelectric perovskites are almost always slightly oxygen deficient. This oxygen deficiency manifests itself in local oxygen vacancies which acts as doubly charged electron donors. At room temperature these electrons have a low mobility and are no longer bound to the local vacancies, the ferroelectric perovskite then effectively becomes an n-type semiconductor. This is reflected in the upward displaced Fermi level in the band gap of the ferroelectric perovskite. [38, 61]

As BTO can be regarded as an n-type semiconductor, the interface between gold and BTO forms a metal-semiconductor junction: a Schottky barrier. Such a barrier only appears when the metal work function  $e\phi_m$  is greater than the ferroelectric's electron affinity  $e\chi_f$ :  $\phi_m > \chi_f$ . With this condition being fulfilled the barrier height is ideally given by

$$e\phi_b = e(\phi_m - \chi_f), \quad (5.1)$$

with  $e$  the electron charge to express all quantities in units of energy (eV). BTO has an electron affinity of  $e\chi_{BTO} \approx 3.9$  eV [62], while gold has a work function of  $e\phi_{Au} \approx 5.47$  eV [63]. A contact between gold and BTO will therefore result in a Schottky barrier with a height of  $e\phi_b \approx 1.6$  eV. Since the Fermi levels of both materials are different, the electrons near the

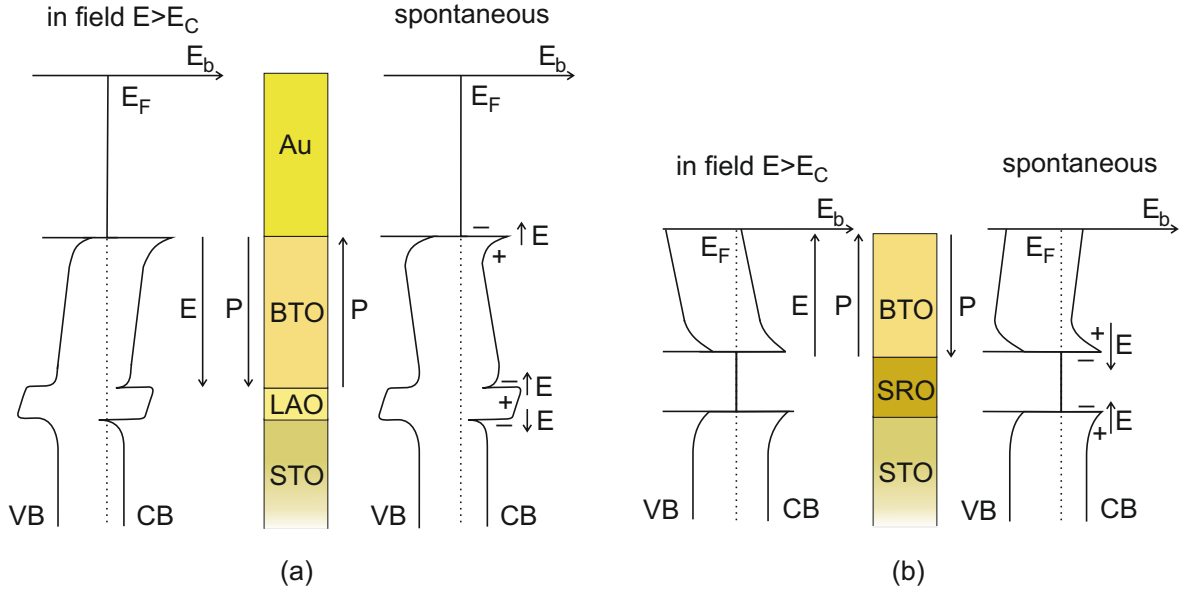


Figure 5.3: Band diagrams showing band bending at the interfaces between the materials of two different samples. The left sample (a) is a BTO-LAO-STO sample with gold electrodes, while in the right sample (b) the LAO layer is replaced by a thicker conducting SRO layer in a sample without gold top electrodes. This results in different band bending and thus in different internal fields ( $E_i$ ) which are expected to change the preferred (spontaneous) polarization direction ( $P$ ). Also the band diagrams corresponding to the opposite polarization direction are displayed, which is reached when an electric field ( $E$ ) above the coercive field ( $E_C$ ) is applied over the ferroelectric BTO layer. In this figure CB denotes conductance band, VB denotes valence band,  $E_F$  denotes fermi level and  $E_b$  denotes band energy.

interface redistribute until both Fermi levels are aligned. This process is accompanied by band bending in the ferroelectric near the metal-semiconductor interface. Electrons from the BTO layer are depleted resulting in a positive space charge layer at the BTO side of the interface. An internal bias is thus established over the interface, giving rise to an electric field towards the gold electrode. [64, 65]

At the bottom of the BTO-LAO-STO system different band bending occurs at the LAO-STO interface. Due to the alternating charged layers in LAO, as was discussed in section 1.2, there is an internal potential in the LAO film which increases with thickness. This linearly increases the energy level of the LAO valence and conduction band until the LAO valence band crosses the energy level of the STO conduction band. Then the electrons are redistributed to the STO conduction band near the interface, which is accompanied by band bending. During this process of charge transfer the internal field of the LAO film decreases until it is zero, which corresponds to the charge transfer of half an electron across the layers. Thus the polar catastrophe is prevented. The discussed process results in similar band bending as at a junction between a metal and a p-type semiconductor. [66]

The band structure of bulk STO and bulk BTO, either in a ferroelectric or paraelectric phase, are very similar [60]. This is especially true near the Fermi level. However, since the BTO film is slightly n-type and the topmost polar LAO layer is charged even after reconstruction, the BTO bands near the interface will slightly bend as its Fermi level aligns with the Fermi level of LAO. This will result in an internal bias and an electric field towards the BTO layer [67].

In the BTO-SRO-STO system both interfaces represent a Schottky barrier, since SRO is metallic with  $e\chi_{STO} = e\chi_{BTO} < e\phi_{SRO} \approx 5.2$  eV [68]. The band bending is thus similar

to the bending between gold and BTO with a slightly lower Schottky barrier  $e\phi_b \approx 1.3$  eV. However, since BTO is slightly n-type the bending of the BTO bands is more pronounced than the bending of the STO bands. The BTO Fermi level needs to be displaced more than the STO Fermi level in order to align the Fermi levels in the system. The electric fields at both interfaces are in opposite direction, both towards the SRO layer.

The direction of the electric fields at the BTO interfaces is expected to pin the ferroelectric polarization at these interfaces and to influence the polarization strongly in the whole thin layer. In fact, the polarization direction in the thin film is determined by these internal biases or fields. Due to the ferroelectric polarization in the BTO layer, which effectively sustains an electrostatic potential over the BTO layer, its bands are slightly tilted. This is in effect the same as the tilting of the LAO bands, however the electrostatic potential over the LAO layer is caused by the alternating polarity of its charged layers. The polarization direction in BTO determines the polarity of the electrostatic potential and thus also the tilt direction of the bands.

From the band bending model it is expected that the ferroelectric polarization will be upward at zero bias in the BTO-LAO-STO materials system, due to the pinning of the polarization by internal biases at the different interfaces. This should be visible as a shifting of the PFM loops, now located at positive bias. The presence of gold or metal top electrodes should not influence the polarization direction in the system, since the electric field due to the Schottky barrier at the electrodes is in the same direction as the electric fields in the bare BTO-LAO-STO system. The PFM loops are therefore expected to be shifted identically.

A system in which the LAO layer is replaced by a metallic SRO layer, however, should flip the polarization direction of BTO downward. Now a Schottky barrier appears below the BTO, which creates a downward electric field at the SRO-BTO interface. In PFM spectroscopy measurements the SRO layer can be used as a back electrode instead of the LAO-STO 2DEG. The PFM loops are now expected to be shifted to negative bias. This materials system can therefore be used to test the discussed band bending model with PFM spectroscopy.

### 5.2.2 Verifying the model

The preferred polarization direction, due to the internal biases in the system, results in shifting of the loops. The locally preferred (spontaneous) polarization direction can therefore be determined from the measured shift of the piezoresponse loops.

At negative tip biases well below the switching voltages, the polarization is surely in an upward direction in the PFM setup. If the phase hysteresis loop is then centered at positive voltages and not switching at zero bias, the system must also prefer an upward spontaneous polarization direction. If the phase hysteresis loop is centered at negative voltages, then the reasoning should be reversed. The local spontaneous polarization then prefers a downward direction. For applied sample biases, instead of tip biases, this analysis should be identically reversed. When the loop is centered at zero bias voltage, the local preferred polarization direction is dependent on the sweep direction, the spontaneous polarization direction can then not be determined from these data. When the piezoresponse loops are centered around zero bias, PFM microscopy maps are needed to determine the polarization direction.

Multiple PFM spectroscopy measurements have been performed on samples with 100 nm BTO and 4 nm LAO on an STO substrate, either with and without gold top contacts, as well as samples with 50 nm BTO and 30 nm SRO on an STO substrate. The results of these measurements are statistically analyzed and presented in table 5.1, in which also the sample type, the sample age at the measurement and the number of measured spots on the sample are listed.

During these measurements different spots on the samples have been measured. Many of these spots directly measured on BTO revealed ferroelectric behaviour, although some were found not to be ferroelectric. On the samples with SRO back gates a large majority of spots

sample type and number	age (mo.)	N	ferroelectric	upward	downward	switching
Au-BTO-LAO-STO 007	<1	4	50%	50%	0%	50%
Au-BTO-LAO-STO 007	1	7	0%	—	—	—
Au-BTO-LAO-STO 007	1	7	57%	100%	0%	0%
Au-BTO-LAO-STO 008	2	7	43%	33%	67%	0%
BTO-LAO-STO 005	2	24	50%	0%	100%	0%
BTO-LAO-STO 005	4	8	75%	67%	0%	33%
BTO-LAO-STO 008	2	23	26%	50%	0%	50%
BTO-LAO-STO 008	2	21	0%	—	—	—
BTO-LAO-STO 009	2	9	44%	0%	25%	75%
BTO-LAO-STO 009	2	20	30%	67%	16%	17%
BTO-SRO-STO 006	<1	11	100%	0%	100%	0%
BTO-SRO-STO 006	1	25	92%	0%	100%	0%
BTO-SRO-STO 006	3	8	75%	0%	100%	0%

Table 5.1: Data of multiple PFM spectroscopy measurements at different spots on samples with 2DEG and SRO back gates either with or without gold top electrodes. The preparation of sample number 005 was discussed in section 4.2.1, that of 006 in section 4.2.3, that of 007 in section 4.4.2 and 008 are the device samples discussed in section 4.5. The age of the sample is the time in months (mo.) between the sample production and the sample measurement and N is the number of spots measured. The polarization state (upward, downward, switching) is expressed as a percentage of the number of ferroelectric spots, as is given by the ferroelectric percentage of N.

was found to be ferroelectric. Ferroelectricity was not or not clearly detected when measuring on gold top contacts. This is explained by the thickness of the gold and BTO layers, which are both 100 nm thick. For BTO this is too thin to give a huge piezoresponse that is not fully or partly damped by the relatively thick gold top contacts. For measurements directly on BTO in samples with a 2DEG back gate the amount of ferroelectric spots differs quite a lot per measurement. Sometimes not even a single spot was found to be ferroelectric during a measurement.

All ferroelectric spots on the BTO-SRO-STO samples were found to be downward polarized. This is in accordance with the presented band bending model. With increasing age the percentage of ferroelectric spots seems to decrease, however the data sets are probably too small to conclude this.

On samples with the LAO-STO 2DEG as a back gate the data are harder to interpret. When measured directly on BTO the polarization direction is sometimes in majority upward, in majority switching or even in majority downward. Furthermore, since samples might be affected by water, as is discussed in section 4.6, measurements on older samples and samples produced with photolithography (007, 008 and 009) are less reliable than the others. Even considering only the most reliable measurements, those on 005, no clear conclusion can be drawn. The most reliable measurements on the gold 007 sample, seems to favour an upward polarization direction. This is however stated with care, since the statistical validity is questionable.

Unfortunately the statistical measurement sets are small, even though much more spectroscopy measurements were performed in each measurement series than listed. However, many of these measurements were on the same spot. These were performed to check training effects, which were not always observed, and to confirm the ferroelectric behaviour. From all multiple measurements at the same spot, only one typical measurement was selected for the statistical analysis. This resulted in the smaller statistical sets. A meta-analysis of different

measurement series on the same sample could have improved the validity of the statistical data, however this is believed to be unjustified due to the possible degradation of the samples by water or moisture, as is discussed in section 4.6. Measurements at later moments can therefore not be fully compared to previous measurements, which is also clear from the large differences between the listed measurement series.

The BTO-LAO-STO samples deviate from the band bending model. The model is therefore either wrong, too simple or a wrong assumption was made. Since the BTO-SRO samples are in accordance with the band bending model and the Au-BTO-LAO samples seem to be, the model is probably not fully wrong. Comparing all three types of samples, a possible explanation was found. In the sample with gold electrodes at both the BTO-LAO and the Au-BTO interfaces the polarization is pinned in the same direction. This pinning at both interfaces is probably so strong that the whole layer, or at least the depth measured with PFM, is polarized in the upward direction. Deviations might be caused by a possible reaction with water. For 100 nm BTO the pinning at the BTO-LAO interface alone is probably not strong enough to polarize also the top part of the layer, which can be measured with PFM. When SRO is used as a back electrode, only a top layer of 50 nm BTO was grown. This might have been thin enough to be fully polarized in the downward direction by the Schottky barrier at the SRO-BTO interface. Furthermore, the electric field at this interface might be stronger than the electric field at the BTO-LAO interface. Another remark is that in the production of the SRO samples no water was used.

The band bending model stated in the previous section, section 5.2.1, is not fully verified. The assumption that 100 nm BTO is fully pinned by the electric field at the BTO-STO interface is probably wrong. Without this assumption, the polarization direction at the top half of the BTO layer in the BTO-LAO-STO samples is unknown. It might be upward, downward or both. Probably charge at the interface, might strongly influence this. Without the assumption discussed, the model is in accordance with the PFM spectroscopy measurements.

### 5.2.3 Extending the band bending model

The observed shift of the PFM loops is sometimes called imprint in literature. The band bending in a materials system is indeed one of the possible explanations for this effect. However, in literature multiple possible explanations have been identified, all give rise to an internal bias. The most important origins of the loop shift identified in literature [69] are (1) trapped charges, (2) charged defects, (3) strain gradients, (4) misfit dislocations, (5) band bending and (6) photo or thermally induced charges. Most of them are introduced during production (1, 2, 3, 4, 5) and some during measuring (6). Apart from the band bending discussed in the previous section, the BTO-LAO-STO system can additionally suffer from some of these other origins of loop shifting. Since the band model is not fully verified, it is very possible that multiple origins account for the observed shift.

The BTO-LAO-STO system might suffer from the combination of trapped charges and charged defects in the form of oxygen vacancies [70]. The used growth conditions for BTO (see table 4.2) employ fairly high oxygen pressure during deposition. This should result in a moderate tetragonality of the BTO unit cell, a moderate spontaneous polarization and a fairly high oxygen content. A doubling of the used oxygen pressure would increase the oxygen content even further, but then the unit cell becomes cubic and the ferroelectricity is lost [19]. Due to the expected fairly high oxygen content, there should be quite a low number of oxygen vacancies available in the BTO. Still, each oxygen vacancy donates two electrons to the BTO layer, which may be delocalized from their vacancy by the polarization induced potential over the ferroelectric BTO layer. This will leave a local positively charged oxygen vacancy. These charges, related to oxygen vacancies throughout the BTO layer, may contribute to the internal bias and shift of the PFM loops. Its relative contribution is hard to estimate, since the actual amount of oxygen vacancies in the used samples is unknown. Further experiments

are needed to retrieve the amount of oxygen vacancies.

Due to the slight misfit of BTO on LAO-STO a compressed strain of 2% is expected in the BTO layer, as was discussed in section 1.3.1. This may be accompanied by some misfit dislocations and strain gradients. The BTO film is initially strained and slowly relaxes with increasing thickness, this will result in a strain gradient and is accompanied by misfit dislocations. Both are a source of internal biases and may thus contribute to the shift of the PFM loops. The amount of dislocations in the used samples and the value of the strain gradient is however unknown. Additional experiments are needed to determine the relative contribution of these effects on the system's observed loop shifting.

Also the polar (charged) LAO layer at the BTO-LAO interface may contribute to the internal potential of the system, as was predicted in reference [67]. The BTO internal bias may thus be influenced by the LAO-STO. However, the research in reference [22], discussed in section 1.4, has led to ferroelectric tuning of the LAO-STO 2DEG with a PZT top layer without a substantial shift of the PFM loops. The difference between the current research and this publication is the use of a different ferroelectric (PZT) and different growth conditions of LAO on STO (lower oxygen pressure). The internal bias may thus be strongly associated with the ferroelectric material or partly with oxygen vacancies in the LAO layer. The effect of the latter may possibly counteract other internal biases in the materials system which are detrimental for the polarization switching in the system.

#### 5.2.4 Consequences of internal bias

The internal bias in the BTO-LAO-STO system, resulting in the shifting of the loops, has important consequences. In fact, it is disadvantageous for the pursued goal of this project. Simple on and off switching of the 2DEG cannot be achieved by applying a short voltage pulse in order to change the polarization. The system is in a preferred polarization direction at zero bias, as soon as the short voltage pulse is over, the system will relax again to this preferred polarization. A constantly applied voltage, higher than the switching voltages of the ferroelectric, is needed to keep the polarization in a state opposite to its preferred polarization. The system can then no longer be used as a passive switch or memory of polarization state.

Another consequence is that PFM microscopy cannot be used to write areas of different polarization direction on the sample, which is generally considered as an important evidence of ferroelectricity. As soon as the tip no longer locally applies a switching voltage, the system will locally relax to its preferred polarization direction. The tip induced polarization direction will thus be lost directly after writing. The writing of areas with different polarization could therefore not be used as a proof of ferroelectricity in the BTO-LAO-STO system. However, on the basis of the obtained PFM spectroscopy data, it is believed that the manufactured BTO-LAO-STO samples are reliably proven to be ferroelectric.

### 5.3 Inhomogeneous ferroelectricity

With PFM spectroscopy the BTO-LAO-STO samples have been analyzed at different spots on the sample to map the global ferroelectric properties of the sample. Since PFM microscopy cannot be used on the BTO-LAO-STO sample, local PFM spectroscopy was needed. The ferroelectricity in the measured samples turned out to be very inhomogeneous. Repeatedly spots were measured that showed no signs of ferroelectricity.

The ferroelectricity was first mapped on a small scale. A few hundred nanometers were scanned in two directions on the 005 sample of table 5.1. The mapping of these scans is shown in figure 5.4(a). The circles indicate the interaction radius of the PFM tip, which is approximately 30 nm. On this small scale only one polarization direction was found: a downward polarization. However, many of the spots measured did not reveal any sign of

ferroelectricity.

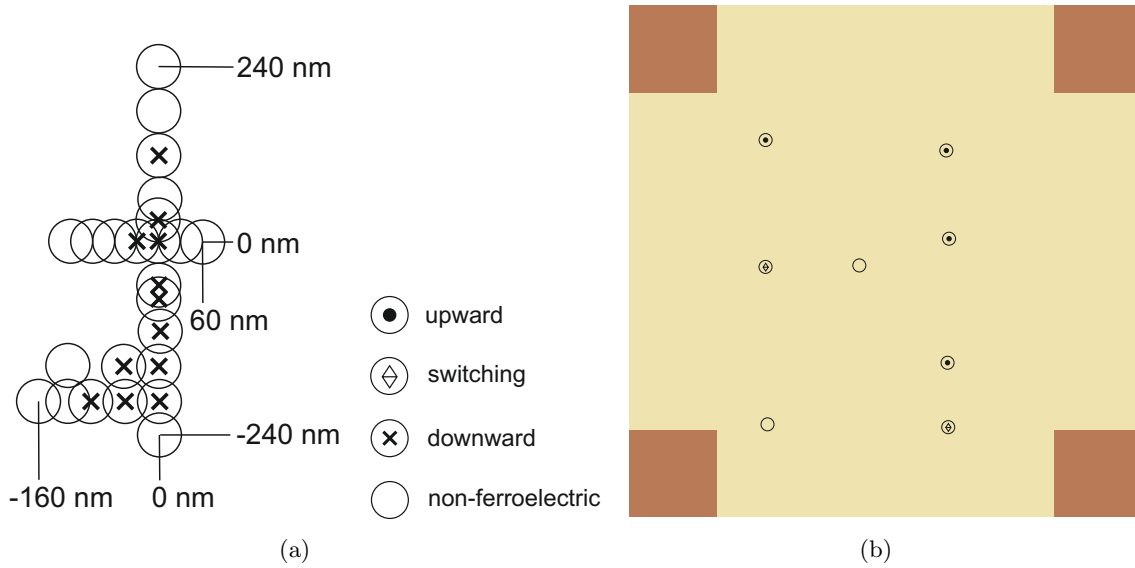


Figure 5.4: Mappings of the ferroelectric state and polarization direction determined by PFM spectroscopy. These figures show the inhomogeneity of ferroelectricity in the BTO-LAO-STO system, both on the small scale (a) as well as on the large sample size ( $10 \times 10$  mm) scale (b). The khaki area is BTO-LAO-STO and the brown squares are contacts to the back gate (2DEG).

The downward polarized spots are neighboring each other on the small scale and might constitute a single domain. In that case, the domain would be approximately 200 nm in length and 100 nm in width. This corresponds to the size of islands observed on the sample surface, as can be seen in figure 4.5, and is at the order of the reported size of the pillars due to the growth mode of BTO [52]. Islands or pillars might therefore act as natural domains in BTO.

On the scale of a full sample the polarization is also found to differ from non-ferroelectric to polarization switching and upward polarized, both measured directly on BTO and gold. The measurement positions on the BTO-LAO-STO sample are shown in figure 5.4(b) and the measurement positions on the Au-BTO-LAO-STO sample in figure 5.5. No clear relation between position and polarization could be found on this scale. Only one observation on the Au-BTO-LAO-STO sample with different sized gold contacts can be mentioned: on smaller sized top contacts, 150  $\mu\text{m}$  and 100  $\mu\text{m}$ , ferroelectricity was measured in contrast to the larger contacts, where no ferroelectricity was measured. However, this does not need to be related to the contact layer size, but can also be due to the inhomogeneity of the ferroelectricity in the BTO-LAO layers. Even so, the number of measurements on these contacts is too low to draw a strong conclusion.

Three different types of devices have been measured for ferroelectricity with PFM spectroscopy. These three types are a Hall bar, a Van der Pauw square and a gate bar and are shown in figure 5.6. The mappings in this figure reveal very little ferroelectricity in these devices. At crucial spots, especially below the bridges of the gate bar, no ferroelectricity was observed. Therefore, there is no hope to detect full ferroelectric depletion of the 2DEG in a gating experiment with this device. The gate bar device is not expected to work. In the Hall bar and the Van der Pauw square the ferroelectricity is so local and so small, that in two- or four-point measurements of the whole device no effect on the 2DEG properties is expected to be found. The commonly observed absence of local ferroelectricity is expected

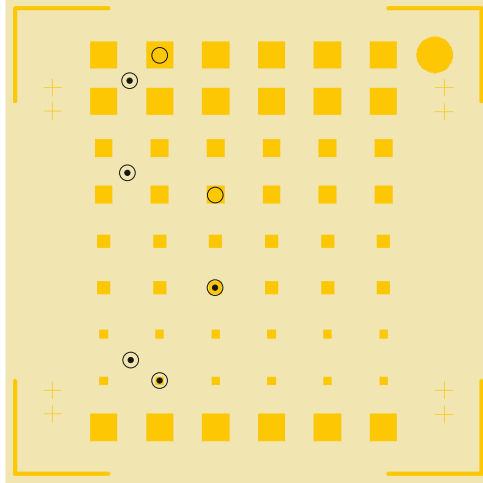


Figure 5.5: Mapping of the ferroelectric state and polarization direction determined by PFM spectroscopy on Au-BTO-LAO-STO. Measurements are both performed on the gold top electrodes (yellow) as well as directly on BTO (khaki).

to be detrimental for the operation of gated Hall bar devices and electronic switches.

## 5.4 Gating BTO-LAO-STO

The polarization of the BTO layer is theoretically expected to influence the conduction of the 2DEG. The electric field due to the polarization is expected to bend the bands near the LAO-STO interface (see figure 5.3). This would induce extra charge carriers or deplete charge carriers from the 2DEG, depending on the band bending and thus on the polarization direction. To see this effect in the conductivity, the polarization must induce a collective and homogeneous change in charge carriers. This can only be possible if large parts of the measured device are ferroelectrically polarized in the same direction.

It was found that ferroelectricity is inhomogeneous in all samples and only locally ferroelectric spots are found, therefore electric field gating below micron-sized bridges is performed. With this small size it might be possible to see the additional effects of ferroelectric gating in the current through the 2DEG. Applying a voltage over these small bridges, which act as top electrodes, the 2DEG can be electrically driven into depletion by an electric field. The bridge is located over a thin confined stroke of BTO-LAO-STO and thus could locally 'turn off' the 2DEG, which would be visible as a zero-current through the 2DEG. The electric bridge gating thus locally decreases the thickness of the 2DEG by band bending until the 2DEG is gone. This is visible as a decreasing, and finally vanishing, 2DEG current. As soon as the electric field between the 2DEG and the top bridge is as large as the coercive field of the BTO, the ferroelectric polarization will start to switch. This switching would be visible in the 2DEG current as an additional upturn or downturn, since it either counteracts or contributes to the electric field gating effect, respectively. The ferroelectric gating is therefore expected to be visible as an additional feature on the electric field gating IV curve near the coercive bias of the ferroelectric layer. If the ferroelectric gating is strong enough, the IV curve would reach quite sudden depletion at this coercive bias, however, this is not expected due to the inhomogeneous ferroelectricity in the device.

The set-up of this gating experiment is shown in figure 5.7(a). The 2DEG (source-drain) voltage is kept at 100 mV while the gate (gate-drain) voltage is swept. Both the gate current and 2DEG current are measured. The gate current is checked first to determine the

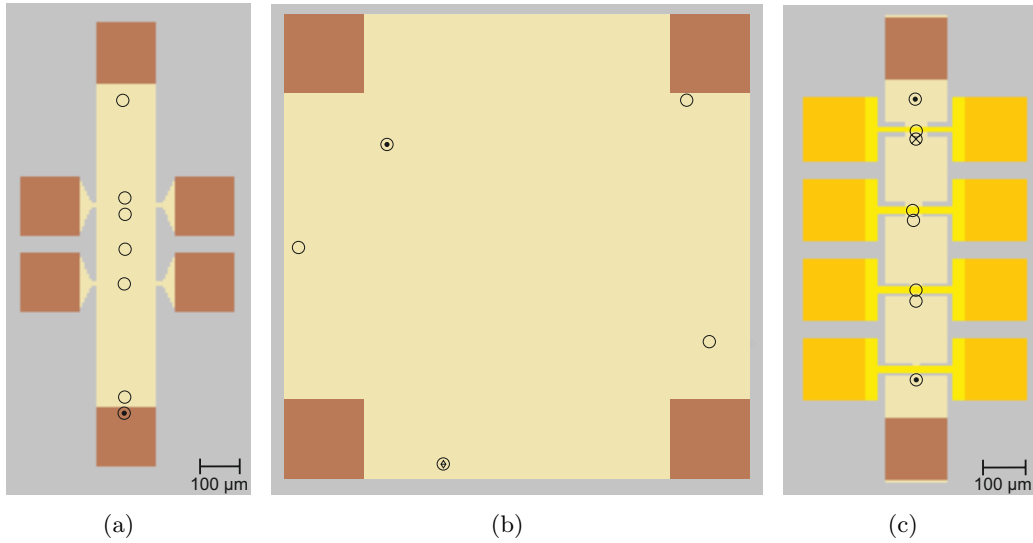


Figure 5.6: Mappings of the ferroelectric state and polarization direction determined by PFM spectroscopy measured on the different devices of the 009 sample. In (a) the Hall bar is depicted, in (b) the Van der Pauw square ( $900 \times 900 \mu\text{m}$ ) is depicted and in (c) the gate bar is depicted. The BTO-LAO layers are coloured khaki, the amorphous layers gray, the bottom electrodes brown and the top electrodes yellow.

breakdown voltage of the BTO-LAO layers. For measuring the 2DEG current, the applied gate voltage should be below the breakdown voltage, otherwise there is a short between the 2DEG and the top gate. The breakdown voltage for the 008 device sample is found to be approximately 2 V. At negative gate biases the 2DEG is slowly driven into depletion which is reached at approximately -5 V with an on-set at approximately -4 V. The IV curve displaying this behaviour is given in figure 5.7(b). The leakage current is not shown, but for negative gate biases the leakage current was within the nA range.

In the IV curve no ferroelectric upturn or downturn is visible, which might be a result of the lack of polarization in the BTO. In the current sample, if ferroelectricity is detected by PFM spectroscopy, the coercive biases always obey  $V_{coercive} > -4$  V. Therefore any effect of the polarization of BTO is expected to be above -4 V. The depletion of the 2DEG by gating at -5 V is thus not reached before ferroelectric effects would have contributed to the process. The observed hysteresis in the IV curve is also unlikely to be related to the switching of the polarization direction in BTO. This is due to the fact that an even more pronounced hysteresis is observed in similar IV curves on LAO-STO samples<sup>1</sup> and the fact that the voltage difference between the curves is at least a factor of four less than the spacing between the coercive biases found in the examined gate bar. The conclusion must then be that in this device the 2DEG was not tuned by ferroelectricity. It still might be slightly tuned very locally, but this does not contribute to the overall behaviour of the 2DEG and cannot be measured.

A second and more elaborate attempt to find indications of ferroelectric tuning of the 2DEG was made. The gate bar on the 009 device sample was used in the same set-up as in figure 5.7(a). Now both the gate voltage and the 2DEG voltage are swept, this allows a 3D mapping of the IV curves. First a leakage test is performed, the results of which are shown in figure 5.8(b). The leakage now already starts at positive gate voltages as low as 0.6 V, but this onset (gate) voltage increases for higher 2DEG voltages until there is no leakage anymore. This makes sense, since it is the potential difference over the BTO-LAO layers that

<sup>1</sup>An observation that is not reported, but was experienced in other research within the ICE group.

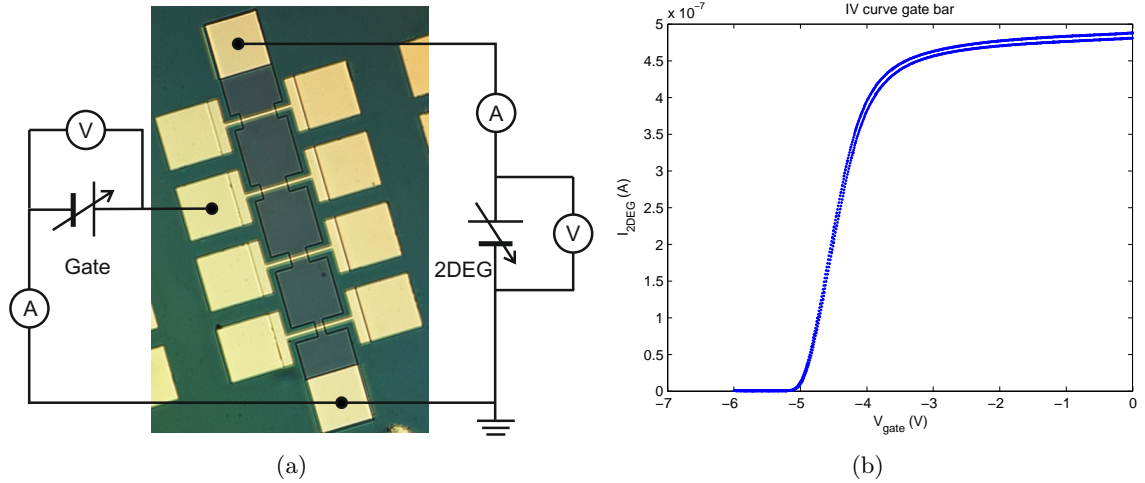


Figure 5.7: The probe station measurement set-up for the gating measurements on a gate bar (a) and the resulting IV curve measured on the 008 device sample with a 2DEG bias of 100 mV (b).

determines the leakage, therefore there is an interplay between the gate and 2DEG voltages. Still, at negative gate voltages there is never any leakage.

The measured IV curves show depletion of the 2DEG only for certain combinations of 2DEG and gate voltages, as can be seen in figure 5.8(a). Depletion starts now already at approximately -2 V gate bias, while the coercive bias in this sample always obeys  $V_{coercive} > -3$  V. Therefore, there might be some effects of tuning invisible in the depletion range. Still, spots were found with PFM spectroscopy with higher coercive biases, and these effects are neither visible in the IV curve. The overall behaviour of the 2DEG is thus not influenced by the ferroelectric polarization in the BTO layer.

There are, however, some remarkable features in these IV curves. The 2DEG is not depleted for all 2DEG voltages above approximately -2 V gate bias. At 2DEG voltages below approximately -7 V the 2DEG allows some conductivity. In this range was, however, no significant leakage current observed, as can be seen in figure 5.8(b). At these voltages the depleted 2DEG transforms into a state in which the 2DEG is able to sustain negative currents. This behaviour is somewhat analogous to a Schottky barrier (diode) in reverse bias, which has quite similar IV curves. If there is a Schottky barrier, then this could indicate a bad contact between the gold electrodes and the 2DEG. This is a very possible explanation, since the production of this sample has been challenging. Furthermore, in later PPMS measurements, where the sample is cooled down to 4 K, the wire bonds came off the back electrodes. This indicates a low-quality contact indeed.

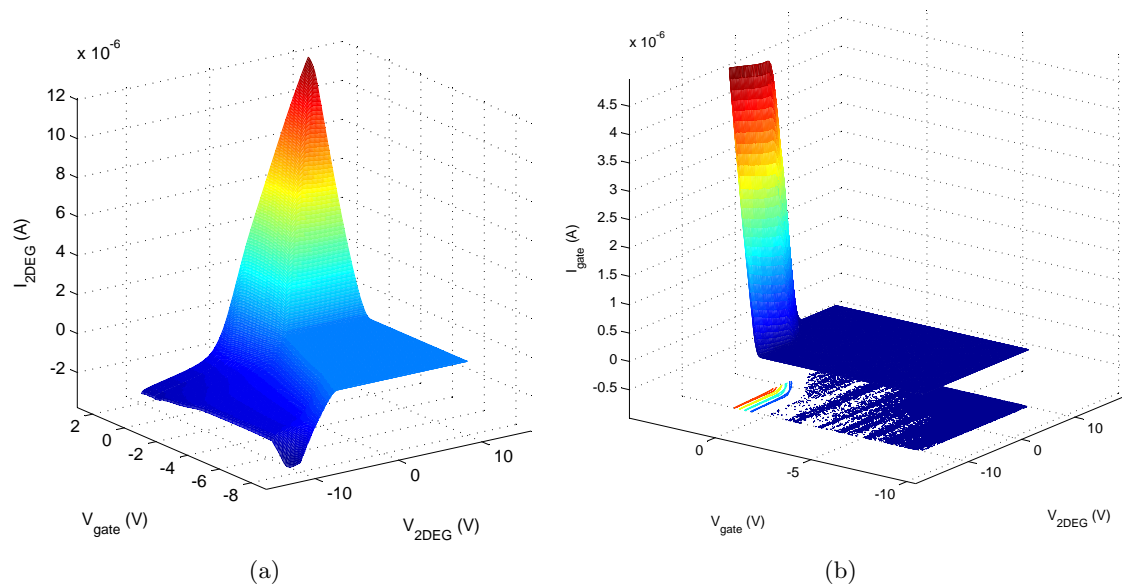


Figure 5.8: Three-dimensional IV curves displaying the gating measurement (a) as well as the corresponding leakage current measurement (b) on the gate bar of the 009 device sample.

## Chapter 6

# Conclusions and recommendations

In the research described in this master thesis the effect of a ferroelectric BaTiO<sub>3</sub> top layer on the 2DEG of LaAlO<sub>3</sub>/SrTiO<sub>3</sub> heterostructures has been studied. The electronic effects of ferroelectric tuning of this 2DEG have been explored, but were not clearly observed. In the current research some necessary experimental foundations have been investigated to near the ambitious final goal of realizing strong spin-orbit coupling in the LaAlO<sub>3</sub>/SrTiO<sub>3</sub> 2DEG for the research on Majorana fermions. The main conclusions of this research are discussed here and recommendations are presented to reach this final goal.

### 6.1 Conclusions

In this project BaTiO<sub>3</sub> (BTO) was chosen as a top layer to ferroelectrically tune the interface 2DEG between LaAlO<sub>3</sub> (LAO) and SrTiO<sub>3</sub> (STO). The choice for BTO was based on its perovskite structure with lattice constants closely matching to those of LAO and STO and the reported fact that BTO can be grown ferroelectrically in very thin films down to 1 nm [16]. BTO was grown with pulsed laser deposition (PLD) assisted by reflection high-energy electron diffraction (RHEED). The PLD growth conditions of BTO have been optimized for a good layer density, not for improved ferroelectricity. These optimized BTO films were deposited at a deposition temperature of 750 °C in 0.13 mbar oxygen pressure with a fluency of 1.8 J at 1 Hz repetition rate, followed by a 60 minutes anneal step at deposition temperature in an oxygen pressure of 500 mbar. The RHEED signal of the optimized BTO deposition indicated layer-by-layer growth only for the first eleven monolayers or less. The surface of BTO was found with atomic force microscopy (AFM) to be covered with islands with a varying lateral size in the order 100 nm. The surface roughness of the BTO top layer was found with AFM to be approximately 10% of its layer thickness. These findings are in accordance with literature [52] where a Stranski-Krastanov growth mode for BTO is reported, which results in columnar islands with a lateral size of approximately 100 nm. X-ray diffraction (XRD) has revealed good stoichiometry, crystallinity and epitaxial growth along the *c* axis of the BTO thin films on the LAO-STO materials system.

The BTO-LAO-STO materials system has successfully been grown with RHEED controlled PLD. The existence of a 2DEG at the LAO-STO interface was verified in this materials system and was thus not destroyed by the ferroelectric top layer. The electronic properties of the 2DEG in the as-deposited BTO-LAO-STO materials system were found to be qualitatively the same as in an LAO-STO heterostructure with an identical LAO layer thickness. This convincingly proved the existence of a similar 2DEG in the current system as in the conventional system. The observed small quantitative differences can be explained by the in situ annealing procedure in high oxygen pressure that was applied to the BTO-LAO-STO samples. It is expected to enhance the oxidation level and therefore reduce the amount of oxygen vacancies and associated thermally activated charge carriers.

Multiple BTO-LAO-STO samples have been manufactured of different types. Apart from BTO-LAO-STO samples, also BTO-SRO-STO and BTO-STO samples have been manufactured all with chemically treated and single-terminated STO substrates. In the BTO-LAO-STO samples the LAO-STO 2DEG was successfully used as a back gate. The device samples were successfully structured with amorphous LAO, which was verified to have an insulating interface with STO.

The ferroelectric properties of the BTO-LAO-STO samples, as well as the BTO-SRO samples, have been thoroughly analyzed with piezoresponse force microscopy (PFM). Only the spectroscopy mode of this technique could be used, which enabled to analyze the local ferroelectricity only within an interaction radius of approximately 30 nm. Only samples grown with the optimized growth conditions for BTO and BTO top layers of more than 50 nm were found to be ferroelectric using PFM. Ferroelectricity in BTO was only found out-of-plane, indicating a polarization along the crystal's  $c$  axis. As expected, no evidence of in-plane polarization was found. The local piezoresponse differed strongly from position to position and from sample to sample.

In the measured piezoresponses multiple effects were found. In approximately 55% of all PFM measurements the hysteresis loop was found to be inverted. This effects seems to be more measurement dependent than sample dependent. The observed inversion of the hysteresis loop is yet unexplained. Another effect, which was irregularly and only occasionally observed, was training of the PFM loops. Performing a second tip bias sweep directly after the first shifted the PFM loops to lower biases, after which their positions remained stable. This can possibly be explained by a changing tip-surface interaction after the first measurement. Another explanation may be that during the first measurement the applied voltage redistributes the available oxygen vacancies to a more stable position, changing the internal bias and structure of the system. The most important effect observed was the shifting of the PFM loops to negative or positive voltages. This was generally observed, although the shift differed per position and per sample. This is in line with the fact that no uniform switching voltages were observed across the surface of single samples.

A model has been developed to account for the shifting of the PFM loops. The shifting indicates internal biases in the materials system, which are ascribed to band bending at the various interfaces in the system. The band bending is accompanied by electric fields which are expected to pin the polarization in the BTO top layer. The internal biases thus determine the polarization direction in the BTO layer.

The band bending model is not fully verified. The model was found to be in agreement with the PFM measurements on the BTO-SRO-STO system and seems to be in agreement with the Au-BTO-LAO-STO system. However, the PFM measurements on the BTO-LAO-STO system are not in accordance with the band bending model. The assumption that 100 nm BTO is fully pinned by the electric field at the BTO-STO interface is probably a wrong assumption in the model. Without this assumption the model seems to work, but is not able to predict a favoured polarization direction in the BTO-LAO-STO system.

The band bending model can be extended by considering possible additional origins of loop shifting. The system may in particular suffer from both trapped charges and charged defects due to oxygen vacancies and both strain gradients and misfit dislocations due to the approximate 2% misfit of BTO on LAO-STO. Also the polar LAO layer at the BTO-LAO interface may contribute to the internal bias in the system. The internal bias may furthermore be strongly related to the ferroelectric material or partly with the number of oxygen vacancies in the LAO layer. Since the band bending model is not fully verified, it is very well possible that multiple origins account for the observed shift. The relative contribution of each is yet unknown.

The shifting of the PFM loops makes the current materials systems unsuitable as a passive switch or memory of polarization state. As soon as a switching voltage over the system

is turned off, the polarization in the BTO layer will relax to its preferred polarization direction. Therefore, it is also impossible to scan the materials systems with PFM microscopy. Furthermore, PFM microscopy cannot be used to write areas of different polarization, which is generally considered as an important evidence of ferroelectricity. Attempts to do so have indeed failed. Still, on the basis of the obtained PFM spectroscopy data, it is believed that the manufactured BTO-LAO-STO samples are reliably proven to be ferroelectric.

The ferroelectricity in all samples was statistically analyzed and found to be very inhomogeneous. In the BTO-LAO-STO system the ferroelectricity was found to be inhomogeneous on both small scale as well as on sample scale. On the small scale only one polarization direction was detected if ferroelectric, these neighbour each other and may constitute a single domain. The BTO islands or pillars may act as natural domains. On the sample scale no relation between position and polarization could be found. Multiple directions were sometimes found on the same sample. Only in the film underneath the smaller gold contacts, 100-150  $\mu\text{m}$ , weak ferroelectricity was found. In the BTO-LAO-STO devices very little ferroelectric spots were found even at crucial positions. These devices are therefore unable to realize full ferroelectric depletion of the 2DEG in gating experiments.

In gating experiments on LAO-STO-BTO no effects of ferroelectric tuning of the interface 2DEG was found. In the IV curves no up- or downturn due to the switching of the ferroelectric polarization was found near the expected coercive biases. The measurement is non-local so that still locally some ferroelectric tuning of the 2DEG might occur, but this cannot be verified. At negative gate biases the 2DEG is slowly driven into depletion, which is reached at -5 V gate bias. A second sample revealed similar behaviour, but here the back electrodes had bad contact to the 2DEG, since diode-like IV curves were observed at a range of negative gate and 2DEG biases.

One possible explanation for the lack of ferroelectricity in the devices is a reaction of BTO with water. This might have occurred during the photolithography steps in the production of the device samples. An etching effect has indeed been observed, which was especially pronounced at the polycrystalline parts of the sample. The reaction is expected to affect the structure, stoichiometry and surface charge of the BTO layer, which are all detrimental for ferroelectricity. Polycrystalline BTO was found to be quite reactive, whereas crystalline BTO is less reactive. A crystalline BTO sample was used to investigate the effect of water on BTO by XRD. The XRD scan of water contacted BTO slightly differed near the BTO peak from the as-deposited BTO XRD scan. This might be due to a change of a few layers near the surface, but the differences between the scans were too small to be significant. AFM scans could help to verify a possible etch reaction with BTO and water in these samples, however the XRD sample turned out to be unsuitable for a sensible artifact-free AFM scan. Thus, there might have been a reaction with the crystalline BTO, but this could not be verified from XRD and AFM scans.

In conclusion, the main goal, realizing and characterizing ferroelectric tuning of the LAO-STO 2DEG, has been partly reached. The characterization of the ferroelectric tuning in these samples was performed, but no clear indications of ferroelectric tuning were found. However, the subgoals defined during the project were reached: (1) a well-chosen ferroelectric layer was successfully grown by pulsed laser deposition, (2) a ferroelectric top layer was deposited on LAO-STO without destroying the 2DEG, (3) the ferroelectric properties of the materials system was extensively analyzed with PFM spectroscopy, (4) devices for electronic measurements on the materials system were successfully manufactured and (5) these devices were used to examine whether there occurs some sort of ferroelectric tuning of the 2DEG. The initial goal of this project, realizing strong spin-orbit coupling induced by a ferroelectric top layer in the LAO-STO 2DEG for the research on Majorana fermions, was theoretically explained but not yet experimentally addressed. Some necessary experimental foundations have however been investigated.

## 6.2 Recommendations

The recommendations posed here are divided in two categories: recommendations on improving the current materials system and measurements and recommendations for further research. With these recommendations the initial and main goal of this research are probably within reach.

### 6.2.1 Improving the materials system and measurements

The developed band bending model turned out to be not fully correct. The polarization in the BTO layer is probably not fully pinned by the internal fields at the interface, but only a part of the layer is. This results in a non-switchable ferroelectric dead layer near the interface. The influence of this dead layer can be reduced by increasing the thickness of the ferroelectric layer. The thicker the ferroelectric film the less the percentage of the film affected by the band bending, so that the polarization of the film will increase. The corresponding electric field towards the 2DEG will equally increase. Furthermore, an increased polarization will improve the PFM signals.

The ferroelectric polarization in the BTO film crucially depends on the oxygen pressure during deposition. Lower oxygen deposition pressures results in higher spontaneous polarizations. Due to oxygen deficiency the tetragonality of the unit cell increases which improves its dipole moment. This oxygen deficiency, however, comes with a decreased dielectric constant due to a larger number of oxygen vacancies. The oxygen deposition pressure used in this research is quite high, resulting in a fairly high dielectric constant, but fairly low spontaneous polarization. This is since the growth conditions were not optimized for ferroelectricity. To improve the ferroelectricity by a factor of 2 and to see corresponding stronger PFM signals, the oxygen deposition pressure should be decreased a factor of 10 [19]. This improved polarization might be successful in tuning the 2DEG, since it increases the electric field towards the 2DEG. A doubling of the polarization is still about a factor of 10 less than the polarization used in the article of reference [22], where effects of ferroelectric 2DEG tuning at the LAO-STO interface have been observed.

The decrease of oxygen deposition pressure during the BTO film growth might thus not improve the ferroelectric polarization enough. Furthermore, decreasing the oxygen pressure will increase the number of oxygen vacancies. This might be a source of stronger internal biases in itself, but might also contribute to the internal bias due to increased band bending, since BTO will behave more as an n-type semiconductor with a large band gap. Therefore, it is probably wise to consider another ferroelectric material as a top-layer on LAO-STO. The research described in reference [22] has proven the successful application of  $\text{Pb}(\text{Zr}_x\text{Ti}_{1-x})\text{O}_3$  (PZT) for ferroelectric switching of the electronic properties of the LAO-STO 2DEG. The ferroelectricity of PZT can be tuned by changing the stoichiometry via the parameter  $x$ , in the referred research  $x = 0.2$  was used. Its piezoresponse on LAO-STO can be mapped by PFM microscopy and the PFM spectroscopy loops seem to be approximately centered around zero bias [71]. This would solve the main experimental problems on BTO experienced in this research.

To prevent a possible reaction between BTO and water it may be wise to grow a thin capping layer on top of BTO. This may be, for example, STO, which is in many respects quite similar to BTO. This has to be a very thin layer, preferably of only a few monolayers, so that the ferroelectricity in BTO can still be probed by PFM.

The effect of surface adsorbates on PFM measurements of the BTO-LAO-STO samples can be better understood if those samples are measured soon after deposition in a controlled environment. This is possible in the Nanolab's COMAT system in which in situ PFM measurements can be performed. This would allow PFM measurements under vacuum conditions, so that water (moisture) and other surface adsorbates are not influencing the sample. If the

PFM loops are still shifted, inverted or show training effects, these effects must be ascribed to internal charges. This would help in understanding and solving these effects in the analyzed materials systems.

The measurements below gold contacts would improve if thinner gold contacts were used and thicker BTO. The latter will reduce the surface and interface effects on the BTO ferroelectricity, while the former would damp the piezoresponse less. Moreover, a different metal for the electrodes may be considered, such as niobium, which has a lower work function, so that the Schottky barrier will be lowered. This would reduce the band bending at the electrode-BTO interface and, consequently, the internal bias at this interface.

### 6.2.2 Further research

The ferroelectric tuning is not clearly realized in the current materials system, but the reported success in reference [22] encourages to look forward to suggestions for further research on the ferroelectric tuning of the LAO-STO 2DEG. The next interesting step would be measuring the strength of the Rashba spin-orbit coupling in this materials system and to show that this coupling is stronger than in the LAO-STO system without a ferroelectric top layer. The coupling strength can be related to the Rashba coefficient, which can be determined from magnetoconductivity measurements in the diffusive regime, as is discussed in reference [36].

Another interesting step would be to change the LAO-STO growth conditions so that the interface 2DEG is superconducting at low temperature. In combination with strong Rashba spin-orbit coupling this would create a materials system which is predicted to exhibit Majorana edge states in small magnetic fields [1, 37]. This would near the initial interest of the current research project and would enable further research possibilities in the quest for the Majorana particle.



# Dankwoord

Met deze master thesis komt een klein jaar van leren en onderzoeken ten einde. Het was een plezierige tijd waarin ik veel geleerd heb. Ik heb veel vrijheid gekregen bij de invulling en uitvoering van mijn opdracht, maar ik zou deze opdracht zeker niet zonder de kennis en hulp van anderen hebben kunnen volbrengen. Daarom wil ik op deze plek een groot aantal mensen bedanken.

Als eerste wil ik Hans en Alexander bedanken voor de interessante en uitdagende opdracht die zij mij toevertrouwen. Alexander wil ik daarnaast bedanken voor de motiverende en enthousiaste wijze waarop hij mij heeft begeleid.

Ik wil Sander in het bijzonder bedanken voor zijn dagelijkse begeleiding. Ik heb veel van hem geleerd. Hij heeft mij veel experimentele vaardigheden bijgebracht en zo veel mogelijk zelf laten uitvoeren. Dat was een leerzame aanpak. Ik vond het prettig dat hij me het project zelf in handen gaf en altijd beschikbaar was voor discussie en advies. Zijn humor en nuchtere kijk op de wetenschap, maakte voor mij de samenwerking erg plezierig.

Op deze plaats wil ik ook Gertjan Koster en Marc Dhallé bedanken voor het feit dat ze zitting wilden nemen in mijn afstudeercommissie.

Naast Sander, heb ik ook veel geleerd van anderen binnen en buiten de vakgroep. Een aantal van hen wil ik hier noemen en bedanken. In het bijzonder Brian, promovendus bij IMS, die mij de PFM techniek heeft bijgebracht en geleerd heeft hoe je PFM data moet interpreteren. Daarnaast Peter en Renshaw voor hun hulp in het lab en hun adviezen op kantoor. Marcel en Denise bij het maken en Sybolt bij het interpreteren van de XRD metingen. Nirupam en Michelle, promovendi bij IMS, voor hun hulp en betrokkenheid. En natuurlijk Frank en Dick voor hun adviezen, uitleg en hulp bij technische problemen.

De mensen in de ICE en QTM vakgroep hebben mijn afstudeerperiode tot een plezierige tijd gemaakt. Mijn kantoorgenoten en medestudenten hebben daar met name aan bijgedragen. Ook hen wil ik bedanken.

Tot slot wil ik mijn familie, vrienden, commissie- en studiegenoten bedanken voor het mede mogelijk maken van een leuke studietijd hier in Twente en omstreken.



# References

- [1] M. Leijnse and K. Flensberg. Introduction to topological superconductivity and Majorana fermions. *Semiconductor Science and Technology*, 27(12):124003, 2012.
- [2] A. Ohtomo and H.Y. Hwang. A high-mobility electron gas at the LaAlO<sub>3</sub>/SrTiO<sub>3</sub> heterointerface. *Nature*, 427(6973):423–426, 2004.
- [3] N. Nakagawa, H.Y. Hwang, and D.A. Muller. Why some interfaces cannot be sharp. *Nature Materials*, 5(3):204–209, 2006.
- [4] A. Kalabukhov, R. Gunnarsson, J. Börjesson, E. Olsson, T. Claeson, and D. Winkler. Effect of oxygen vacancies in the SrTiO<sub>3</sub> substrate on the electrical properties of the LaAlO<sub>3</sub>/SrTiO<sub>3</sub> interface. *Physical Review B*, 75(12):121404, 2007.
- [5] P.R. Willmott, S.A. Pauli, R. Herger, C.M. Schlepütz, D. Martoccia, B.D. Patterson, B. Delley, R. Clarke, D. Kumah, C. Cionca, and Y. Yacoby. Structural basis for the conducting interface between LaAlO<sub>3</sub> and SrTiO<sub>3</sub>. *Physical Review Letters*, 99(15):155502, 2007.
- [6] J.A. Boschker. *Perovskite oxide heteroepitaxy – Strain and interface engineering*. PhD thesis, University of Twente, February 2011.
- [7] M. Huijben, A. Brinkman, G. Koster, G. Rijnders, H. Hilgenkamp, and D.H.A. Blank. Structure-property relation of SrTiO<sub>3</sub>/LaAlO<sub>3</sub> interfaces. *Advanced Materials*, 21(17):1665–1677, 2009.
- [8] S. Thiel, G. Hammerl, A. Schmehl, C.W. Schneider, and J. Mannhart. Tunable quasitwo-dimensional electron gases in oxide heterostructures. *Science*, 313(5795):1942–1945, 2006.
- [9] N. Reyren, S. Thiel, A.D. Caviglia, L. Fitting Kourkoutis, G. Hammerl, C. Richter, C.W. Schneider, T. Kopp, A.S. Rüetschi, D. Jaccard, M. Gabay, D.A. Muller, J.M. Triscone, and J. Mannhart. Superconducting interfaces between insulating oxides. *Science*, 317(5842):1196–1199, 2007.
- [10] A. Brinkman, M. Huijben, M. van Zalk, J. Huijben, U. Zeitler, J.C. Maan, W.G. van der Wiel, G. Rijnders, D.H.A. Blank, and H. Hilgenkamp. Magnetic effects at the interface between non-magnetic oxides. *Nature Materials*, 6(7):493–496, 2007.
- [11] M. Huijben, G. Koster, M.K. Kruize, S. Wenderich, J. Verbeeck, S. Bals, E. Slooten, B. Shi, H.J.A. Molegraaf, J.E. Kleibeuker, S. van Aert, J.B. Goedkoop, A. Brinkman, D.H.A. Blank, M.S. Golden, G. van Tendeloo, H. Hilgenkamp, and G. Rijnders. Defect engineering in oxide heterostructures by enhanced oxygen surface exchange. *Advanced Functional Materials*, 23(25):1, 2013.
- [12] R.J.D. Tilley. *Understanding Solids: The science of Materials*. John Wiley & Sons, first edition, 2004.

- 
- [13] D.J. Griffiths. *Introduction to Electrodynamics*. Prentice-Hall, third edition, 1999.
- [14] U. Böttger. Dielectric properties of polar oxides. In R. Waser, U. Böttger, and S. Tiedke, editors, *Polar Oxides: Properties, Characterization, and Imaging*, chapter 1, pages 11–38. Wiley-VCH Verlag, 2005.
- [15] P. Chandra and P.B. Littlewood. A Landau primer for ferroelectrics. In K. Rabe, C.H. Ahn, and J.M. Triscone, editors, *Physics of Ferroelectrics: A Modern Perspective*, volume 105 of *Topics in Applied Physics*, page 69116. Springer-Verlag, 2007.
- [16] V. Garcia, S. Fusil, K. Bouzehouane, S. Enouz-Vedrenne, N.D. Mathur, A. Barthélémy, and M. Bibes. Giant tunnel electroresistance for non-destructive readout of ferroelectric states. *Nature*, 460(7251):81–84, 2009.
- [17] K.J. Choi, M. Biegalski, Y.L. Li, A. Sharan, J. Schubert, R. Uecker, P. Reiche, Y.B. Chen, X.Q. Pan, V. Gopalan, L.Q. Chen, D.G. Schlom, and C.B. Eom. Enhancement of ferroelectricity in strained BaTiO<sub>3</sub> thin films. *Science*, 306(5698):1005–1009, 2004.
- [18] T. Zhao, F. Chen, H. Lu, G. Yang, and Z. Chen. Thickness and oxygen pressure dependent structural characteristics of BaTiO<sub>3</sub> thin films grown by laser molecular beam epitaxy. *Journal of Applied Physics*, 87(10):7442–7447, 2000.
- [19] C.L. Li, Z.H. Chen, Y.L. Zhou, and D.F. Cui. Effect of oxygen content on the dielectric and ferroelectric properties of laser-deposited BaTiO<sub>3</sub> thin films. *Journal of Physics: Condensed Matter*, 13(22):52615268, 2001.
- [20] S.J. van Reeuwijk, K. Karakaya, H. Graafsma, and S. Harkema. Polarization switching in BaTiO<sub>3</sub> thin films measured by X-ray diffraction exploiting anomalous dispersion. *Journal of Applied Crystallography*, 37(2):193–199, 2003.
- [21] R. Resta and D. Vanderbilt. Theory of polarization: A modern approach. In K. Rabe, C.H. Ahn, and J.M. Triscone, editors, *Physics of Ferroelectrics: A Modern Perspective*, volume 105 of *Topics in Applied Physics*, page 3168. Springer-Verlag, 2007.
- [22] V.T. Tra, J.W. Chen, P.C. Huang, B.C. Huang, Y. Cao, C.H. Yeh, H.J. Liu, E.A. Eliseev, A.N. Morozovska, J.Y. Lin, Y.C. Chen, M.W. Chu, P.W. Chiu, Y.P. Chiu, L.Q. Chen, C.L. Wu, and Y.H. Chu. Ferroelectric control of the conduction at the LaAlO<sub>3</sub>/SrTiO<sub>3</sub> heterointerface. *Advanced Materials*, 25(24):3357–3364, 2013.
- [23] F. Schwabl. *Advanced Quantum Mechanics*. Springer-Verlag, third edition, 2005.
- [24] R. Winkler. Springer tracts in modern physics. In G. Höhler, editor, *SpinOrbit Coupling Effects in Two-Dimensional Electron and Hole Systems*, volume 191. Springer-Verlag Berlin Heidelberg, 2003.
- [25] J.J. Sakurai. *Advanced Quantum Mechanics*. Addison-Wesley, seventh edition, 1978.
- [26] O. Krupin. *Dichroism and Rashba effect at magnetic crystal surfaces of rare-earth metals*. PhD thesis, Free University of Berlin, September 2004.
- [27] J.J. Sakurai and J. Napolitano. *Modern Quantum Mechanics*. Addison-Wesley, second edition, 2011.
- [28] L. Petersen and P. Hedegård. A simple tight-binding model of spinorbit splitting of sp-derived surface states. *Surface Science*, 459(1-2):4956, 2000.
- [29] Z. Zhong, A. Tóth, and K. Held. Theory of spin-orbit coupling at LaAlO<sub>3</sub>/SrTiO<sub>3</sub> interfaces and SrTiO<sub>3</sub> surfaces. *Physical Review B*, 87(16):161102, 2013.

- [30] S. Debalde. *Interaction and confinement in nanostructures: Spin-orbit coupling and electron-phonon scattering*. PhD thesis, University of Hamburg, April 2005.
- [31] J.H. Bardarson. *Effects of Spin-Orbit Coupling on Quantum Transport*. PhD thesis, Leiden University, June 2008.
- [32] D. Bercioux. Spin-orbit interactions in semiconductor nanostructures. <http://tftp1.physik.uni-freiburg.de/teaching/Nanoelectronics/Notes/Notes%20on%20SOI.pdf>, 2011. Lecture notes.
- [33] G. Fleury, J. Li, and M. Büttiker. Introduction to Majorana fermions in condensed matter physics. presentation for the 'GDR Physique mésoscopique' meeting Aussois, December 2011.
- [34] M. Cyrot and D. Pavuna. *Introduction to Superconductivity and High-Tc Materials*. World Scientific, 1992.
- [35] J. Alicea. Majorana fermions in a tunable semiconductor device. *Physical Review B*, 81(12):125318, 2010.
- [36] A.D. Caviglia, M. Gabay, S. Gariglio, N. Reyren, C. Cancellieri, and J.M. Triscone. Tunable Rashba spin-orbit interaction at oxide interfaces. *Physical Review Letters*, 104(12):126803, 2010.
- [37] S. Nakosai, Y. Tanaka, and N. Nagaosa. Topological superconductivity in bilayer Rashba system. *Physical Review Letters*, 108(14):147003, 2012.
- [38] D. Damjanovic. Ferroelectric, dielectric and piezoelectric properties of ferroelectric thin films and ceramics. *Reports on Progress in Physics*, 61:1267–1324, 1998.
- [39] C. Harnagea. *Local piezoelectric response and domain structures in ferroelectric thin films investigated by voltage-modulated force microscopy*. PhD thesis, Martin Luther University of Halle-Wittenberg, May 2001.
- [40] A. Gruverman. Principles and applications of piezoresponse force microscopy. presentation for the CNMS Workshop on Piezoresponse Force Microscopy, October 2007.
- [41] R.J.A. Steenwelle. Characterization of piezo- and ferroelectric thin films by scanning probe techniques. Master thesis, University of Twente, September 2007.
- [42] A.L. Kholkin, S.V. Kalinin, A. Roelofs, and A. Gruverman. Review of ferroelectric domain imaging by piezoresponse force microscopy. In S. Kalinin and A. Gruverman, editors, *Scanning Probe Microscopy: Electrical and Electromechanical Phenomena at the Nanoscale*, chapter I.6, pages 173–214. Springer, 2007.
- [43] D.A. Scrymgeour and V. Gopalan. Nanoscale piezoelectric response across a single antiparallel ferroelectric domain wall. *Physical Review B*, 72(2):024103, 2005.
- [44] S. Jesse, A.P. Baddorf, and S.V. Kalinin. Switching spectroscopy piezoresponse force microscopy of ferroelectric materials. *Applied Physics Letters*, 88(6):062908, 2006.
- [45] G. Koster, B.L. Kropman, G.J.H.M. Rijnders, D.H.A. Blank, and H. Rogalla. Quasi-ideal strontium titanate crystal surfaces through formation of strontium hydroxide. *Applied Physics Letters*, 73(20):2920–2922, 1998.
- [46] F.J.G. Roesthuis. *ICE Manual for standard SrTiO<sub>3</sub> substrate treatment for TiO<sub>2</sub> termination*. ICE, 2007. Downloadable from ICE Wiki.

- 
- [47] M. Ohring. *Materials Science of Thin Films – Deposition and Structure*. Academic Press, second edition, 2002.
- [48] Y. Yang, Z. Wang, J.F. Li, and D. Viehland. Pulsed laser deposition of BaTiO<sub>3</sub> thin films on different substrates. *Journal of Nanomaterials*, 2010:Article ID 756319, 2010.
- [49] J. Zhang, D. Cui, H. Lu, Z. Chen, Y. Zhou, L. Li, G. Yang, S. Martin, and P. Hess. Structural behavior of thin BaTiO<sub>3</sub> film grown at different conditions by pulsed laser deposition. *Japanese Journal of Applied Physics*, 36(1A):276–283, 1997.
- [50] C. Chmiel. High capacitance thin films. Bachelor thesis, University of Twente, 2011.
- [51] J. Rainer. private communication. February 2013.
- [52] A. Visinoiu, M. Alexe, H.N. Lee, D.N. Zakharov, A. Pignolet, D. Hesse, and U. Gösele. Initial growth stages of epitaxial BaTiO<sub>3</sub> films on vicinal SrTiO<sub>3</sub> (001) substrate surfaces. *Journal of Applied Physics*, 91(12):10157–10162, 2002.
- [53] T. Ohnishi and K. Takada. Epitaxial thin-film growth of SrRuO<sub>3</sub>, Sr<sub>3</sub>Ru<sub>2</sub>O<sub>7</sub>, and Sr<sub>2</sub>RuO<sub>4</sub> from a SrRuO<sub>3</sub> target by pulsed laser deposition. *Applied Physics Express*, 4(2):025501, 2011.
- [54] W.R. Thurber. Hall effect measurements algorithm. [www.nist.gov/pml/div683/hall\\_algorithm.cfm](http://www.nist.gov/pml/div683/hall_algorithm.cfm). visited: November 2012.
- [55] S. Datta. *Electronic Transport in Mesoscopic Systems*. Cambridge University Press, 1995.
- [56] M. Huijben, G. Rijnders, D.H.A. Blank, S. Bals, S. van Aert, J. Verbeeck, G. van Tendeloo, A. Brinkman, and H. Hilgenkamp. Electronically coupled complementary interfaces between perovskite band insulators. *Nature Materials*, 5(7):556–560, 2006.
- [57] P.D. Eerkes, W.G. van der Wiel, and H. Hilgenkamp. Modulation of conductance and superconductivity by top-gating in LaAlO<sub>3</sub>/SrTiO<sub>3</sub> 2-dimensional electron systems. Manuscript submitted for publication, June 2013.
- [58] D. Völtzke, S. Gablenz, H.P. Abicht, R. Schneider, E. Pippel, and J. Woltersdorf. Surface modification of barium titanate powder particles. *Materials Chemistry and Physics*, 61(2):110–116, 1999.
- [59] S.A. Hayward, H.J. Redfern, S.A.T. and Stone, M.G. Tucker, K.R. Whittle, and W.G. Marshall. Phase transitions in BaTiO<sub>3</sub>: a high-pressure neutron diffraction study. *Zeitschrift fuer Kristallographie*, 220(8):735–739, 2005.
- [60] S. Piskunov, E. Heifets, R.I. Eglitis, and G. Borstel. Bulk properties and electronic structure of SrTiO<sub>3</sub>, BaTiO<sub>3</sub>, PbTiO<sub>3</sub> perovskites: an ab initio HF/DFT study. *Computational Materials Science*, 29(2):165178, 2004.
- [61] Y. Xiao. *The influence of oxygen vacancies on domain patterns in ferroelectric perovskites*. PhD thesis, California Institute of Technology, September 2004.
- [62] D.P. Cann, J.P. Maria, and C.A. Randall. Relationship between wetting and electrical contact properties of pure metals and alloys on semiconducting barium titanate ceramics. *Journal of Materials Science*, 36(20):4969–4976, 2001.
- [63] H.L. Skriver and N.M. Rosengaard. Surface energy and work function of elemental metal. *Physical Review B*, 46(11):7157–7168, 1992.

- [64] Y.C. Chen, C.H. Ko, Y.C. Huang, J.C. Yang, and Y.H. Chu. Domain relaxation dynamics in epitaxial BiFeO<sub>3</sub> films: Role of surface charges. *Journal of Applied Physics*, 112(5):052017, 2012.
- [65] M. Dawber, K.M. Rabe, and J.F. Scott. Physics of thin-film ferroelectric oxides. *Reviews of Modern Physics*, 77(4):1083–1130, 2005.
- [66] W.J. Son, E. Cho, B. Lee, J. Lee, and S. Han. Density and spatial distribution of charge carriers in the intrinsic n-type LaAlO<sub>3</sub>-SrTiO<sub>3</sub> interface. *Physical Review B*, 79(24):245411, 2009.
- [67] Y. Wang, M.K. Niranjan, K. Janicka, J.P. Velev, M.Y. Zhuravlev, S.S. Jaswal, and E.Y. Tsymbal. Ferroelectric dead layer driven by a polar interface. *Physical Review B*, 82(9):094114, 2010.
- [68] Y. Hikita, Y. Kozuka, T. Susaki, H. Takagi, and H.Y. Hwang. Characterization of the Schottky barrier in SrRuO<sub>3</sub>/Nb:SrTiO<sub>3</sub> junctions. *Applied Physics Letters*, 90(14):143507, 2007.
- [69] M.B. Okatan and S.P. Alpay. Imprint in ferroelectric materials due to space charges: A theoretical analysis. *Applied Physics Letters*, 95(9):092902, 2009.
- [70] W.L. Warren, D. Dimos, G.E. Pike, B.A. Tuttle, M.V. Raymond, R. Ramesh, and J.T. Evans Jr. Voltage shifts and imprint in ferroelectric capacitors. *Applied Physics Letters*, 67(6):866–868, 1995.
- [71] V.T. Tra, J.W. Chen, P.C. Huang, B.C. Huang, Y. Cao, C.H. Yeh, H.J. Liu, E.A. Eliseev, A.N. Morozovska, J.Y. Lin, Y.C. Chen, M.W. Chu, P.W. Chiu, Y.P. Chiu, L.Q. Chen, C.L. Wu, and Y.H. Chu. Ferroelectric control of the conduction at the LaAlO<sub>3</sub>/SrTiO<sub>3</sub> heterointerface. *Advanced Materials*, 25(24):3357–3364, 2013. Supporting Information (online).
- [72] M.E. Lines and A.M. Glass. *Principles and Applications of Ferroelectric and Related Materials*. Clarendon Press, 1977.



# Appendix A

## Theory of spontaneous polarization

In this appendix the theory of spontaneous polarization is discussed. In section 1.3 a large part of the material covered in this appendix was summarized, but most of the math and physics was omitted. For completeness and clarity these are presented here.

### A.1 Ginzburg-Landau theory of ferroelectric phase transition

Ferroelectric materials have two phases: a paraelectric phase and a ferroelectric phase. In both phases the stoichiometry is identical, only the dimensions of the unit cells are changed and atoms displaced. This difference results in different properties of the material. Ferroelectric materials are only ferroelectric in the ferroelectric phase, whereas they are only dielectric in the paraelectric phase. This phase change occurs at a certain temperature called the Curie temperature or Curie point  $T_C$ . At temperatures lower than the Curie temperature the material favours a spontaneous polarization so that material is ferroelectric. Barium titanate has a Curie temperature of  $T_C = 135^\circ\text{C}$  [14] and is thus ferroelectric at room temperature.

Such a phase transition can phenomenologically be well described with a thermodynamic theory. The theory for ferroelectricity discussed here is the Ginzburg-Landau theory of ferroelectric phase transition, which reliably describes the equilibrium behaviour of a ferroelectric near a phase transition. The basic assumptions of this macroscopic theory are that (1) the primary variables that drive the phase transition are the dielectric displacement  $D_i$  and the electric field  $E_i$ , (2) the relevant equation of a phase state can be represented by a polynomial and (3) the same polynomial can be used in both phase states, above and below the Curie temperature. The following theoretical discussion is based upon references [14, 15, 72].

The most convenient thermodynamic potential for this theory is the elastic Gibbs free energy

$$G_e = G + E_i D_i, \quad (\text{A.1})$$

with  $G$  the Gibbs free energy,  $E$  the electric field,  $D$  the dielectric displacement and  $i \in \{1, 2, 3\}$  an index corresponding to the  $x$ ,  $y$  and  $z$  direction, respectively. The elastic Gibbs free energy is generally a function of temperature  $T$ , mechanical stress  $X$  and dielectric displacement  $D$ . However, for barium titanate and most other ferroelectrics, the elastic Gibbs free energy can be simplified by the fact that the spontaneous polarization is directed along one crystallographic axis so that  $D_i = D$  and the fact that the paraelectric phase is centrosymmetric. Due to this symmetry all asymmetric terms in the elastic Gibbs free energy near the phase transition are discarded. Furthermore, all stresses can be safely assumed zero. With these simplifications the elastic Gibbs free energy can be represented as a series expansion around the phase transition:

$$G_e(T, D) = \frac{1}{2}\alpha_1 D^2 + \frac{1}{4}\alpha_2 D^4 + \frac{1}{6}\alpha_3 D^6 + h.o.. \quad (\text{A.2})$$

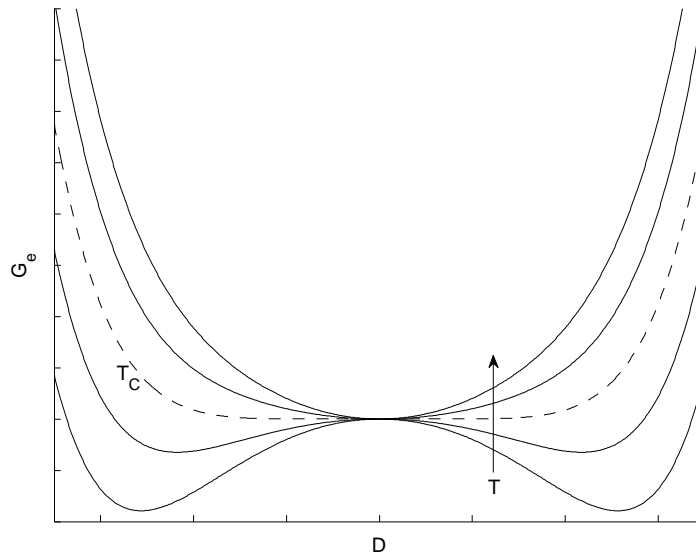


Figure A.1: The elastic Gibbs free energy polynomial of equation (A.2) for different temperatures. The dotted line is at  $T_C$ , while above and below this line  $T > T_C$  and  $T < T_C$ , respectively.

From equation (A.1) it is clear that differentiating this polynomial with respect to the dielectric displacement results in the electric field:

$$E(T, D) = \alpha_1 D + \alpha_2 D^3 + \alpha_3 D^5 + h.o.. \quad (\text{A.3})$$

To find the spontaneous polarization direction of the ferroelectric the electric field is set to zero. Since the dielectric displacement is given by

$$D = \epsilon_0 \epsilon_f E + P, \quad (\text{A.4})$$

$D = P$  when  $E = 0$ . With this condition both equation (A.2) and equation (A.3) can be equally well expressed as functions of polarization. In these equations the polarization is the order parameter, it is zero in the paraelectric phase and changes continuously to a finite value in the ferroelectric phase.

The value of the spontaneous polarization  $P_s$  is found at the stable minima of the elastic Gibbs free energy. For the polynomial to have at least two stable minima in the ferroelectric phase, corresponding to the two directions of the spontaneous polarization, the first coefficient  $\alpha_1$  has to be less than zero. According to the Devonshire theory this coefficient is expressed as

$$\alpha_1 = \beta (T - T_0), \quad (\text{A.5})$$

with  $T_0$  the Curie-Weiss temperature<sup>1</sup> and constant  $\beta > 0$ . All other coefficients are temperature independent. These coefficients get to fulfill the condition  $\alpha_2 = \gamma < 0$  and  $\alpha_3 = \delta > 0$ . A transition with these coefficients is called a first order (discontinuous) phase transition. It describes the ferroelectric behaviour of (bulk) barium titanate well, as well as other ferroelectrics. Yet, some ferroelectrics do not have a first order but second order (continuous) phase transition. In this section only first order phase transitions in relation to ferroelectricity are discussed.

<sup>1</sup>This is a different temperature than the Curie temperature  $T_C$  introduced at the beginning of this section, since  $T_0 \leq T_C$ , as can be seen in figure A.3. When  $T < T_C$  the material is in the ferroelectric phase, however as long as  $T \geq T_0$  the paraelectric phase, although metastable, coexists with the ferroelectric phase.

The first order phase transition at zero field occurs when both equation (A.2) and equation (A.3) are zero:

$$\begin{aligned} \frac{1}{2}\beta(T - T_0)P^2 - \frac{1}{4}|\gamma|P^4 + \frac{1}{6}\delta P^6 &= 0 \\ \beta(T - T_0)P - |\gamma|P^3 + \delta P^5 &= 0. \end{aligned} \quad (\text{A.6})$$

Solving these coupled equations for temperature  $T$  will provide the Curie temperature as a function of the Curie-Weiss temperature. The sought-after expression is

$$T_C = T = T_0 + \left(\frac{3}{16}\right) \left(\frac{\gamma^2}{\beta\delta}\right). \quad (\text{A.7})$$

The spontaneous polarization states can be found by calculating the minima of the elastic Gibbs free energy. These are temperature dependent and located at

$$P_s = \pm \sqrt{\frac{|\gamma| + \sqrt{|\gamma|^2 - 4\delta\beta(T - T_0)}}{2\delta}}. \quad (\text{A.8})$$

At  $T = T_C$  this expression can be simplified to  $P_s = \pm\sqrt{3|\gamma|/4\delta}$  using equation (A.7).

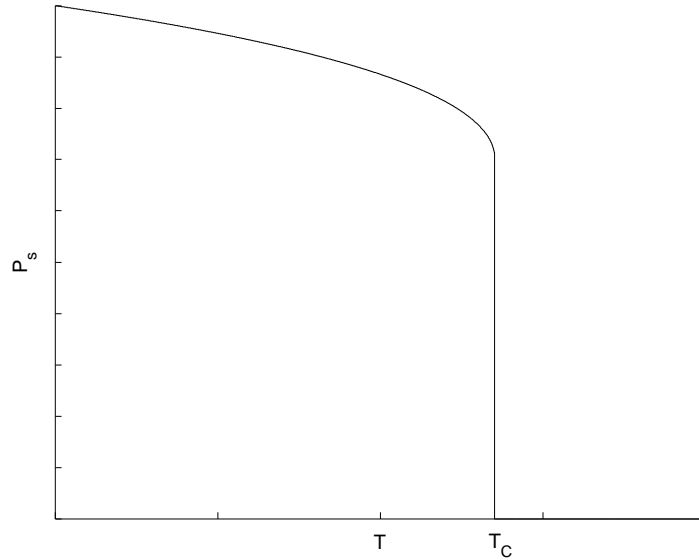


Figure A.2: The spontaneous polarization as a function of temperature for a first order ferroelectric phase transition, as described by the absolute value of equation (A.8).

Furthermore, the dielectric susceptibility  $\chi$  of the ferroelectric material can be deduced from this simple theory, since

$$\frac{1}{\chi} = \left. \frac{\partial^2 G_e}{\partial D^2} \right|_{D=P_s}. \quad (\text{A.9})$$

This function is discontinuous at the Curie temperature,

$$\frac{1}{\chi} = \begin{cases} \frac{3|\gamma|^2}{4\delta} + 8\beta(T_c - T) & T \rightarrow T_C^- \\ \frac{3|\gamma|^2}{16\delta} + \beta(T_c - T) & T \rightarrow T_C^+ \end{cases}, \quad (\text{A.10})$$

and reduces to the well-known Devonshire expression of equation (A.5) at temperatures above the Curie-Weiss temperature. The dielectric susceptibility of a ferroelectric can be experimentally determined. From the slope of a  $1/\chi$  versus  $T$  graph the coefficient  $\beta$  can then be determined, for barium titanate this value is found to be  $\beta \approx 5.6 \cdot 10^{-6}$  [14].

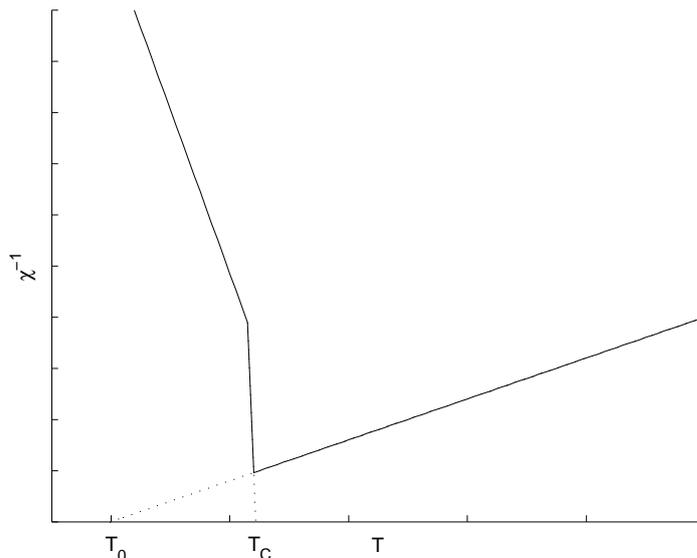


Figure A.3: The inverse dielectric susceptibility as a function of temperature for a first order ferroelectric phase transition as described in equation (A.10). At  $T = T_C$  the susceptibility is discontinuous, a characteristic of a first order transition, also  $T_0 < T_C$  is indicated.

## A.2 Ferroelectric hysteresis and domains

Ferroelectric materials can have multiple spontaneous polarization directions. A spatial part of such a material with a single and constant spontaneous polarization direction is called a domain. Some ferroelectrics are single-domain and have a single dominant polarization direction, whereas others are multi-domain and have multiple non-dominant polarization directions.

An externally applied electric field can change the polarization direction to another spontaneous polarization. This can be understood from the Ginzburg-Landau theory discussed in the previous section. The spontaneous polarization directions are determined from the minima of the elastic Gibbs free energy of equation (A.2). The dielectric displacement  $D$  in this polynomial is a function of the electric field, as can be seen from equation (A.4). The elastic Gibbs free energy function thus changes when an external electric field is applied. This also influences its minima and thus the spontaneous polarization direction.

In the ferroelectric phase the minima of the elastic Gibbs free energy are separated by a barrier. Therefore a small electric field will not change the spontaneous polarization immediately. A high enough electric field lowers this barrier and reduces the two minima into a single minimum. This minimum is then the dominant or even only spontaneous polarization direction. The direction of the electric field determines which of the two minima or polarization directions will survive. Due to this barrier the changing of polarization is a hysteretic effect. This hysteresis effect is visible in a plot of polarization versus electric field, as can be seen in figure A.4. Such a hysteresis loop is commonly called a polarization loop.

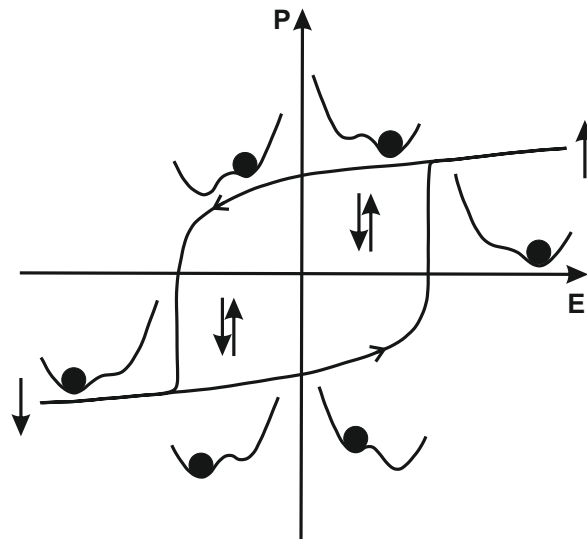


Figure A.4: A ferroelectric hysteresis loop with schematically shown the form of the elastic Gibbs free energy curve at specific electric fields. The dot indicates in which polarization state the ferroelectric is in and the arrows indicate the polarization direction(s). Figure after reference [15].



## Appendix B

# A short user guide to Piezoresponse Force Microscopy

This short user guide is intended for users who have no experience in piezoresponse force microscopy (PFM), but do have some experience with atomic force microscopy (AFM). It serves as a practical guide in which the new user is guided through the steps of typical PFM measurements. The most important settings are discussed as well as the different types of measurements that are typically performed with a PFM. This guide is written specifically for the Bruker Dimension Icon AFM with the standard Nanoscope software of the manufacturer for controlling the system and analyzing the data<sup>1</sup>.

## B.1 Preparations

### B.1.1 Sample

During a PFM measurement an electric field is applied over the sample, perpendicular to the sample surface. The tip of the PFM probe is used as one of the electrodes, while a conducting layer in the sample is used as a back electrode. One of these electrodes is biased and the other is grounded, which can be assigned by the user.

The application of an electric field during a PFM measurements puts some constraints on the sample. First, it must have a conducting layer. This conducting layer must be below the piezoelectric layer which has to be measured. Second, contact has to be made to this layer. Either the ground or the bias is applied by the PFM to a metallic AFM specimen disc. The sample has to be mounted to this specimen disc and the conducting layer should be in contact with this disc. When a conducting substrate is used, gluing the sample to the plate with silver paint or paste is all that needs to be done. In other cases contact has to be made to the conducting layer. There are three commonly used techniques for that: scratching, bonding or contact sputtering.

The scratching technique is the simplest way to make contact to your back electrode and is often used. With this technique a deep scratch is made at one corner of the sample. This is done with a surgical blade. Then the sample is glued onto the specimen disc with silver paint. A blob of silver paint is put over the scratched corner so that it is also in contact with the specimen disc. Although this technique is simple, it is not very precise. One has to make sure that the scratch is deep enough to contact the electrode layer. Furthermore, this technique does not work well with thick layers and specific multilayers. The scratch technique is also destructive and may harm your sample if it is badly performed.

---

<sup>1</sup>The analyzing tool box of this software, Nanoscope Analysis, can be downloaded from [ftp://sboftp.bruker-nano.com/outgoing/GPTech/Software/NanoScope\\_Analysis/](ftp://sboftp.bruker-nano.com/outgoing/GPTech/Software/NanoScope_Analysis/). This software can read the native file type of the Bruker Dimension Icon AFM and PFM including all used settings.

The other two techniques, bonding and contact sputtering, are better to control and less destructive. The bonding technique works well for a thin layer on top of your electrode layer. With this technique the wire bonder is used to ultrasonically bond a wire to the sample. The wire is then cut from the bonder and with a dot of silver paint connected to the specimen disc. The contact sputtering technique works fine for all thicknesses if argon etching can be used on the sample to etch to the electrode layer. After this etching step, gold electrodes can be sputtered. This technique is more work, but can be performed fairly easy with a shadow mask if the sample allows such a mask to be used.

### **B.1.2 Tip**

PFM measurements are performed in contact mode, but a different tip is used than in AFM contact mode. The PFM tip must have a conductive coating to apply a bias or ground to the tip. Typically silicon tips are used with a Cr/Pt conductive coating. The resonance frequency of these tips is 75 kHz. These PFM tips have a larger cantilever than normal AFM tips. The PFM tip should be in 'tip holder 1' of the NanoLab's Dimension Icon AFM. In the logbook this tip is denoted as 'PFM1'. Before performing a PFM measurement make sure the right tip is installed.

## **B.2 Measurements**

Before the measurement can be started, the laser should be aligned on the tip and its reflection should be centered on the detector. Furthermore, the sample should be mounted on the measurement stage. These procedures are identical to the normal AFM procedures and are therefore not discussed in this document.

### **B.2.1 PFM mode**

To start a PFM measurement the software has to be in the PFM mode. This means that one has to open the right experiment in the Nanoscope software. This is done on starting the Nanoscope software by selecting the experiment category 'Electrical & Magnetic', next the experiment group 'Piezoresponse' and then the experiment 'Piezoresponse - Vertical & Horizontal Domains'. The other experiment, 'Optimal Vertical Domains', may be used if the plane of polarization is known a priori. The PFM mode will open once the green button with 'Load Experiment' is pressed. The PFM mode can also be opened if another mode is open. Then one can click on 'Experiment' in the menu bar and next on 'Select Experiment'. The same window will then pop-up so that the discussed steps can be followed next.

Now the alignment and navigation steps can be performed. These are identical to the normal AFM steps and are therefore not discussed here.

### **B.2.2 Tuning the Tip**

The tip must operate at a suited frequency. The selected frequency depends on the type of measurement that one wants to perform. To set the suited frequency one selects 'Sweep' in the Workflow Toolbar at the left of the screen. A new window will appear with a graph and a bar with settings, this window is depicted in figure B.1. For tuning a PFM tip it is best to use two graphs. Therefore make sure that 'Channel 1' is set to the data type 'Amplitude 1' and 'Channel 2' to the data type 'Phase 1'.

Both graphs might initially seem very noisy or do not show a clear signal at all. The first step to change this is changing the scale. Click with the right mouse button on one of these graphs and select 'Scale' in the menu that appears. A window will pop-up. In this window

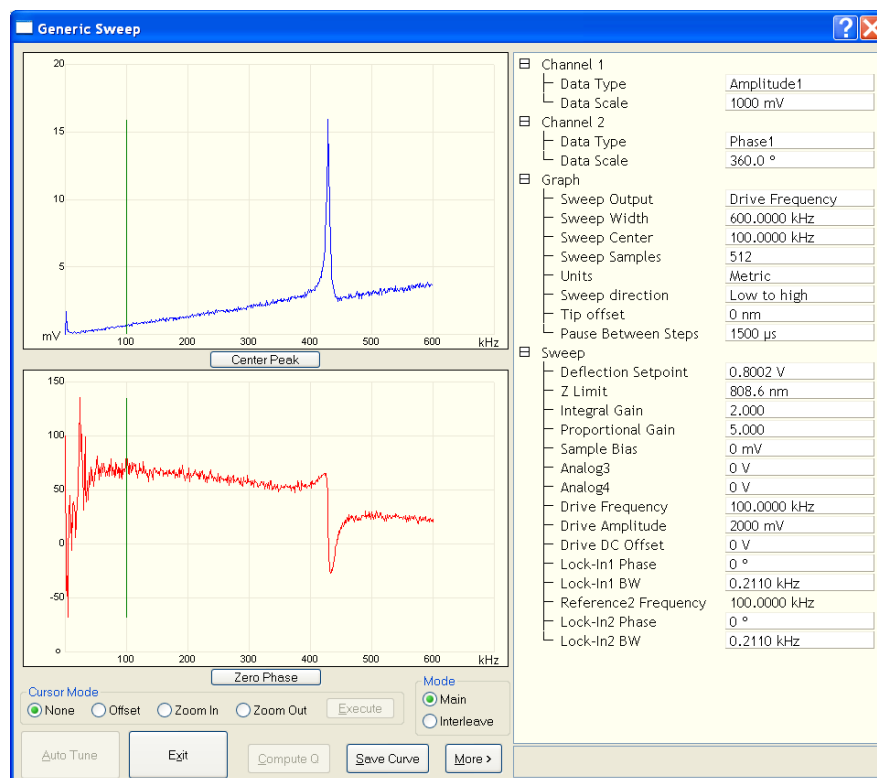


Figure B.1: Tuning the PFM tip in the 'Generic Sweep' menu, with the settings for PFM reading displayed.

choose 'Auto scale' and click 'Ok'. Do the same for the other graph. Now some sort of signal should be clearly visible.

The Cr/Pt tips typically used have a resonance frequency of 75 kHz, as was mentioned before. This resonance peak is important for judging the tip quality and selecting the suited frequency. To make this peak visible, set below 'Graph' the 'Sweep width' to 400-600 kHz and apply a 'Drive Amplitude' below 'Sweep'. Start with a small 'Drive Amplitude' and increase it until a resonance peak appears. Increasing the voltage should reduce the noise in the amplitude signal and increase the peak. However, a too high voltage may destroy your sample surface and the coating of the tip. The resonance peak should appear near 400 kHz.

From these two sweep graphs it is best to judge the tip quality. The peak in the amplitude signal should be large, fairly sharp and turned upward. There should be no clear dip downward right in front of this peak. Furthermore the phase should show at the peak frequency a large phase shift. At lower frequencies the phase may be instable, that is no problem, if only near the resonance the phase is not largely unstable and a clear phase shift at resonance is present. If the amplitude has no resonance peak or a peak which is not significantly higher than the noise level, it should be replaced. Increasing the voltage should decrease the noise, if this is not the case, the tip should be replaced. Furthermore, if there is a significant dip in front of the peak, it is also better to replace the tip. The resonance frequency can be shifting a few Hertz over time, this is generally no problem. For ramp measurements, however, it is advised to check that the drive frequency is still centered at the peak before starting a ramp at a different spot. The sweep graphs are strongly position dependent due to the interaction with the sample surface. The drive frequency might therefore needed to be changed.

Below the sub menu 'Graph' there is another frequency, the 'Drive frequency'. The value of this frequency depends on the type of measurement that one would like to perform. For topographical measurements of the phase and amplitude of a piezoelectric sample, one should

be far below the resonance peak. For a peak near 400 kHz a frequency of 20 kHz is commonly used. One may change this value a bit to a frequency where the phase is more stable. For ramp measurements the 'Drive frequency' should be on resonance. The frequency should then be tuned to the peak frequency. This can be done precisely by using the green line in the graph as an indicator. This green line indicates the drive frequency.

### B.2.3 Topographical measurements: reading

In topographical measurements the surface of the sample is scanned to probe for piezoelectric domains. Both in-plane and out-of-plane domains can be measured simultaneously as well as the standard AFM topography and deflection error. This particular measurement is termed reading in this document, since it reads out the existing piezoelectric state without modifying it. This is different from writing and ramp measurements, in which a bias is applied to change the piezoelectric state.

To perform this measurement one should open the 'Scan' section by clicking 'Scan' in the Workflow Toolbar. The windows in figure B.2 and figure B.3(a) now appear. First check and change the settings. The settings in the 'Scan' sub menu are set just as in an AFM measurement, only the 'Scan Rate' must be below 1.00 Hz, typically 0.500 Hz is used. This slow scan rate is needed, because there are two lock-in amplifiers which cannot operate properly at high scan rates. In the sub menu 'Limits' the 'Z Range' should be reduced to a value close to one, it may be lower, but keep in mind that the bar of the 'Real Time Status' should be green. If the sample roughness does not tolerate this value, choose the lowest possible one. Set in the sub menu 'Other' either the 'Tip Bias Control' to 'Tip Bias' and the 'Sample Bias Control' to 'Ground' or the 'Tip Bias Control' to 'Ground' and the 'Sample Bias Control' to 'Sample Bias'. This will determine the direction of the applied electric field. Now the 'Drive Routing' in the 'Lock-In 1' sub menu should be set either to 'Sample' or 'Tip', while the 'Lock-In 2' should always be set to 'Harmonic'. The 'Drive Amplitude' in the 'Lock-in 1' sub menu should have initially a low value, which can be increased while scanning. However, this low value must have resulted in a resonance peak during the tuning of the tip. Starting with too high voltages may destroy the sample surface.

Before the actual measurement is started, select the needed measurement channels in the small scan images. For a PFM measurement typically the AFM channels 'Height Sensor' and 'Deflection Error' are selected as well as the specific PFM channels 'Amplitude 1', 'Phase 1', 'Amplitude 2' and 'Phase 2'. From these it is advised to assign the 'Height Sensor', 'Amplitude 1', 'Phase 1' and 'Phase 2' to the larger scan views. These will give during the measurement the most important data for most piezoelectric materials. Now the settings are suited to start the measurement.

During the first measurement optimize the settings. Change the scale of the image channels and make sure that the phase is centered around zero degrees. Sometimes the phase data is noisy, this can be reduced by changing the 'Lock-In Phase' and/or the 'Lock-In BW' in the 'Lock-In' sub menus. This is best done by playing around with the values. Also both gains in the 'Feedback' sub menu might contribute to a better signal. If there is a strong resemblance between the images of the topography and the amplitude and phase, try to reduce the 'Drive Amplitude'.

### B.2.4 Topographical measurements: writing

With the PFM technique not only the piezoresponse signal can be measured, it can also be influenced by applying a voltage. When this voltage is, for example, higher than the switching voltage, the piezoelectric domains are aligned in the same direction. By scanning the tip a large domain can be created. In principle all types of domain shapes can be created with this procedure. During this process only the 'Height Sensor' and the 'Deflection Error' can be

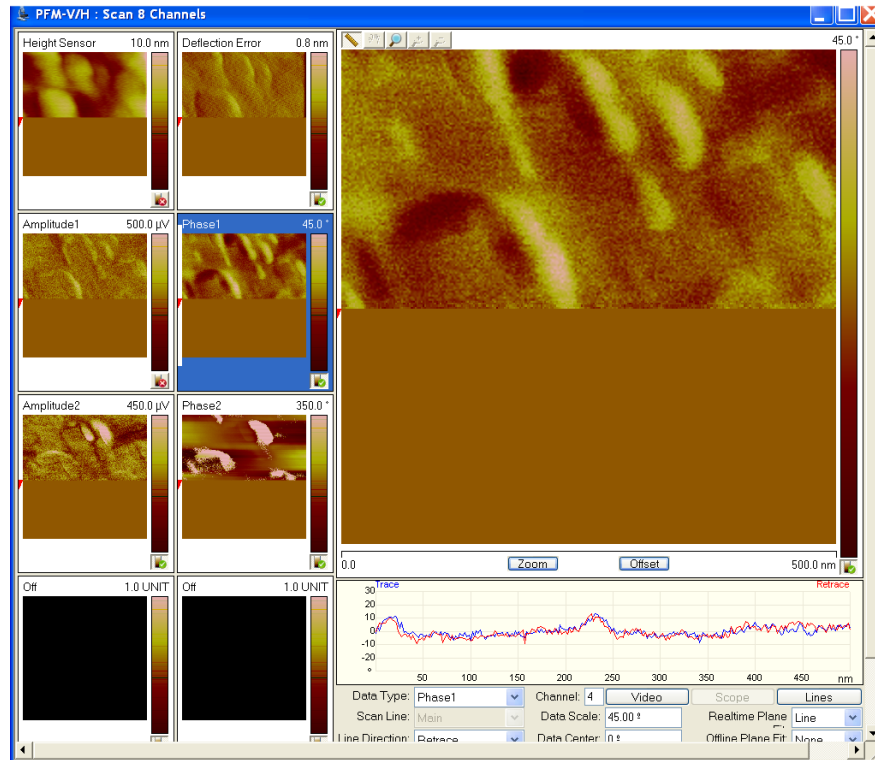


Figure B.2: The Scan window displaying six active scan channels during a PFM reading measurement.

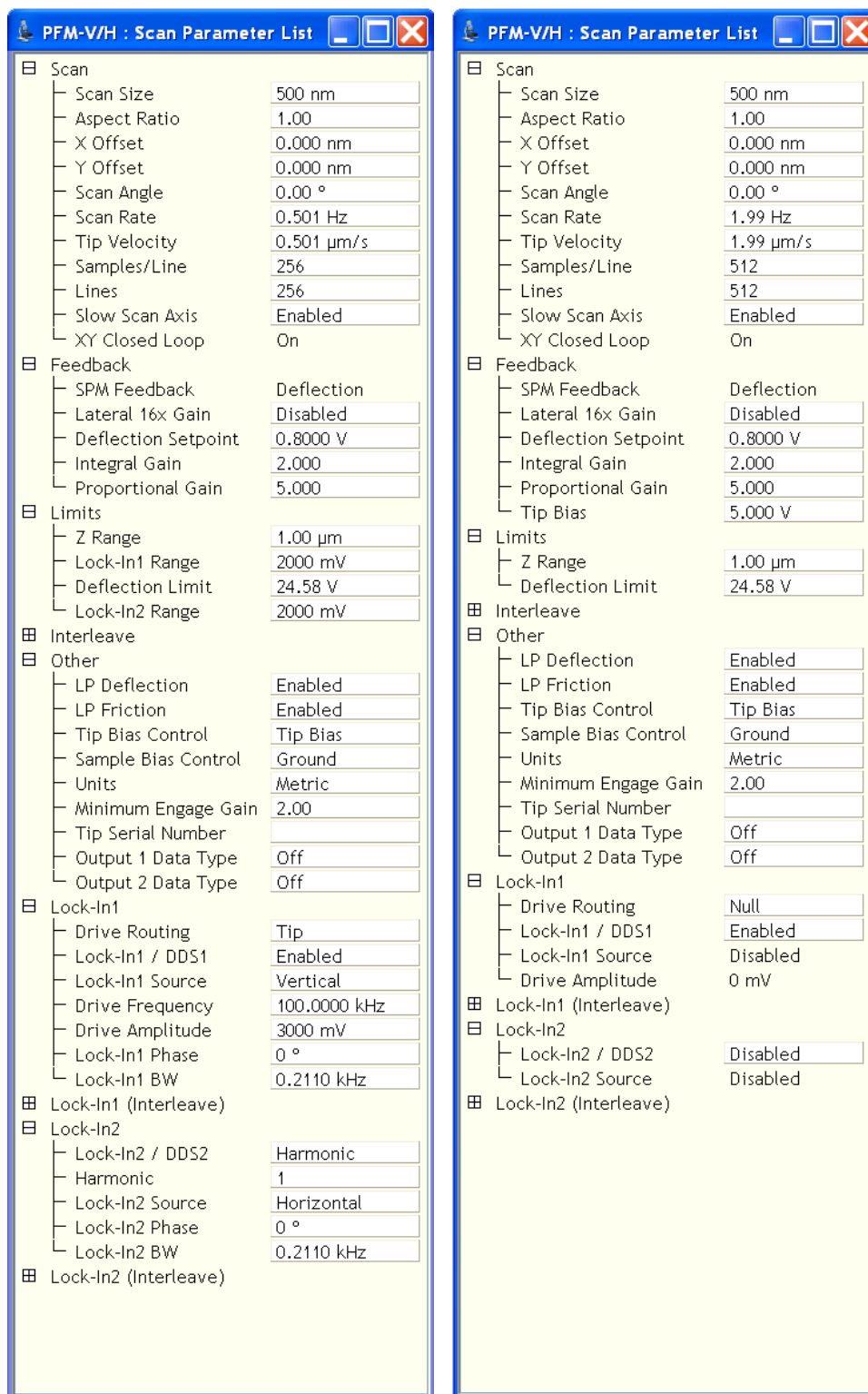
measured. This description has probably made clear why this topographical measurement is termed writing in this document.

To do this writing both lock-in amplifiers have to be turned off. This is done by setting the 'Drive Routing' to 'Null' in the lock-in sub menus. By doing this the amplitude and phase channels become inactive, although the phase channels may give some signal it is certainly no piezoresponse signal anymore. Since the lock-ins are no longer used, the 'Scan Rate' in the 'Scan' sub menu may be increased to higher scan rates. These and the following settings in this subsection are displayed in figure B.3(b).

To do the writing a bias voltage must be applied. This can be done in the 'Feedback' sub menu by setting the 'Tip Bias' to a certain voltage. It is advised to start with a low voltage, for instance 0.500 V. This voltage can then be increased slowly. One should increase the 'Tip Bias' for as long as there is no structural change in the topography shown in the 'Height Sensor' data. As soon as the surface starts to change (a clear different trace and retrace, for example), go to the previous (lower) voltage. This procedure is generally destructive, one should therefore use an unimportant spot on the sample to find this voltage, for example near the edge of the sample.

Now the sample can be scanned with the optimized bias voltage. Making structures in the domains, for example lines of different domains, is possible by changing the voltage. This can, for instance, be done by changing a positive bias to a negative bias. One can directly go to zero, but from zero to a negative voltage should again be done in steps, since a negative voltage may switch the piezoelectric state at a different absolute bias than a positive voltage. During these steps watch again the topography closely for any structural change. If so, go back to the previous (higher) voltage.

Before starting a reading measurement after this writing measurement, make sure that the 'Tip Bias' is set to zero again. Also decrease the 'Scan Rate' to a value below 1.00 Hz



(a)

(b)

Figure B.3: The 'Scan Parameter List' in which the settings of the scan can be checked and changed. In (a) the settings for PFM reading are displayed and in (b) the settings for PFM writing are displayed.

before reactivating the lock-ins.

### B.2.5 Spectroscopy measurements

With spectroscopy or ramp measurements one can locally probe the piezoelectric effect of the sample. With a ramp a linear increasing voltage is applied during the trace, starting and ending at specified voltages. During the retrace the ramp is inverted and a linear decreasing voltage is applied. With these measurements the in-plane and out-of-plane amplitude and phase can be measured. If the sample is piezoelectric and the ramp voltages are well chosen, the local switching behaviour can be observed. In that case the amplitude graph should show a butterfly shaped loop with minima at the switching voltages. In the phase graph a hysteresis loop should appear with a phase shift at the same switching voltages as in the amplitude graph. The in-plane and out-of-plane graphs should differ.

To perform a spectroscopy measurement one should start with changing settings in the 'Scan' section of the Nanoscope software. To get there click 'Scan' in the Workflow Toolbar. Ramp measurements should be performed at a fixed position, therefore one should change the 'Scan size' in the sub menu 'Scan' to zero. Also increase the 'Deflection Setpoint' in the 'Feedback' sub menu to a higher value, for instance 0.800 V, but do not go to 1.000 V or above.

Make sure that the menu is expanded and check if the 'Z Range' in the sub menu 'Limits' is low. The 'Z Range' should have preferably a value close to one if the sample roughness will tolerate this, otherwise choose the lowest possible value above one. Check also in the sub menu 'Other' that either the 'Tip Bias Control' is on 'Tip Bias' and the 'Sample Bias Control' is on 'Ground' or that the 'Tip Bias Control' is on 'Ground' and the 'Sample Bias Control' is on 'Sample Bias'. In the 'Lock-In 1' sub menu the 'Drive Routing' should then be either on 'Sample' or 'Tip', while the 'Lock-In 2' should always be on 'Harmonic'. The 'Drive Amplitude' in the 'Lock-in 1' sub menu should be on the value set during the tuning of the tip or during a topographical measurement.

Now the 'Ramp' section of the software can be opened in the 'Workflow Toolbar'. The window of figure B.4 appears, however, the graphs displayed in this figure should still be empty. The software should still be in expanded mode and the bar of the 'Real Time Status' should turn red. In the sub menu 'Ramp' set the 'Ramp Output' to 'Drive DC Offset' and choose for 'Ramp Begin' and 'Ramp End' suitable voltages. It is advised to start with low absolute voltages. These voltages can be slowly increased after a ramp has been made and no switching behaviour was observed. The 'Ramp Rate' in the same sub menu is best to be set to a low value, for example 0.100 Hz.

In the 'Ramp' section three graphs are visible, each coupled to a different measurement channel. During each ramp three channels can be measured simultaneously. One has to make a suitable choice for these channels. It is best to measure at least the two phases, since these bear the clearest signals of piezoelectricity. The third channel can then be used to measure the in-plane or out-of-plane amplitude, the choice of which depends on the direction of the largest expected piezoresponse. To assign these channels select above each graph the right 'Data Type'.

Now everything has been set to start the ramp. This is done by clicking on the first button depicting a cantilever and an arrow in the tool bar above the graphs. A single ramp is then performed. The other buttons also start a ramp but of a different type or will start a continuous sequence of ramps. Feel free to try this, but one commonly wants to use the single ramp, which one can repeat of course manually.

The 'X Offset' and 'Y Offset' in the 'Ramp' sub menu can be used to probe the local piezoelectricity of the sample at a different spot. If repeated ramps influence the switching behaviour in the ramps, it is best to change the offsets with values of at least 30 nm. This value is chosen, because it is the radius which is probed by the tip during a ramp measurement.



Figure B.4: The Ramp window displaying three active ramp channels during a PFM spectroscopy measurement. The ramps displayed are far from ideal: the phase change is too small in the 'Phase 1' channel and no clear butterfly loop is observed in the 'Amplitude 1' channel.

With an offset of more than 30 nm one is sure not to measure influences of prior ramps.

The graphs can be saved in the same manner as one would normally save AFM pictures. However, there is no separate post-processing software like Gwyddion available which can read these ramp files, only the Nanoscope software is able to process these (see the footnote on page 81). To convert these ramp files in more suitable formats select one or multiple files in the data browser at the right of the screen and click with the right mouse button on them. In the menu that appears select 'Export' and choose for example 'ASCII'. This format will give a nice data file that can be easily processed with many data processing software. After clicking a pop-up will appear in which the data columns can be selected.

### B.3 Final remarks

Sometimes it is hard to make good scans of piezoelectric samples. Making good PFM scans relies partly on experience. The best way to make good scans is playing around with the settings. By doing this the user will get a better feeling of the influence of the parameters. Furthermore, for some materials it seems to be easier to get neat PFM scans than for others.

In this user guide the approaching is not discussed. It was assumed that the tip was already in contact and that user knows how to align and approach. This procedure is not different from an AFM measurement. However, with a PFM measurement it may be needed that the 'Deflection Setpoint' in the 'Feedback' sub menu must be increased for successful engaging. This must be done if the bar of the 'Real Time Status' turns red.